To the Graduate Council:

I am submitting herewith a thesis written by Jung-Young Son entitled "Particle Size Analysis Using Scatter Signal Magnitude from an Interference Fringe Pattern." I have examined the final copy of this thesis for form and content and recommend that it be accepted in partial fulfillment of the requirements for the degree of Master of Science, with a major in Electrical Engineering.

W. Michael Farmer

Dr. W. Michael Farmer, Major Professor

We have read this thesis
and recommend its acceptance:

Accepted for the Council:

L. Evans Roth

Vice Chancellor
Graduate Studies and Research

A

PARTICLE SIZE ANALYSIS
USING SCATTER SIGNAL MAGNITUDE
FROM AN INTERFERENCE FRINGE PATTERN

A Thesis

Presented for the

Master of Science

Degree

The University of Tennessee, Knoxville

Jung-Young Son

June 1982

3060946

ACKNOWLEDGMENTS

The author wishes to express his appreciation to Dr. W. Michael Farmer for his assistance and guidance throughout the development of this work. Appreciation is also extended to Dr. R. D. Joseph and Dr. R. A. Belz for their advice during the progress of this work. Thanks are given to the personnel of the Particle Sizing Laboratory at The University of Tennessee Space Institute for their help.

The excellent typing of the manuscript was carried out by Ms. Susan Carpenter.

Sincerest appreciation is given to the author's mother, Mrs. Young-Ja Lee, and to the author's other family for their love and prayer.

ABSTRACT

An analysis is presented of the relationships between particle size and the signal magnitude obtained by light scattered from a dual scatter laser velocimeter interference fringe pattern. The results of the analysis are used to perform a parametric study for some of the factors that affect the performance of a laser interferometer that is designed to measure velocity and particle size. A comparison of the experimental data with performance predictions confirms the essential validity of the analysis.

TABLE OF CONTENTS

SECTION		PAGE
1.	INTRODUCTION	1
2.	THEORETICAL ANALYSIS	7
	2.1 Basic PSI Concepts	7
	2.2 Electronic Measurement of Signal Visibility	19
	2.3 Calculation of PSI Signal Magnitude	20
	2.3.1 Basic Scattering Theory	21
	2.3.2 The Evaluation of the Scattering Intensity Coefficient $C(\theta,\phi)$	23
	2.3.3 Effects of Probe Volume Fringe Contrast Variation	27
	2.3.4 The Evaluation of Minimum Threshold Power	34
	2.3.5 Calculation of the Maximum Number of Available Signal Fringes	38
	2.3.6 Calculation of Mean Signal Amplitude (Mean Pedestal Amplitude)	40
3.	RESULTS OF THE COMPUTATIONS	47
	3.1 Characteristics of the PSI Optical System and Setup	47
	3.2 Computation of the Scattering Gain	49
	3.3 Computation of the Maximum Number of Signal Cycles (N_{max})	57
	3.4 Computation of Interference Fringe Variation	60
	3.5 Computation of Mean Pedestal Amplitude	65
4.	DISCUSSION OF THE RESULTS	77
	4.1 Experimental Setup	77
	4.2 Comparison of Experimental and Computational Results	79

SECTION PAGE

5. SUMMARY AND CONCLUSIONS 88

LIST OF REFERENCES 90

APPENDICES 93

A. NUMERICAL INTEGRATION SCHEME 94

B. RAY TRACE THROUGH THE TRANSPARENT SPHERE 101

VITA 103

LIST OF FIGURES

FIGURE		PAGE
1.	PSI configuration (on-axis collection)	2
2.	Probe volume diagram	3
3.	Gaussian spherical wave.	8
4.	Calculation of fringe period	13
5.	Intensity distribution of probe volume	16
6.	PSI signal characteristics	18
7.	Scattering diagram of PSI.	22
8.	Diffraction by a spherical particle with radius a in the probe volume	28
9.	Focusing of Gaussian beam.	41
10.	Evaluation of starting and ending point of integration	43
11.	PSI Optical System	48
12.	Diffractive scattering gain (using simplified method).	51
13.	Diffractive scattering gain (using numerical method) with no beam stops.	52
14.	Refractive scattering gain in various F-numbers and particulate materials	
	(a) PSL, (b) ethanol	55
	(c) alumina, (b) water	56
15.	Visibility table and the rate of fringe visibility variation	61
16.	The rate of fringe visibility variation with starting point of integration	63
17.	Mean pedestal amplitude of 0.624 μm PSL particle	
	(a) Velocity: 4.5 m/sec.	67
	(b) Velocity: 6.5 m/sec.	68
18.	Mean pedestal amplitude of 1.09 μm PSL particle	
	(a) Velocity: 4.5 m/sec.	69
	(b) Velocity: 6.5 m/sec.	70

FIGURE PAGE

19. Mean pedestal amplitude of 2 μm PSL particle
(a) Velocity: 4.5 m/sec. 71
(b) Velocity: 6.5 m/sec. 72

20. Mean pedestal amplitude distribution of 3 μm PSL particle
(a) Velocity: 4.5 m/sec. 73
(b) Velocity: 6.5 m/sec. 74

21. Experimental setup 78

22. Pedestal amplitude distribution of .624 μm PSL particle
(a) Velocity: 4.5 m/sec. 80
(b) Velocity: 6.5 m/sec. 81

23. Pedestal amplitude distribution of 1.09 μm PSL particle
(a) Velocity: 4.5 m/sec. 82
(b) Velocity: 6.5 m/sec. 83

24. Pedestal amplitude distribution of 3.0 μm PSL particle
(a) Velocity: 4.5 m/sec. 84
(b) Velocity: 6.5 m/sec. 85

A1 64 evaluation points in the numerical integration scheme . . 95

A2 Normalizing of collecting lens' radius to 1 97

A3 Geometry for numerical integration over collecting lens . . 99

A4 Geometry for numerical integration over the beam stops . . . 100

B1 Ray trace through the transparent sphere in the probe volume 102

NOMENCLATURE

a	Particle radius (m)
b	Beam spot size (m)
b_o	Beam waist radius at focal point (m)
$b_{1,2}$	Beam spot sizes of beam 1 and beam 2 (m)
C	Arbitrary constant to match the minimum intensity of the Doppler signal to the signal processor threshold level
$C(\theta,\phi)$	Scattering intensity coefficient
D	Particle diameter (m)
d_1	Distance between beam waist point (in front of transmitting lens) and transmitting lens (m)
d_2	Distance between transmitting lens and focused point (m)
d_3	Distance between probe volume and collecting lens (m)
d_4	Distance between collecting lens and PMT tube (m)
$E_{1,2}$	Field amplitudes of beam 1 and beam 2 (volt/m)
e	Base of natural logarithm
e_c	Electron charge (1.609×10^{-19} coulomb)
F-number	Ratio of d_3 and collecting lens diameter
f_d	Frequency of the measured signal (cycle/sec.)
G	Scattering gain
G_s	Overall signal processor gain
h	Normalized value of YN (h_2YN/δ)
$h\nu_s$	Light energy (joule)
I_o	Intensity of the incident light (watt)
I_p	Probe volume intensity distribution (watt)

$\bar{i}_c$	Mean signal current (ampere)
i_d	Cathode dark current of PMT (ampere)
i_{PMT}	PMT output current (ampere)
$J_{0,1}$	Bessel functions of the first kind of zero and first order
k	Wave number (1/m)
$k_{1,2}$	Propagation direction of beam 1 and beam 2
$\hat{k}_{sc}$	Wave vector of the scattered field
L	Radius of the collecting lens (m)
LFC	Long Fringe Counter
m	Index of refraction
N_L	Setup number of LFC
N_p	Setup number of PC
P	P times beam waist diameter (pb_o)
PC	Precounter
$P_{1,2}$	Powers of laser beam 1 and beam 2 (watts)
PSI	Particle Sizing Interferometer
PSL	Polystyrene latex
PMT	Photomultiplier tube
p	Normalized value of end point of integration
Q	q times beam waist diameter (qb_o)
R	PMT output impedance (ohm)
$R_{1,2}$	Radii of curvature of beam 1, beam 2 (m)
r	Distance between probe volume and a certain point on collecting lens (m)
r_o	Normalized value of r

S_p	Velocity of particle (m/sec.)
T	Half of the distance between beam stops (m)
TEM	Transverse-Electromagnetic
V	Visibility
ΔV	Rate of fringe visibility variation
V_o	Visibility function $(2J_1(\pi D/\delta)/(\pi D/\delta))$
WN	Normalized value of XN ($WN = XN/b_o$)
XN	Position of particle in the probe volume (x-direction)
YN	Position of particle in the probe volume (y-direction)
Z1	Normalized Z-axis value of probe volume
α	Size parameter $(\pi D/\lambda)$
β	Half of the beam incidence angle
δ	Fringe period
η	Quantum efficiency of PMT
ε	Collection efficiency of PSI receiving optics
$\varepsilon_1, \varepsilon_2, \varepsilon_3$	Unit vectors in x, y, z direction
$\hat{\varepsilon}_2', \hat{\varepsilon}_2''$	Unit vectors in y_1 and y_2 direction
θ	Zenith angle (angle which the direction of scattering makes with the direction of propagation of the incident light
$\theta_{1,2}$	Zenith angles in x_1, y_1, Z_1 and x_2, y_2, Z_2 coordinate system
θ_{bs}	The maximum extended angle of beam stops from the probe volume
θ_{max}	The maximum collection angle
λ	Wavelength of the beam (1/m)
$\Delta\nu$	Signal bandwidth
τ	Temporal width of Gaussian beam

τ'	Measured signal time period
ϕ	Azimuth angle in x, y, Z coordinate system
$\phi_{1,2}$	Azimuth angle in x_1, y_1, Z_1 and x_2, y_2, Z_2 coordinate system
Φ_1, Φ_2	Initial phase angle of beam 1 and beam 2
X	Beam incidence angle to a spherical particle
$\psi_{1,2}$	Projection angle of $\phi_{1,2}$ on collecting lens surface
$d\Omega$	Infinitesimal solid angle (steradian)
ω	Angular frequency

1. INTRODUCTION

The dual scatter laser Doppler velocimeter (LDV) has reached the status of a highly-developed engineering tool for the perturbationless measurement of particle velocity in two-phase fluid flow. A commonly used optical configuration (figure 1) for the LDV splits the laser beam into two parallel beams which are made to cross and focus simultaneously using a positive lens. Because the beams are coherent, a Huygens diagram of the wavefronts in the cross-focus region of the beams (see figure 2) will show that a set of planar interference fringes is produced, each fringe of which is parallel to the bisector between the beams and perpendicular to the plane defined by the beams' center lines. Light scattered by aerosol particles passing through this fringe pattern is collected by a lens (usually in the forward direction) and focused to a photodetector which produces a measurable current. The operation of the instrument is most easily visualized using the so-called fringe model. The fringe model assumes the scattered light signal will be a replica of the intensity distribution illuminating the particle. This is found to be a reasonable assumption as long as the particle size is small compared to the fringe period. The fringe period is a constant for a given optical geometry. It is a function only of the laser wavelength and angle between the beams. Hence, measurement of the scattered light signal frequency can be used to produce an estimate of particle velocity.

Ten years ago, Farmer[1] first showed that by measuring the ratio of the sinusoidal amplitude of the scattered light signal to the mean

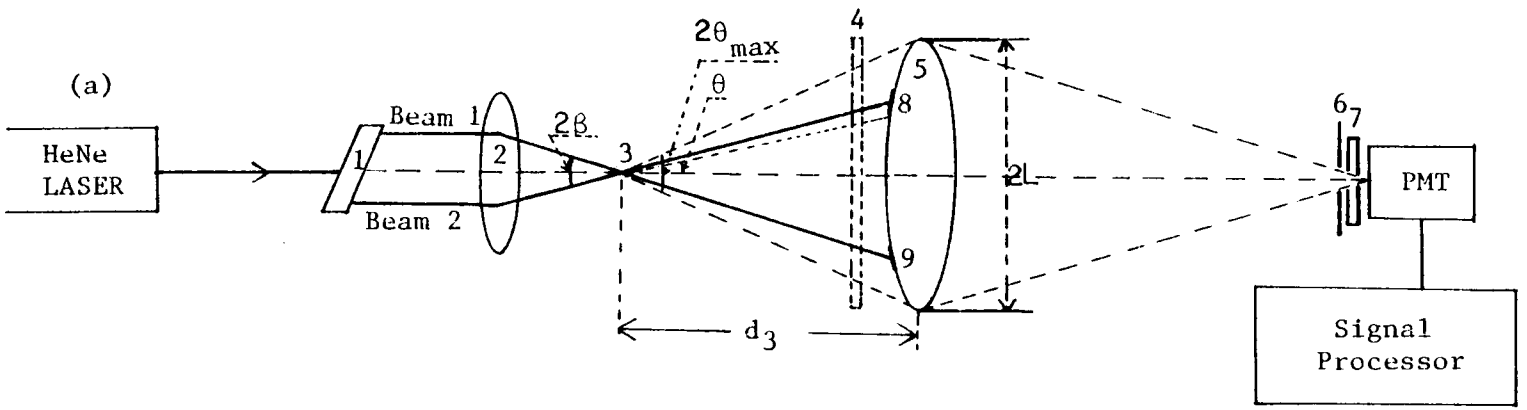

Figure 1. PSI configuration (on-axis collection).

1: Beam Splitter
2: Transmitting Lens
3: Probe Volume
4: Window
5: Collecting Lens
6: PMT Aperture
7: Light Filter
8: Beam Stop
9: Beam Stop
L: Radius of Collecting Lens
θ: Collecting Angle

F-number: $d_3/2L$

θ_{max}: Maximum Collecting Angle

d_3: Distance From Probe Volume to Collecting Lens

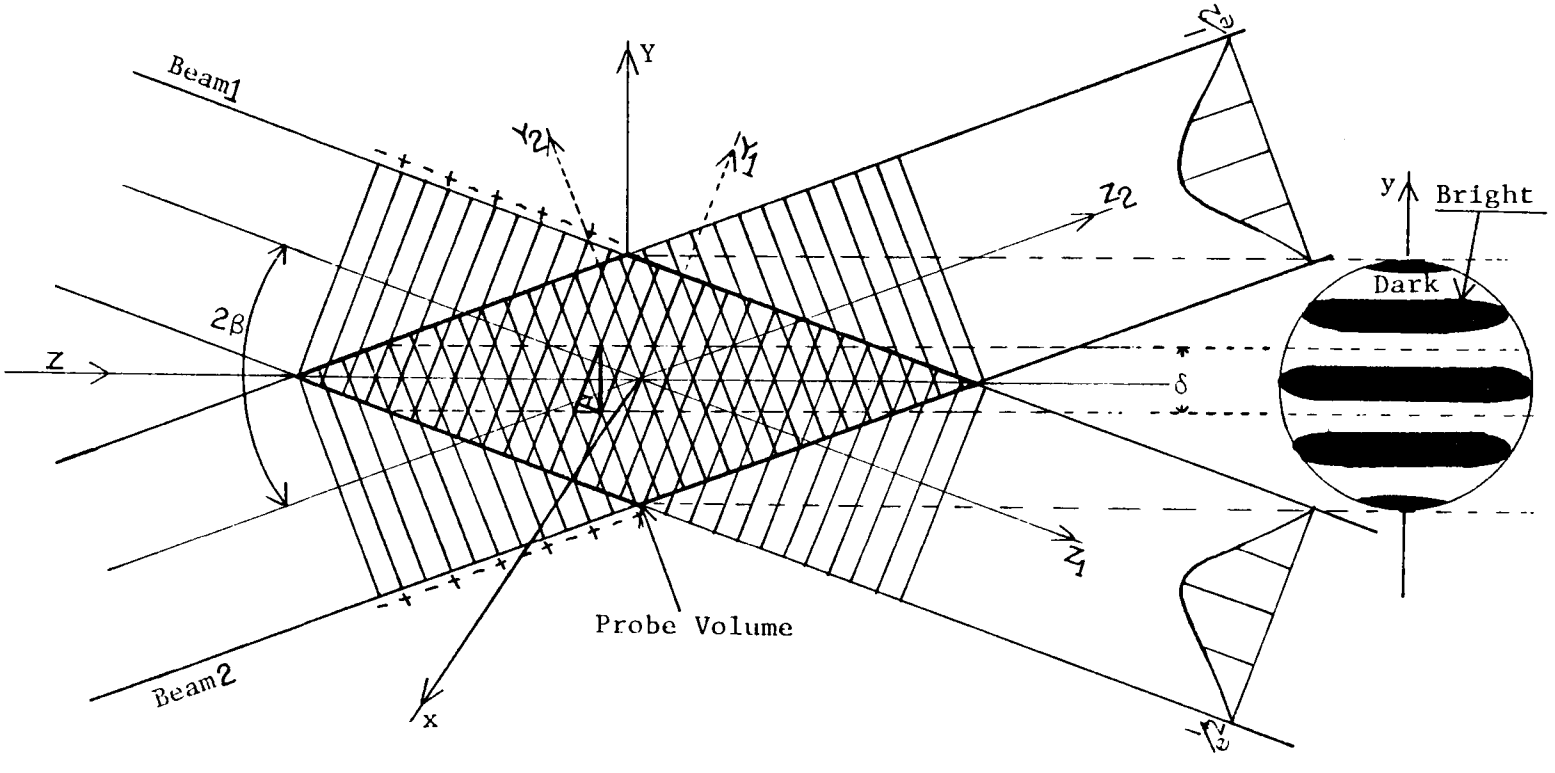

Figure 2. Probe volume diagram.

value of the signal amplitude (this ratio is called the visibility), particle size could be determined. Particle size measurement using the visibility was thus found to be independent of signal magnitude. This method of measurement was unlike commercially available optical particle counters in that it did not have to sample the aerosol with a mechanical probe (i.e., it had the perturbationless measurement characteristic of the LDV), and it avoided calibration difficulties associated with particle sizers depending on pulse height analysis. When the LDV optical system is used primarily for particle size analysis, it has traditionally been called a particle sizing interferometer (PSI).

Even though a visibility measurement allows particle size to be determined independent of signal magnitudes, this parameter, as the following discussion indicates, continues to play a significant role in PSI system operation and in extending the capability of an interferometer designed to measure both particle size and velocity. In a 1976 paper, Farmer[2] showed that the fringe volume (often called the probe or sample volume) in which a particle size measurement could be obtained depended on the size of the particle being measured. Hence, when a particle size distribution is measured, the number of measurements as a function of size must be weighted in order to obtain a volume-normalized probability of occurrence distribution. The size dependence of the fringe volume arises from the following facts. The signal processor used to measure visibility is a threshold limited device (i.e., the signal must reach a certain amplitude before it is

measured). Furthermore, the spatial distribution of the mean intensity in the probe volume follows a Gaussian distribution function. Thus, a very large particle scattering a low level of incident intensity near the edge of the probe volume can generate a signal magnitude equal to that of a small particle scattering a high level intensity near the center of the probe volume.

A relative signal magnitude as a function of particle size is, therefore, an important parameter in developing the proper weighting function with which to normalize size distributions measured with a PSI.

A visibility measurement for a specific optical arrangement can commonly cover a 10:1 or, at best, 20:1 variation in particle size range.[3] For particle sizes smaller or larger than this range, the visibility function relating particle size to visibility is not monotonic (for sizes larger than a fringe period) or size resolution limited (for sizes smaller than 1/20 of a fringe period). However, signal magnitude measurement can eliminate or reduce many of the ambiguities found in a visibility measurement outside the size range detected by a specific optical measurement. Since the present University of Tennessee Space Institute (UTSI) visibility signal processor can also measure the mean signal magnitude, correlation of particle size with scattered signal magnitude obtained with these devices provides both an independent check of the particle sizes measured using the visibility approach and a means of possibly extending the measurable size range by eliminating ambiguous sizes

resulting from visibility measurements made outside the size range determined by a particular optical arrangement.

A second area of interest in PSI signal magnitudes arises from questions regarding the minimum detectable particle size observable with a given PSI or LDV. Such questions can only be answered by consideration of the scattered signal magnitude relative to the signal processor threshold.

Although users of PSI systems have been aware of many of the effects of signal magnitude on system operation and, in some cases, have attempted to compensate for such effects by crude models, relatively few detailed analyses have been made.[4]

The purpose of this research is to develop an analysis of PSI signal magnitude effects which can be used to provide approximate answers and solutions to many of the questions raised in the preceding discussion.

2. THEORETICAL ANALYSIS

This section presents a theoretical analysis of the mean signal amplitude response characteristics of the particle sizing interferometer. Specifically treated is the interferometer response as a function of (1) particle diameter, (2) particle velocity, and (3) signal processor constraints.

The analysis begins by reviewing basic PSI concepts. A scattering theory approximation based on diffraction, refraction, and reflection is then applied to spherical transparent particles scattering in a PSI probe volume. The resulting equations developed from the analysis are then parameterized with dimensionless variables to facilitate evaluation of the PSI performance for a variety of input variables.

2.1 Basic PSI Concepts

In this subsection, the basic concepts and instrumentation features of particle sizing interferometry are reviewed. These results are used as a formal basis for developing the analysis and equations necessary to predict PSI signal magnitudes.

Consider first the properties of the laser beam typically used in the instrument. In most lasers used in a PSI, the beam is composed of spherical waves having a Gaussian variation[5] (TEM_{ooq} mode) in amplitude across the wavefront as depicted in figure 3. The Gaussian amplitude distribution normalized for unit power may be expressed in Cartesian coordinates as[6]

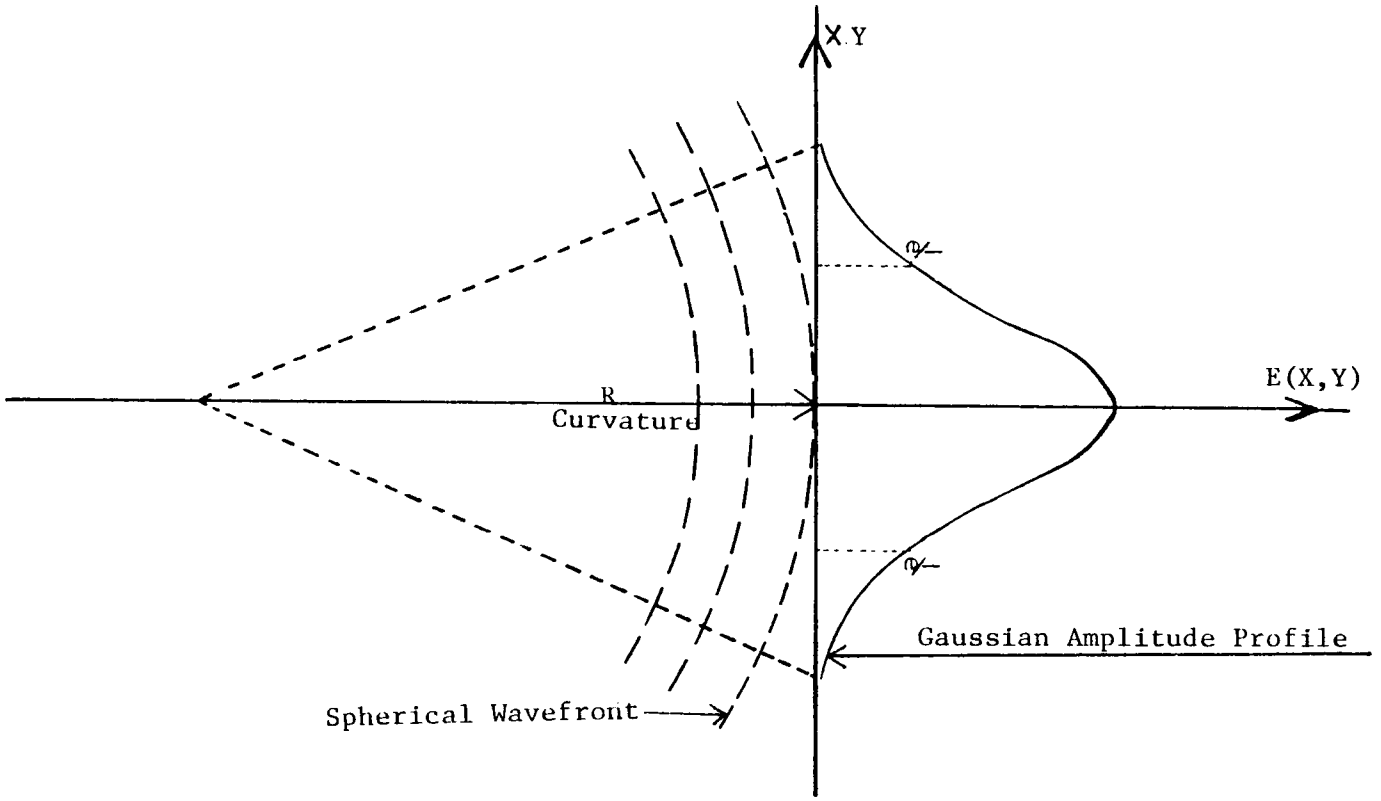

Figure 3. Gaussian spherical wave.

$$|E(x,y)| = \frac{1}{\pi}\,\frac{1}{b}\,e^{-(x^2 + y^2)/b^2} \tag{1}$$

where b (often called the spot size) is defined as the distance from the beam axis for which the beam irradiance (the power per unit area) decreases to $1/e^2$ of its value.

Consider two parallel and equal intensity coherent beams which are linearly polarized in the same direction and are incident on an ideal positive lens (no aberration and 100% transmission). The beams passing through the lens may be expressed in terms of electromagnetic fields with Gaussian amplitudes (see figure 2).

$$E_1 = \frac{P_1}{\pi b_1^{\,2}} \exp\left[-\frac{1}{b_1^{\,2}}\left(x_1^{\,2} + y_1^{\,2}\right)\right]$$

$$\cdot \exp\left[i\omega t - i\,\frac{2\pi}{\lambda} Z_1 + i\Phi_1\right]$$

$$\cdot \exp\left[-j\,\frac{\pi}{\lambda}\,\frac{x_1^{\,2} + y_1^{\,2}}{R_1}\right] \tag{2a}$$

$$E_2 = \frac{P_2}{\pi b_2^{\,2}} \exp\left[-\frac{1}{b_2^{\,2}}\left(x_2^{\,2} + y_2^{\,2}\right)\right]$$

$$\cdot \exp\left[i\omega t - i\,\frac{2\pi}{\lambda} Z_2 + i\Phi_2\right]$$

$$\cdot \exp\left[-j\,\frac{\pi}{\lambda}\,\frac{x_2^{\,2} + y_2^{\,2}}{R_2}\right] \tag{2b}$$

where

λ,ω = wavelength and angular frequency, respectively

R_1,R_2 = radii of curvature of each Gaussian beam

P_1,P_2 = powers of laser beams 1 and 2 (watt)

Z_i = (i = 1,2) beam propagation direction

x_i,y_i = (i = 1,2) axis components normal to Z_i

Φ_i = (i = 1,2) initial phase angle of beam 1 and beam 2, respectively.

In the PSI, these fields are generated after the incident laser beam is divided into two parallel beams with almost equal power by a beam splitter (see figure 1). After passing through the transmitting lens, the two beams focus and cross in the focal plane of the lens. This region is identified as the probe volume.

If it is assumed that the lens is ideal and the path difference of the two beams produced by the beam splitter only introduces an integer multiple of 2π in the relative phases; then at the geometric center of the probe volume the two laser beams having the same minimum spot size, b_o, called the beam waist, become plane waves because R_i goes to infinity as Z_1,Z_2 approach zero. Hence, Equation 2 can be expressed as

$$E_1 = \frac{P_1}{\pi b_o^2} \exp\left[-\frac{1}{b_o^2}(x_1^2 + y_1^2)\right] \cdot \exp\left[i\omega t - i\frac{2\pi}{\lambda} Z_1 + i\Phi\right] \qquad (3a)$$

$$E_2 = \frac{P_2}{\pi b_o^2} \exp\left[-\frac{1}{b_o^2}(x_2^2 + y_2^2)\right]$$

$$\cdot \exp\left[i\omega t - i\frac{2\pi}{\lambda} Z_2 + i(\Phi + 2\pi)\right]. \qquad (3b)$$

To express E_1 and E_2 in the same coordinate system, consider a rectangular coordinate system having as an origin the center of the probe volume defined in figure 2. Here the Z-axis is the bisector of two beams, the x-axis is parallel to the polarization direction, and the y-axis is normal to both these axes in a right-handed sense. If the beam incidence angle (angle between Z-axis and beam 1 and beam 2) is β, Equation 3 is expressed through the rotation of the coordinate of each beam as

$$E_1 = \frac{P_1}{\pi b_o^2} \exp\left[-\frac{1}{b_o^2}[x^2 + (Y\cos\beta - Z\sin\beta)^2]\right]$$

$$\cdot \exp\left[i\omega t - i\frac{2\pi}{\lambda}(Z\cos\beta + y\sin\beta) + i\Phi_1\right] \qquad (4a)$$

$$E_2 = \frac{P_2}{\pi b_o^2} \exp\left[-\frac{1}{b_o^2}[x^2 + (y\cos\beta + Z\sin\beta)^2]\right]$$

$$\cdot \exp\left[i\omega t - i\frac{2\pi}{\lambda}(Z\cos\beta - y\sin\beta) + i(\Phi_1 + 2\pi)\right] \qquad (4b)$$

where it is assumed that the beams are linearly polarized in the x direction.

The intensity of a combined field is given by[7]

$$I_p = \mathrm{Re}(E_1 + E_2)(E_1^* + E_2^*) = |E_1|^2 + |E_2|^2 + 2\mathrm{Re}(E_1 E_2^*) \tag{5}$$

where Re represents the real part. Thus, the probe volume intensity distribution is given by

$$I_p = \frac{1}{\pi b_o^2} \exp\left[-\frac{2}{b_o^2}(x^2 + y^2\cos^2\beta + z^2\sin^2\beta)\right]$$

$$\cdot \left[P_1 \exp\left(-\frac{2yz\sin 2\beta}{b_o^2}\right)\right.$$

$$\left. + P_2 \exp\left(\frac{2yz\sin 2\beta}{b_o^2}\right) + 2\sqrt{P_1 P_2}\cos\left(\frac{4\pi y \sin\beta}{\lambda}\right)\right]. \tag{6}$$

Two coherent waves will generate a series of dark and bright interference fringes. The fringe period is given by δ (see figure 4),

$$\delta = \frac{\lambda/2}{\sin\beta} \tag{7}$$

where λ is the wavelength of the laser beam used to produce the coherent wave.

If β is small, ($\beta \lesssim \pi/9$) and $P_1 = P_2$, $\sin\beta \simeq \beta$, and $\cos\beta \simeq 1$. Hence, equation 6 becomes

$$I_p = \frac{2P_1}{\pi b_o^2} \exp\left[-\frac{2}{b_o^2}(x^2 + y^2 + z^2\beta^2)\right] \cdot \left[\cosh\left(\frac{4yz}{b_o^2}\right) + \cos\left(\frac{2\pi y}{\delta}\right)\right] \tag{8}$$

as given by Farmer.[8]

As particles pass through the probe volume, they disturb the incident fields. Therefore, a certain amount of light proportional

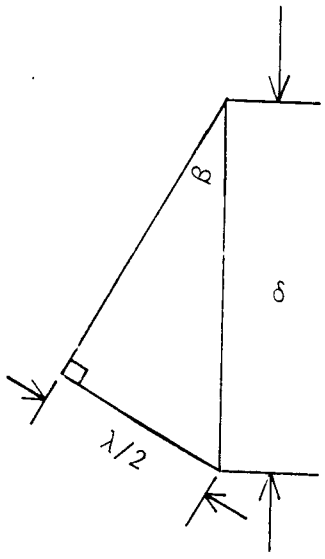

Figure 4. Calculation of fringe period.

to the particle cross-sectional area is scattered in all directions. Scattered light passing through the collecting lens is focused on the photomultiplier tube (PMT). The PMT converts the incident scattered light power into an electrical signal which is amplified and processed. When the scattered light collecting lens is centered on the bisector between the beams (often referred to as on-axis collection), the original laser beams are shielded from the photodetector by beam stops in order to prevent photodetector saturation (the scattered light containing particle size information is much weaker in amplitude than the unscattered light). It is noteworthy that beam stops may also remove a significant portion of the scattered intensity. The effect of the beam stop on the measured signal is discussed more fully in section 2.2.2.

To remove background light from the sun and artificial lamps, an aperture and light filter are placed in front of the PMT. A window is also used to prevent contamination of the lenses by the sampled particles. All these materials also remove some of the collected scattered laser power which directly affects measured signal magnitude and ultimately signal-to-noise ratio.

Since the cosh term in Equation 8 represents DC (in the sense that an equivalent current wave form would be "constant" compared to the high frequency (AC) portion of the equivalent current wave form resulting from the interference fringes) intensity variation of probe volume caused by the Gaussian nature of the laser beam intensity profile, Equation 8 can be expressed as the ratio of

DC to AC intensity of the probe volume. The cosh term in equation 8 can be manipulated outside the bracket to form

$$I_p = AA \cdot \left[1 + \frac{1}{\cosh(4yZ\beta/b_o^2)} \cos\left(\frac{2\pi y}{\delta}\right)\right] \tag{9}$$

where AA is given by

$$AA = \frac{2P_1}{\pi b_o^2} \exp\left[-\frac{2}{b_o^2}(x^2 + y^2 + Z^2\beta^2)\right] \cosh(4yZ\beta/b_o^2). \tag{10}$$

Equation 9 shows that the total intensity is a sum of the intensity profile given by AA and cosine modulated AA with a modulation index $1/\cosh(4yZ\beta/b_o^2)$. The modulation index shows that when y or Z or both values are increased, the sinusoidal amplitude decreases (i.e., DC intensity becomes dominant over the probe volume). Here, $1/\cosh(4yZ\beta/b_o^2)$ is called the fringe visibility variation when $P_1 = P_2$ (see next section for $P_1 \neq P_2$). When Z or y equals zero, the cosh term is 1. This represents 100% modulation. I_p is represented graphically in figure 5a for several values of Z. In figure 5a, the DC part and AC part of Equation 9 are drawn separately for the purpose of illustration. Figures 5b and 5c are graphic representations of AA and modulated AA, respectively, at different values of the Z-axis. These figures also represent filtered outputs (figure 5b - low pass filtered, figure 5c - band pass filtered) of the PSI signal processor.

The following discussion explains how the signal shape depends on particle size and its position within the probe volume (see

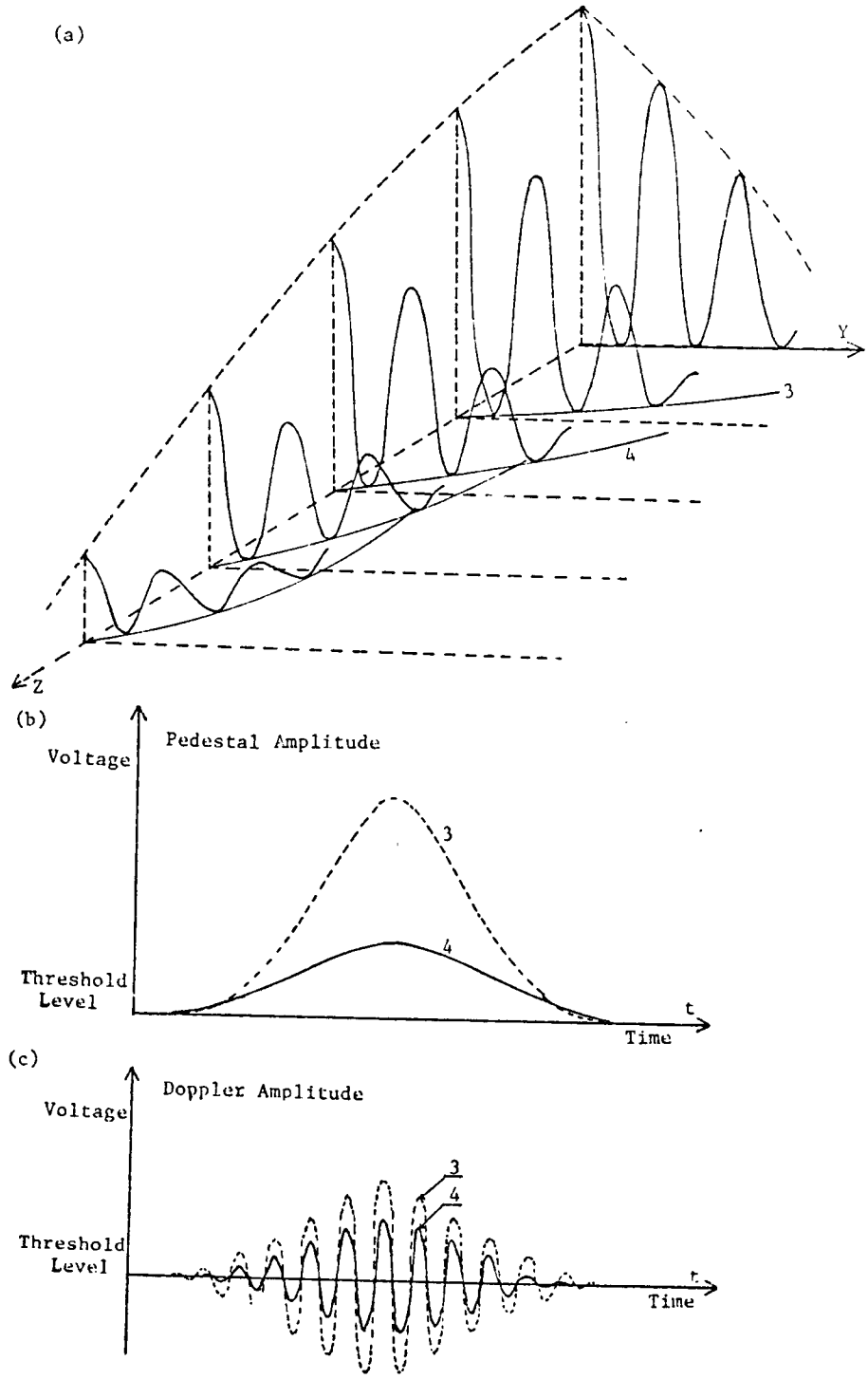

Figure 5. Intensity distribution of probe volume.
(a) Intensity distribution of probe volume.
(b) Filtered pedestal signal.
(c) Filtered Doppler signal.

figures 6a-e). It is assumed that Z in Equation 9 is zero. When a particle is small enough compared to the fringe period, it can accurately reproduce the intensity distribution along its trajectory (see figure 6b). However, when a particle diameter becomes large relative to δ, it will instantaneously cover a large portion of an interference fringe. Therefore, the intensity distribution of its trajectory is averaged over the particle cross-section. The resulting signal is shown in figure 6d.

It can be seen that the ratio of the alternating part of the resulting signal called the "Doppler signal" to a slowly varying part called the "pedestal signal" is related to particle size and trajectory. The ratio of the two is called visibility. In other words, the visibility is the ratio of the difference to the sum of the maximum and minimum intensities in the resulting signal[9] i.e.,

$$\text{VISIBILITY} = \frac{I_{max} - I_{min}}{I_{max} + I_{min}} . \qquad (11)$$

For a given optical geometry, the total number of available fringes (i.e., detectable signal cycles) is dependent on the threshold level of the signal processor, probe volume diameter, particle size, and particle trajectory. Figure 6d depicts a number of possible trajectories and their dependence on the number of available fringes. The mathematical treatment of the number of measurable interference fringes will be given later.

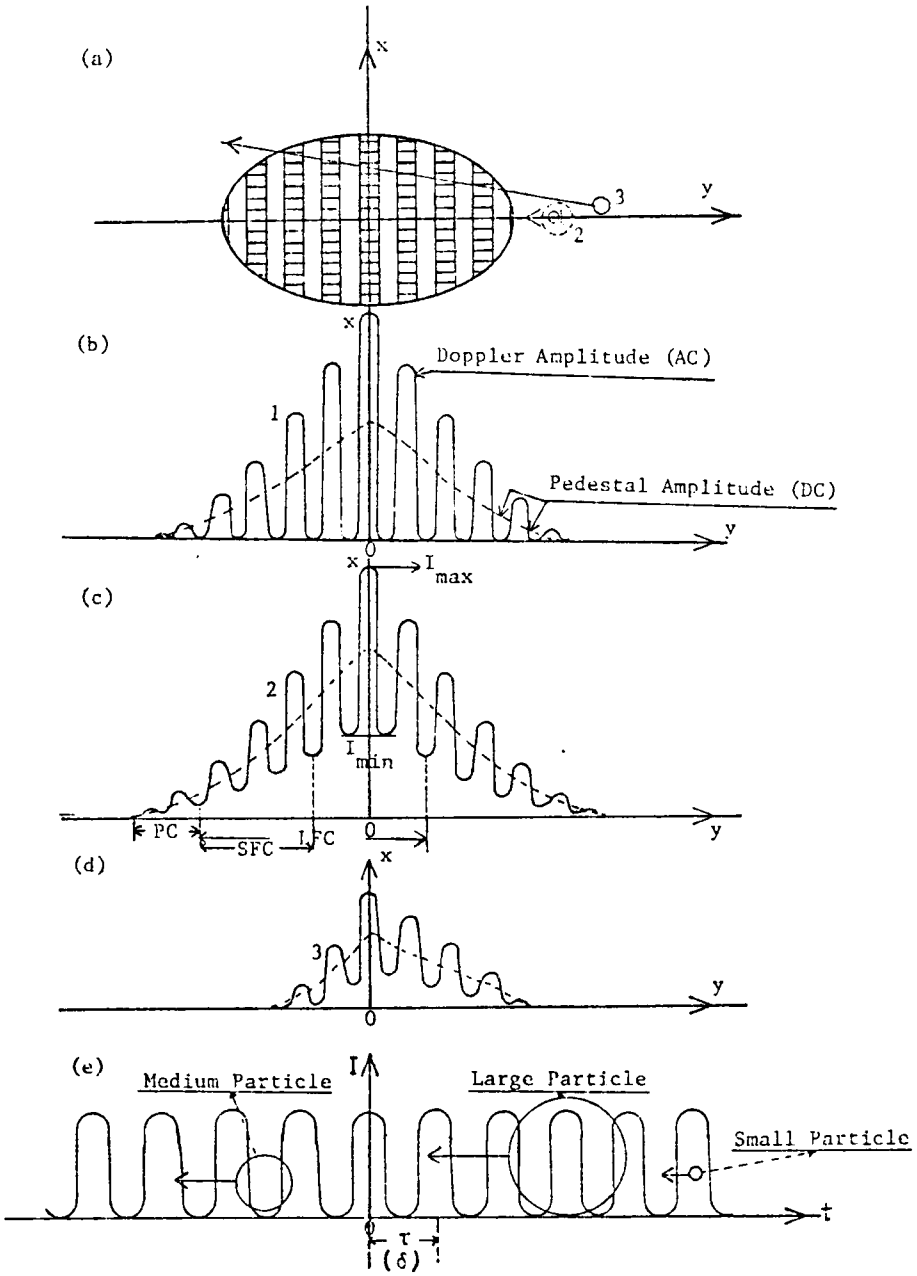

Figure 6. PSI signal characteristics.
(a) Probe volume profile. Circles represent particles.
(b) Signals for small particles.
(c) Signals for larger particles.
(d) Signals resulting from the particles passing through the edge of probe volume.
(e) Probe volume fringe pattern (assume same intensity distribution). If particle becomes large, it overlaps several fringes at one time.

2.2 Electronic Measurement of Signal Visibility

In actual particle sizing experiments, a number of uncontrollable factors can affect system performance. For example, particles are often not uniform in shape, particle trajectories and arrival rates at the probe volume are random, and often several particles can pass through the probe volume at the same time. Therefore, the resulting signal often contains both information and noise and is subject to a broad range of potential variations. To measure visibility, the signal processor separates and filters and signal into high and low frequency parts. After the high frequency portion is rectified, the signal processor then integrates both parts over the number of fringes specified in the instrument. The integration yields the mean amplitude of each part of the original signal. The number of fringes for signal integration by the signal processor is specified by the instrument operator.

There are three kinds of signal cycles of fringe setups made by the operator: Long Fringe Counter (LFC), Precounter (PC), and Short Fringe Counter (SFC) (see figure 6d).[10] Because the incident light level is low, the very beginning of the signal is noisy and signal quality is not good. To remove this noise, the initiation of integration is moved by the precounter to a higher amplitude position of the signal than required for threshold. With this setup, several initial fringes specified by PC are removed from the measurement. Actual integration is performed over the number

of fringes given by the long fringe counter setup. A short fringe counter is used to test signal aperiodicity caused by, for example, multiple particles. (For details, see reference 10.)

The signal processor is also used to measure signal time period in order to determine particle velocity. If τ' is the measured signal time period, then particle velocity is given by (see figure 6e)

$$S_p = \delta/\tau'. \tag{12}$$

The frequency of the measured signal, f_d, is given by $f_d = 1/\tau'$.

2.3 Calculation of PSI Signal Magnitude

To calculate expected signal amplitudes from the signal processor, a number of significant factors should be considered:

1. Fringe period;
2. Scattering intensity function for the collecting lens with beam stops;
3. Probe volume "diameter";
4. Collecting lens F-number and collection efficiency;
5. Minimum intensity for a given size of particle corresponding to the signal processor threshold level;
6. PMT gain;
7. Signal processor gain.

From this list, terms 1, 3, 4, 6, and 7 are PSI parameters known á priori with only 2 and 3 requiring calculation. The optical distribution and magnitude of the scattered intensity will be

considered first. These results will then be used for a parametric evaluation of PSI system performance.

2.3.1 Basic Scattering Theory

If I_o is the intensity of the incident light and I is the intensity of scattered light at a point a large distance r($r >> D^2/\lambda$) from the particle, then as van de Hulst[11] has shown, I is a function of I_o, r, azimuth angle, ϕ, and zenith angle, θ, (which the direction of scattering makes with the direction of propagation of the incident light). Following van de Hulst, I can be written as

$$I = \frac{I_o F(\theta,\phi)}{k^2 r^2} \tag{13}$$

where k is the wave number defined by $2\pi/\lambda$ and $F(\theta,\phi)$ is the scattering intensity function per unit solid angle. Therefore, the total light power scattered by a small particle can be obtained by integrating over all the space ($0 < \theta < \pi$ and $o < \phi < 2\pi$)

$$I_{total} = \int_o^{\pi} \int_o^{2\pi} \frac{I_o F(\theta,\phi)}{k^2 r^2} \cdot dA = \int_o^{\pi} \int_o^{2\pi} \frac{I_o F(\theta,\phi)}{k^2} d\Omega \tag{14}$$

where $dA = r^2 \sin\theta d\theta d\phi$ and $d\Omega = \sin\theta d\theta d\phi$. An example of a PSI scattering diagram is given in figure 7. Since the beams are not normally incident on the collecting lens surface, specific geometry and numerical methods are needed to evaluate the scattered intensity collected by the lens (see Appendix A). However, when the beam incident angle β is small, it can be assumed that the beams are almost normal at the lens surface. In this case, the integrated scatter

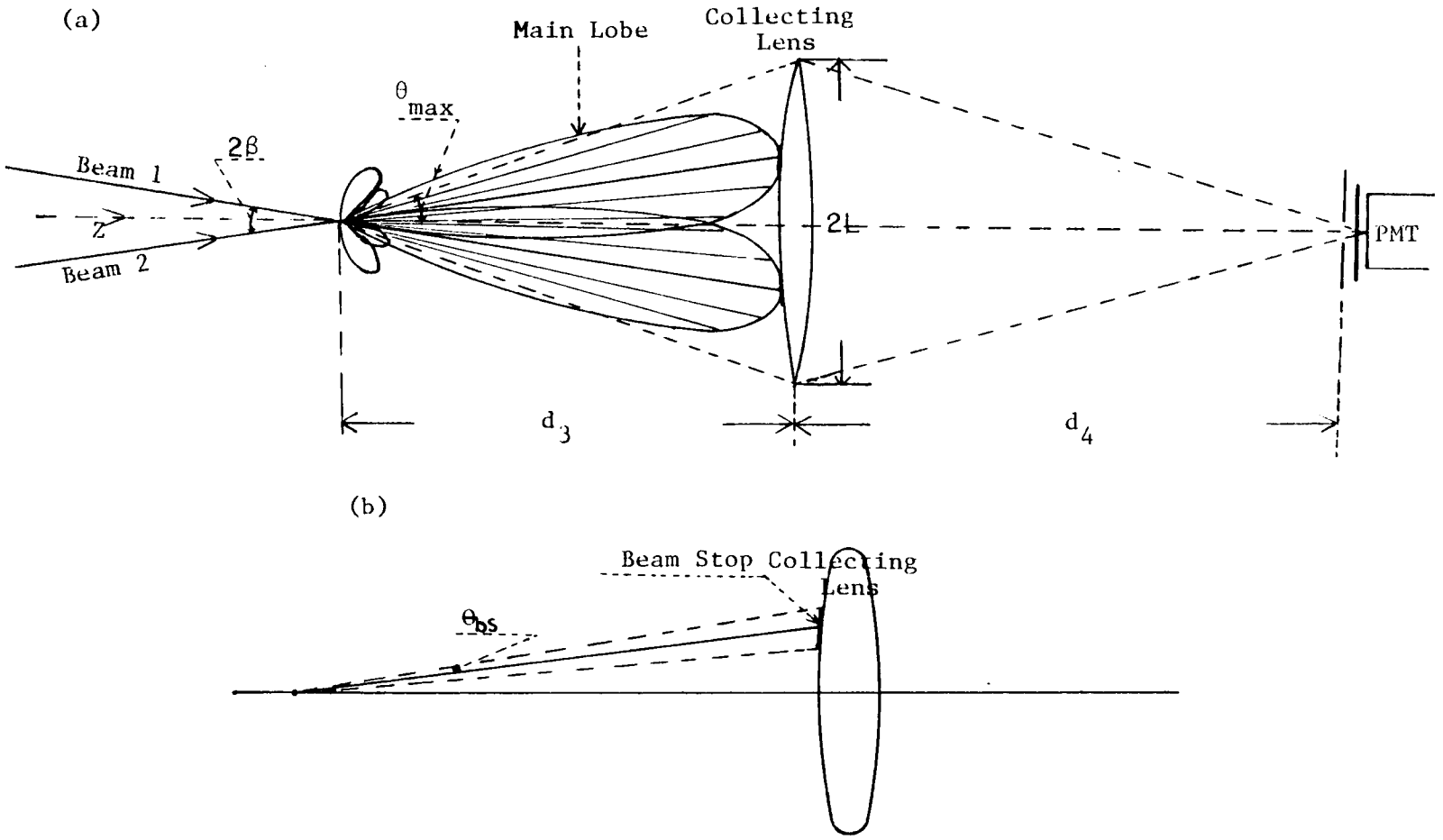

Figure 7. Scattering diagram of PSI.
(a) Scattering diagram for collecting lens.
(b) Scattering diagram over the beam stop.

intensity over the collecting lens surface is given by

$$I_{collect} = I_o \int_0^{\theta_{max}} \int_0^{2\pi} \frac{F(\theta,\phi)}{k^2} \, d\Omega \qquad (15)$$

where θ_{max} is the maximum collecting angle depending on the F-number of the collecting lens which is defined as the ratio of the collecting lens diameter to the distance between the probe volume and the collecting lens. $F(\theta,\phi)/k^2$ is defined as the scattering intensity coefficient, $C(\theta,\phi)$, defined by Hodkinson and Greenleaves.[12] When both laser beams have the same intensity, I_o can be written as AA in Equation 9. It should be remembered that Equation 15 gives only mean (pedestal) intensity. To evaluate the Doppler signal intensity, another step is needed. Section 2.3.3 will treat this problem (see also reference 13).

2.3.2 The Evaluation of the Scattering Intensity Coefficient $C(\theta,\phi)$

The ratio of the particle circumference to the wavelength, λ, of illuminating light is called the size parameter α ($\alpha = \pi D/\lambda$), where D is the particle diameter. Several different scattering theory approximations can be applied to evaluate the scattering intensity function. For spheres, the Lorenz-Mie scattering theory gives an exact solution for $F(\theta,\phi)$. However, evaluation is very difficult because many terms in a series expansion are required when $\alpha >> 1$.

It was shown by van de Hulst[11] that the simplified theories of optics represented by diffraction, refraction, and reflection are good approximations of Lorenz-Mie theory when α is larger than

10 ($D \gtrsim 2$ μm, for $\lambda = 0.60$ μm). However, a recent paper by Ungut, et.al.,[14] showed that, at $\lambda = .5145$ μm, for spherical transparent particles ($1\ \mu m \lesssim D \lesssim 100\ \mu m$) and for forward scattering angles ($0 \sim 20°$), the scattering pattern of the Lorenz-Mie theory agrees well with that of diffraction theory and geometric optics represented by reflection and refraction even beyond the range for which these approximations are expected to apply.

The light diffracted by the particle is found to be concentrated in a main lobe centered about the illuminating beam propagation direction (see figure 7). The width of this main lobe becomes smaller with increasing particle diameter (angular extent $\sim \lambda/d$). Therefore, when the particle becomes large, the beam stop will remove a significant portion of the diffracted light. Diffractive scattering often refers to the Fraunhofer diffraction pattern produced by the scattering particle. About 85% of the diffracted intensity is contained in the main lobe.

Scattered light which is not the result of diffraction is distributed in all directions by reflection and refraction. Hodkinson and Greenleaves[12] showed that, when the index of refraction, m, is 1.5 and $\alpha \gtrsim 15$ ($D \simeq 3$ μm) and the scattering angle, θ, is larger than $\pi/18$ radians, refractive scattering is greater in amplitude than diffractive scattering. Hence, if the collecting lens' F-number becomes small, refractive scattering in the on-axis collection system should be considered in addition to that resulting from diffraction. The expression for the refractive scattering

intensity coefficient for transparent spheres is given by Hodkinson, et.al.,[12] by considering internal reflection,

$$C_{Rr}(\theta,\phi) = \frac{2}{\pi}\left[\frac{m}{(m^2-1)}\right]^4\left[\frac{(m\cos(\theta/2)-1)^3(m-\cos(\theta/2))^3(1+\sec^4(\theta/2))}{\cos(\theta/2)(m^2+1-2m\cos(\theta/2))^2}\right] \quad (16a)$$

and by Bachelo, et.al.[13], by considering no internal reflection

$$C_{Rr}(\theta,\phi) = \frac{1}{\pi}\left[1 - \frac{\sin x - [m^2-\cos^2 x]^{1/2}}{\sin x + [m^2-\cos^2 x]^{1/2}}\right]^2\left[\frac{\sin 2x}{4\sin\theta(1 - \frac{\tan x}{\tan x'})}\right] \quad (16b)$$

where

$$x = \tan^{-1}\left[\frac{m\cos(\theta/2) - 1}{m\sin(\theta/2)}\right] \quad (17a)$$

$$x' = \cos^{-1}\left(\frac{1}{m}\cos x\right) . \quad (17b)$$

Derivation of Equation 17 is given in Appendix B.

The expression for the reflective scattering intensity coefficient for transparent spheres is from Equation 16b and the Fresnel reflection coefficients

$$C_{Rf}(\theta,\phi) = \frac{1}{\pi}\left[\frac{\sin x - (m^2-\cos^2 x)^{1/2}}{\sin x + (m^2-\cos^2 x)^{1/2}}\right]^2\left[\frac{\sin 2x}{4\sin\theta(1 - \frac{\tan x}{\tan x'})}\right] \quad (18)$$

where x and x' are given in Equation 17. The derivation for the diffractive scattering intensity coefficient for transparent spheres[12] is given by a case in which scalar diffraction theory can be applied:

$$C_{di}(\theta,\phi) = \frac{\alpha^2}{4\pi}\left[2\frac{J_1(\alpha\sin\theta)}{\alpha\sin\theta}\right]^2 . \quad (19)$$

If Equation 15 is used, then the intensity collected by the collecting lens due to diffraction is

$$I_{di\text{-}collected} = 2\pi I_o \int_o^{\theta_{max}} C_{di}(\theta)\sin\theta d\theta$$

$$= I_o \left[1 - J_0^2(\alpha\sin\theta_{max}) - J_1^2(\alpha\sin\theta_{max}) \right]. \qquad (20a)$$

The diffractive scattering intensity removed by the beam stops, $I_{di\text{-}bs}$, can be calculated by substituting θ_{max} in Equation 20a with θ_{bs} maximum extended angle of beam stops from the probe volume (see figure 7b). Hence,

$$I_{di\cdot bs} = I_o \left[1 - J_0^2(\alpha\sin\theta_{bs}) - J_1^2(\alpha\sin\theta_{bs}) \right]. \qquad (20b)$$

By combining Equations 20a and 20b, the actual collected scattering intensity $I_{di\text{-}actu}$ can be written as

$$I_{di\text{-}actu} = I_{di\text{-}collected} - I_{di\text{-}bs}$$

$$= I_o \left[J_0^2(\alpha\sin\theta_{bs}) + J_1^2(\alpha\sin\theta_{bs}) \right.$$

$$\left. - J_0^2(\alpha\sin\theta_{max}) - J_1^2(\alpha\sin\theta_{max}) \right] \qquad (20c)$$

where J_0 and J_1 are Bessel functions of the first kind of zero and first order, respectively. Equations 20a and 20b are given by Born and Wolf.[15] Equation 20c is given by Farmer.[16]

For the case of vector diffraction for the calculation of

polarization effects in the scattered light, Jackson[17] gives

$$C_{di}(\theta,\phi) = \cos\beta \frac{\alpha^2}{4\pi} (\cos^2\theta + \cos^2\phi\sin^2\theta)\left[\frac{J_1(\alpha\gamma)}{\alpha\gamma}\right]^2 \qquad (21)$$

where ϕ is the azimuthal angle of the scattered light and γ is given by (see figure 8)

$$\gamma = (\sin^2\theta + \sin^2\beta - 2\sin\theta\sin\beta\cos\phi)^{\frac{1}{2}} . \qquad (22)$$

For spherical particles, light beams are normally incident on the cross-sectional area of the particle, so $\beta = 0$, $\sin\beta = 0$, $\cos\beta = 1$, and $\gamma = \sin\theta$. Therefore,

$$C_{di}(\theta,\phi) = \frac{\alpha^2}{4\pi} (\cos^2\theta + \cos^2\phi\sin^2\theta)\left[\frac{J_1(\alpha\sin\theta)}{\alpha\sin\theta}\right]^2 . \qquad (23)$$

For convenience, define $I_{collected}/I_o$ as the scattering gain. In the simplified optics theory approach taken for this work, the scattering gain can be represented by the sum of the above three terms:

$$\frac{I_{collected}}{I_o} = \int_o^{\theta_{max}} \int_o^{2\pi} \left[C_{Rr}(\theta,\phi) + C_{Rf}(\theta,\phi) + C_{di}(\theta,\phi)\right] d\Omega . \qquad (24)$$

The scattering gain will be used in sections 2.3.4 through 2.3.6 to compute signal amplitude.

2.3.3 Effects of Probe Volume Fringe Contrast Variation

Because the beams forming the probe volume have Gaussian amplitude variations along the respective beam axes, the interference fringe visibility will be a function of spatial position in the probe

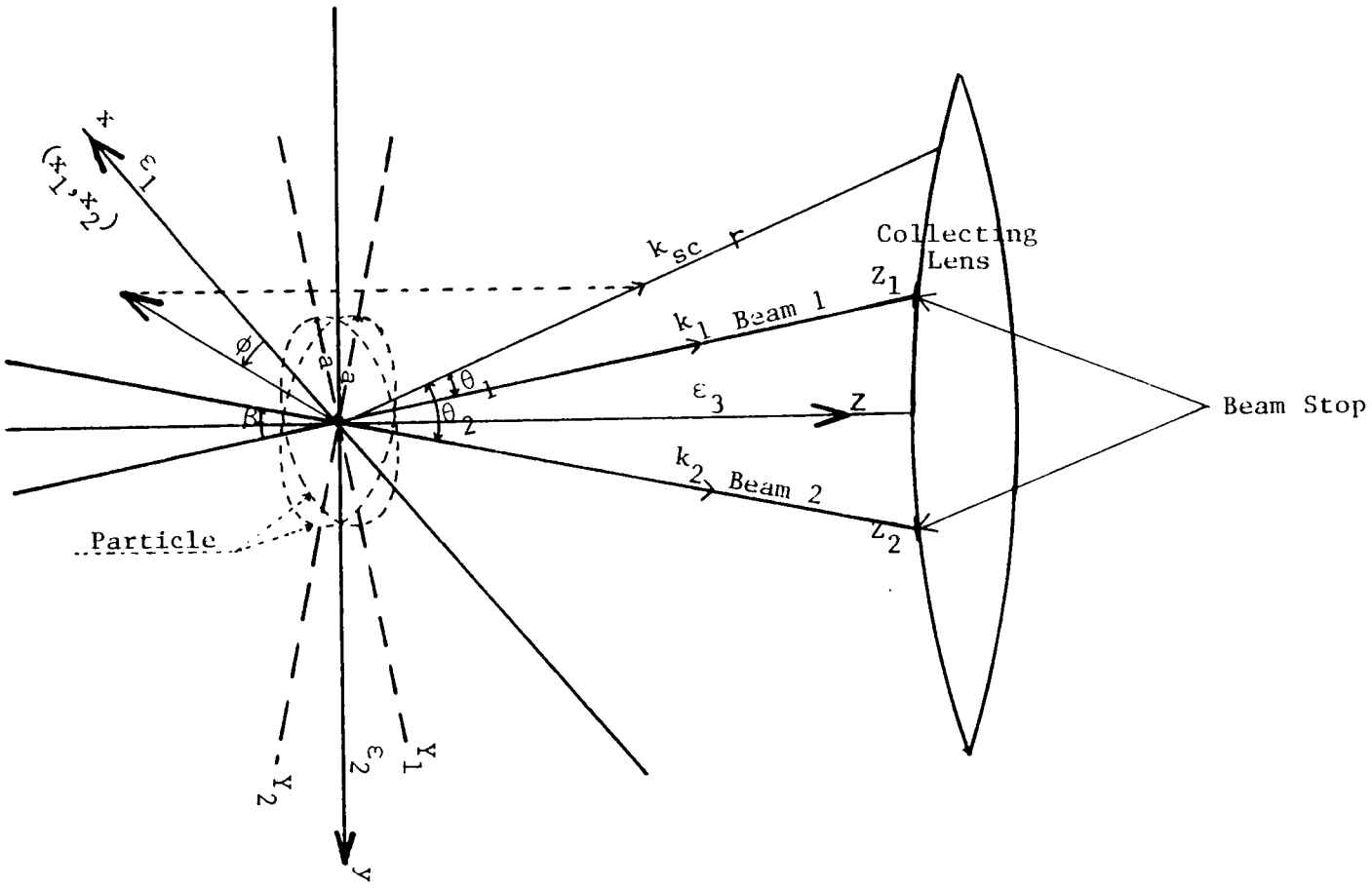

Figure 8. Diffraction by a spherical particle with radius a in the probe volume. Dotted ellipses represent the cross-sectional area of spherical particles to each laser beam. Y_1,Z_1 and Y_2,Z_2 axes lie in the YZ plane.

volume (see figure 5). This visibility multiplies that generated in the scattered light signal, thus creating a lower value of visibility than would be expected on the basis of particle size alone. Thus, the Doppler signal amplitude is reduced. The purpose of this section is to model the variation of Doppler signal magnitude as a function of fringe visibility variation in the probe volume.

The scattered electric field due to diffraction by a circular hole of radius a with beam incidence angle for the vector diffraction theory is given by Jackson.[17] To apply his solution to the case of a spherical particle passing through the two crossed beams, consider two Cartesian coordinate systems x, y_1, z_1 and x, y_2, z_2, which are rotated $+\beta/2$ and $-\beta/2$ about x-axis of x, y, z Cartesian coordinate system as shown in figure 8. Then the diffracted field amplitudes from beam 1 and beam 2 are

$$E_{s1} = E_1 \cdot \frac{ie^{ik_1 r}}{r} a^2 \frac{J_1(ka\sin\theta_1)}{ka\sin\theta_1} (\hat{k}_{sc} x \hat{\varepsilon}_2') \tag{25a}$$

$$E_{s2} = E_2 \cdot \frac{ie^{ik_2 r}}{r} a^2 \frac{J_1(ka\sin\theta_2)}{ka\sin\theta_2} (\hat{k}_{sc} x \hat{\varepsilon}_2'') \tag{25b}$$

where E_1, E_2 are given by Equation 4, k_{sc} is a wave vector of the scattered field, r is the distance between probe volume and a point on the collecting lens surface, θ_1, θ_2 are angles between k_{sc} and the propagation direction represented by a unit vector k_1, k_2 of the laser beams, $\hat{\varepsilon}_2', \hat{\varepsilon}_2''$ are unit vectors in the y_1 and y_2 direction.

In the x, y, z coordinate system, $k_{sc} x \varepsilon_2$ is given by

$$k_{sc} x \varepsilon_2 = (\varepsilon_1 |k_{sc}| \sin\theta\cos\phi + \varepsilon_2 |k_{sc}| \sin\theta\sin\phi + \varepsilon_3 |k_{sc}| \cos\theta) x \varepsilon_2$$

$$= \varepsilon_3 |k_{sc}| \sin\theta\cos\phi - \varepsilon_1 |k_{sc}| \cos\theta \qquad (26a)$$

and

$$|k_{sc} x \varepsilon_2| = |k_{sc}| \ (\sin^2\theta\cos^2\phi + \cos^2\theta) = |k| \ (1 - \sin^2\theta\sin^2\phi). \qquad (26b)$$

Hence, $k_{sc} x \hat{\varepsilon}_2'$ and $k_{sc} x \hat{\varepsilon}_2''$ can be represented by Equation 26 by changing θ,ϕ to θ_1,ϕ_1 and θ_2,ϕ_2, respectively.

The total scattered field is

$$E_s = E_{s1} + E_{s2} = E_1 \cdot \frac{ie^{ik_1 r}}{r} a^2 \frac{J_1(ka\sin\theta_1)}{ka\sin\theta_1} (\hat{k}_{sc} x \hat{\varepsilon}_2')$$

$$+ E_2 \frac{ie^{ik_2 r}}{r_2} a^2 \frac{J_1(ka\sin\theta_2)}{ka\sin\theta_2} (\hat{k}_{sc} x \hat{\varepsilon}_2''). \qquad (27)$$

The intensity of the combined fields due to the diffraction is from Equation 5,

$$I_i = I_o \cdot C_{di}(\theta,\phi) = \frac{1}{\pi b_o^2} k^2 a^2$$

$$\cdot \exp\left[- \frac{2}{b_o^2} (x^2 + y^2\cos^2\beta + Z^2\sin^2\beta)\right]$$

$$\cdot \left[BB + CC + DD \cdot \cos\left(\frac{2\pi y}{\delta}\right) \right] \qquad (28)$$

where

$$BB = P_1 \exp\left(-\frac{2yZ\sin 2\beta}{b_o^2}\right)\left[\frac{J_1(ka\sin\theta_1)}{ka\sin\theta_1}\right]^2 (1 - \sin^2\theta_1\sin^2\phi_1) \tag{29}$$

$$CC = P_2 \exp\left(-\frac{2yZ\sin 2\beta}{b_o^2}\right)\left[\frac{J_1(ka\sin\theta_2)}{ka\sin\theta_2}\right]^2 (1 - \sin^2\theta_2\sin^2\phi_2) \tag{30}$$

$$DD = 2\sqrt{P_1P_2}\left[(1 - \sin^2\theta_1\sin^2\phi_1)(1 - \sin^2\theta_2\sin^2\phi_2) \cdot \frac{J_1(ka\sin\theta_1)}{ka\sin\theta_1} \cdot \frac{J_1(ka\sin\theta_2)}{ka\sin\theta_2}\right]. \tag{31}$$

BB and CC represent the diffractive scattered intensities of beam 1 and beam 2, respectively, and DD represents the intensity caused by interference of beam 1 and beam 2. θ_1,ϕ_1 and θ_2,ϕ_2 are related to θ,ϕ as

$$\theta_1 = \cos^{-1}[-\sin(\beta/2)\sin\theta\sin\phi + \cos(\beta/2)\cos] \tag{32a}$$

$$\theta_2 = \cos^{-1}[\sin(\beta/2)\sin\theta\sin\phi + \cos(\beta/2)\cos] \tag{32b}$$

$$\phi_1 = \cos^{-1}[\sin\theta\cos\phi/\sin\theta_1] \tag{32c}$$

$$\phi_2 = \cos^{-1}[\sin\theta\cos\phi/\sin\theta_2]. \tag{32d}$$

Since the PMT cathode current is proportional to $\int_o^{\theta_{max}}\int_o^{2\pi} I_p d\Omega$ (see section 2.3.4) then

$$i_p \propto \frac{k^2 a^2}{\pi b_o^2} \exp\left[-\frac{2}{b_o^2}(x^2 + y^2\cos^2 + Z^2\sin^2\beta)\right] .$$

$$\int (BB + CC)d\Omega \cdot EE \tag{33}$$

where

$$EE = 1 + \frac{\int DDd\Omega}{\int (BB + CC)d\Omega} \cos\left(\frac{2\pi y}{\delta}\right) . \tag{34}$$

Using Equations 5 and 11, the visibility, V, can be written as

$$V = \frac{2Re(E_1 \cdot E_2^*)}{E_1^2 + E_2^2} . \tag{35}$$

From this definition, it is known that the second term of Equation 34 represents visibility. Symmetry in the problem geometry yields

$$\int \left[\frac{J_1(kasin\theta_1)}{kasin\theta_i}\right]^2 (1 - \sin^2\theta_1\sin^2\phi_1)d\Omega = \int \left[\frac{J_1(kasin\theta_2)}{kasin\theta_2}\right]^2$$

$$\cdot (1 - \sin^2\theta_2\sin^2\phi_2)d\Omega. \tag{36}$$

Hence, EE is rewritten as

$$EE = 1 + \frac{\frac{1}{2\sqrt{P_1P_2}} \int DDd\Omega}{\int \left[\frac{J_1(kasin\theta_1)}{kasin\theta_1}\right]^2 (1 - \sin^2\theta_1\sin^2\phi_1)d\Omega} \cdot FF \cdot \cos\left(\frac{2\pi y}{\delta}\right) \tag{37}$$

where FF is

$$FF = \frac{2\sqrt{P_1 P_2}}{P_1 \exp\left(-\frac{2yZ\sin 2\beta}{b_o^2}\right) + P_2 \exp\left(\frac{2yZ\sin 2\beta}{b_o^2}\right)} . \tag{38}$$

If the collecting lens satisfies the criteria given by Robinson and Chu[18]

$$2L \geq \frac{\lambda d_3}{D}\left(\frac{D}{2\delta} + 1.0\right) \tag{39}$$

where L is the collecting lens radius, D is the particle diameter, and d_3 is the distance between probe volume and collecting lens, then the integral portion of Equation 37 may be represented by the visibility function, V_o, given by Farmer[1]

$$V_o = \frac{J_1(\pi D/\delta)}{\pi D/\delta} . \tag{40}$$

Thus, Equation 38 represents the fringe visibility variation from the visibility given in Equation 40 due to the particle trajectory through the probe volume. Since the expression of the fringe visibility variation is defined at one point, the average fringe visibility variation is the average of visibility in the interval given by the Long Fringe Counter setup.

The rate of fringe visibility variation, ΔV, over the given interval will be defined by performing integration of Equation 38 over the given interval and taking its inverse. Let q and p represent starting and ending points of the integration. In the case when p and q correspond to integration limits that result for the same side of the probe volume, ΔV can be written as:

$$\Delta V = \frac{1}{2\sqrt{P_1 P_2}}\left[\frac{P_1[\exp(4qZ1\cos\beta) - \exp(4pZ1\cos\beta)]}{4Z1(q - p)\cos\beta}\right.$$

$$\left. + \frac{P_2[\exp(-4pZ1\cos\beta - \exp(-4qZ1\cos\beta)]}{4Z1(q - p)\cos\beta}\right] \qquad (41a)$$

when $P_1 \neq P_2$, and

$$\Delta V = \frac{\sinh(4qZ1\cos\beta) - \sinh(4pZ1\cos\beta)}{4Z1(q - p)\cos\beta} \qquad (41b)$$

when $P_1 \simeq P_2$, where Z1 is normalized Z-axis value. When q and p are on different sides of the Z-axis, ΔV is evaluated by changing p in Equation 41 to -p. p and q values will be defined exactly in section 2.3.4. The rate of fringe visibility variation is the value of the constant for multiplying the measured visibility value to obtain the true visibility value.

2.3.4 The Evaluation of Minimum Threshold Power

Not all of the collected light intensity reaches the PMT. This is due to the limited collection aperture (or detector slit) and the optical filter. Light energy (represented by photon energy $h\nu_s$, where h is Planck's constant and ν_s is light frequency) conversion efficiency of the PMT to electrons is also limited. The PMT output current is given by multiplying Equation 33 by the PMT conversion efficiency. (Here only the pedestal term is considered.)

$$i_{PMT} = \frac{I_o G}{h\nu_s}\left(\frac{D}{2}\right)^2 e_c PMTG\varepsilon \qquad (42)$$

where

η = quantum efficiency

e_c = electron charge (1.601×10^{-19} coulomb)

G = scattering gain

PMTG = PMT current gain

D = particle diameter

ε = receiving optics collection efficiency.

For minimum signal current detection, the signal processor is dependent on the signal-to-noise ratio at the PMT output. Amnon Yariv[19] treats this problem in detail. Signal-to-noise power ratio at the PMT output is

$$S/N = \frac{2(Pe\eta/h\nu_s)^2(PMTG)^2}{2(PMTG)^2\, e(\bar{i}_c + i_d)\,\Delta\nu + (4kT_e\Delta\nu/R)} \tag{43}$$

where

P = I_o · scattering gain · collection efficiency

= collected power

i_d = cathode dark current of PMT (about 1×10^{-16} amp)

$\bar{i}_c$ = mean signal current (at the PMT cathode) given by Equation 42 divided by PMTG

$\Delta\nu$ = signal bandwidth

R = PMT output resistance

$4kTe\Delta\nu/R$ = Johnson noise in output resistance.

Since PMTG is usually of the order of $10^5 \sim 10^6$, the Johnson noise term is negligible compared with $2PMTG^2(\bar{i}_c + i_d)\Delta\nu$. Thus, Equation

43 reduces to

$$S/N \simeq \frac{(Pe\eta/h\nu_s)^2}{e(\bar{i}_c+i_d)\Delta\nu} . \tag{44}$$

Hence, the minimum detectable power of the PMT is given by Equation 44; by assuming S/N = 1 and $\bar{i}_c >> i_d$, Equation 44 yields

$$P_{min} \simeq \frac{h\nu_s\Delta\nu}{\eta} . \tag{45}$$

The evaluation of $\Delta\nu$ is given by Schwartz.[20] Assuming the detected signal, f(t), is a Gaussian function, then

$$f(t) = B\exp(-t^2/2\tau^2) \tag{46}$$

where B is a constant. The Fourier transform applied to Equation 46 yields

$$F(\omega) = 2\pi\ \tau B\exp\left[-\omega^2/2(\frac{1}{\tau})^2\right] . \tag{47}$$

The width of $F(\omega)$ is $1/\tau$, i.e., the band width of the signal increases inversely with its temporal width

$$\Delta\nu = \frac{1}{\tau} . \tag{48}$$

Since the probe volume has a Gaussian intensity profile as given in Equation 6, the resulting signal also has a Gaussian amplitude profile as sketched in figure 5b. If this result is expressed as $\exp(-2y^2/b_o^2)$ then

$$\exp(-2y^2/b_o^2) = \exp\left[-y^2/2(\frac{b_o}{2})^2\right] \tag{49}$$

and the width of the signal is given by $b_o/2$. Assuming the particle

velocity is S_p (the PSI measures this velocity), then τ is given as

$$\tau = (b_o/2)/S_p \tag{50a}$$

$$\Delta\nu = \frac{1}{\tau} = \frac{2S_p}{b_o} . \tag{50b}$$

By Equations 45 and 49, the minimum detectable power of a given PMT is

$$P_{min} = \frac{2h\nu_s S_p}{\eta b_o} . \tag{51}$$

Equation 51 shows P_{min} is linearly proportional to particle velocity. However, this is an ideal case. Since the PSI measurement is mainly dependent on the Doppler signal, the Doppler signal power should also exceed P_{min}. Since the Doppler signal is related to the pedestal signal by the visibility, it is possible to relate the minimum intensity of the Doppler signal as a product of a constant, C (an arbitrary constant to match the minimum intensity of the Doppler signal to the signal processor threshold level), visibility, and P_{min}. Therefore, by Equations 38 and 40, minimum power for detection of the Doppler signal $P_{min,dop}$ may be written as

$$P_{min,dop} = CP_{min}/(V_oFF) \tag{52}$$

where V_oFF represents actual visibility at a point on trajectory of particles in the probe volume. By changing the C value, the signal processor threshold value may be obtained.

2.3.5 Calculation of the Maximum Number of Available Signal Fringes

The PSI signal processor requires that the signal have a minimum number of cycles before it is measured. In this section, the maximum number of signal cycles which can be generated as a function of particle size, trajectory through the probe volume, and optical geometry is estimated by a minimum required signal amplitude.

The power reaching the PMT cathode is given as

$$P_{col} = I_o G\pi(\frac{D}{2})^2\varepsilon \ . \tag{53}$$

All factors except I_o are already known. Substituting P_{min} for P_{col} reduces I_o to the minimum detectable intensity:

$$P_{min} = \pi(\frac{D}{2})^2 G\varepsilon I_{omin} \ . \tag{54}$$

Hence, the minimum intensity point detectable in the probe volume is given by

$$I_{omin} = \frac{4P_{min}}{\pi D^2 G\varepsilon} \ . \tag{55}$$

I_{omin} is the probe volume intensity averaged over the particle cross-sectional area which corresponds to the right side of Equation 55. The probe volume intensity distribution is given in Equation 6. Since the Doppler signal is related to the pedestal signal by visibility, only the pedestal terms in Equation 6 need to be calculated to evaluate Equation 55.

Because of the Gaussian intensity variations in the probe

volume, the mean illumination intensity over the particle cross-sectional area should be calculated using integration. Rewriting Equations 6 and 55 and performing the integration yields (To simplify calculation here, integration is done over a square with length D. Since integration is an averaging process, the result should not be much different from that of a circle with diameter D.)

$$\frac{1}{\pi b_o^2}\,\frac{1}{D}\int_{XN-D/2}^{XN+D/2} e^{-\frac{2x^2}{b_o^2}}\,dx\;\frac{1}{D}\int_{YN-D/2}^{YN+D/2}\left[P_1\exp\left[-\frac{2}{b_o^2}(y\cos\theta - Z\sin\theta)^2\right]\right.$$

$$\left. + P_2\exp\left[-\frac{2}{b_o^2}(y\cos\theta + Z\sin\theta)^2\right]\right]dy = \frac{4P_{min}}{\pi D^2 GE} \qquad (56)$$

where XN and YN are x and y axis values, depending on particle trajectory, respectively.

To nondimentionalize the Z direction, let $Z1 = Z\sin\theta/b_o$ then Z1 has a numerical value of 1 when the intensity along the Z axis falls to e^{-2} of the peak intensity. Express XN as a constant multiple of b_o, i.e., $XN = WN \cdot b_o$, and YN as a constant multiple of the fringe period, i.e., $YN = h \cdot \delta$. Then, by substituting Z1 and WN values into Equation 56, the h corresponding to P_{min} may be calculated. The maximum number of bright fringes, N_{max}, is given by

$$N_{max} = 2h + 1 \qquad (57)$$

where 1 is obtained by assuming that the center of the probe volume is a center of the brightest fringe, and the digital fringe counter of the signal processor counts only the positive pulses corresponding to bright fringes (see section 2.3.6). For evaluation of Equation 56, the Simpson Method was used.

Evaluation of the beam waist diameter was given by Dickson[21]; from figure 9a the focused beam waist diameter, r_2, is given by

$$r_2 = \frac{r_o d_2}{d_1}\left[1 + (f_h^2/d_1^2)\right]^{-\frac{1}{2}}\left[1 + \frac{d_1^4}{f_h^2}\left(1 + \frac{f_h^2}{d_1^2}\right)^2 \cdot \left[\frac{1}{d_2^2} - \frac{1}{f} + \frac{1}{d_1[1 + (f_h^2/d_1^2)]}\right]^2\right]^{\frac{1}{2}} \quad (58)$$

where $f_h = \pi r_o^2/\lambda$, when $d_1 = 34.5$ cm, $d_2 = f = 13$ cm, $r_o = .4155 \times 10^{-3}$m, $\lambda = .6328 \times 10^{-6}$m (values applicable to UTSI PSI optical system), r_2 is approximately 63 μm. This will be assumed to be the value of b_o.

2.3.6 Calculation of Mean Signal Amplitude (Mean Pedestal Amplitude)

The calculation of the mean signal amplitude requires the mean intensity of probe volume in a sampled interval specified by the LFC. Since the probe volume has a Gaussian intensity profile, the mean intensity of the probe volume in a sampled interval is dependent on the starting point of integration.

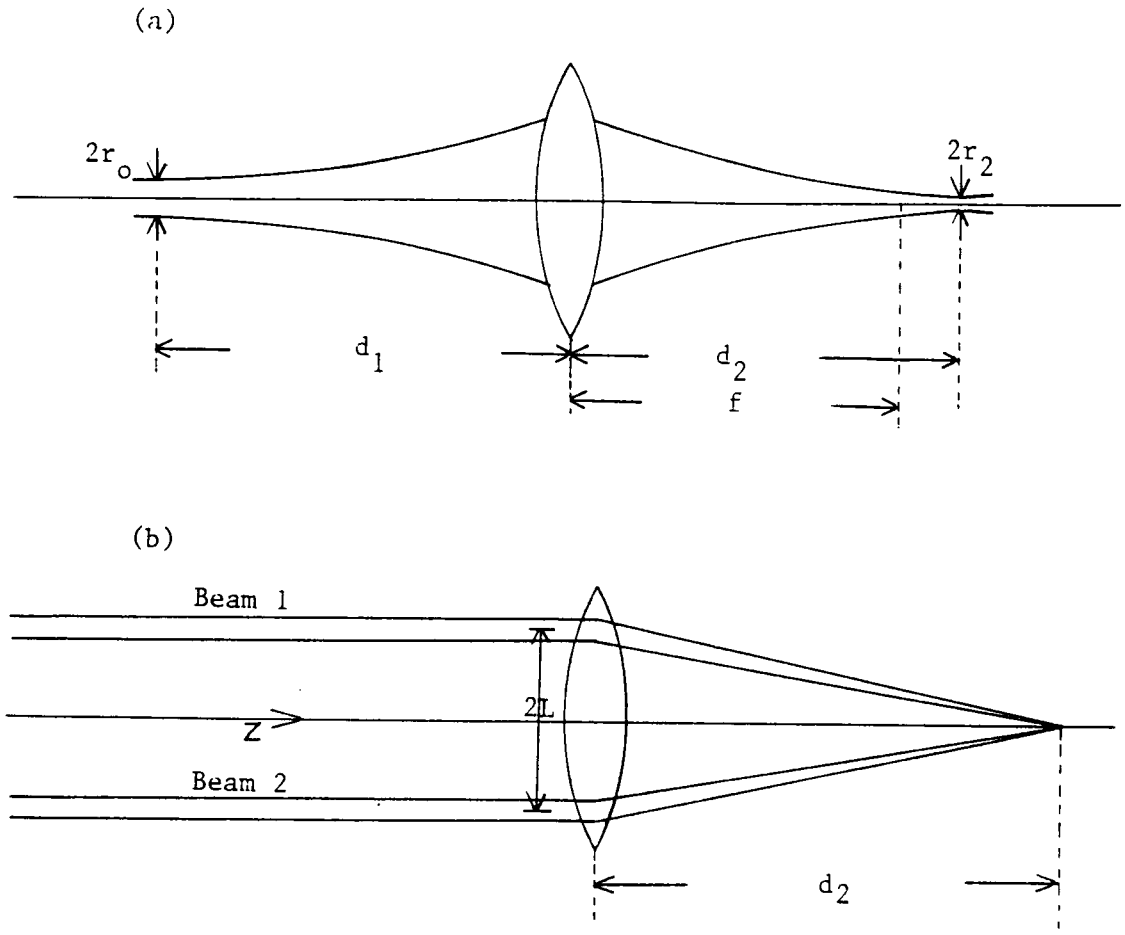

Figure 9. Focusing of Gaussian beam.
(a) One Gaussian beam with beam waist radius r_o a distance d_1 from the lens is focused by a lens with focal length f. The focused point is created at d_2 from the lens. Focused beam diameter is $2r_2$.
(b) Two parallel laser beams incident on the lens are focused to one point (cross-over region at distance d_2 from the lens).

In this section, there is given (1) the evaluation of the starting and ending points of integration in a given fringe setup, and (2) the mathematical expression of mean pedestal amplitude.

As explained in previous sections concerning the evaluation of visibility, the signal processor integrates both Doppler and pedestal signals over the interval given by the LFC. Since the origin of the coordinate system being used is the center of the probe volume, the sum of LFC (N_L) and PC (N_p) should be $N_L + N_p \leq 2h + 1$. When $N_L + N_p \leq h$, the integration interval is located on one side (along the y-axis) of the probe volume; and when $h \leq N_L + N_p \leq 2h + 1$, the integration interval is located on both sides (along the y-axis) of the probe volume. When $N_L + N_p > 2h + 1$, no particle measurement can be made. Therefore, $N_L + N_p$ should always be chosen such that $N_L + N_p \leq N_{max}$. When $N_L + N_p$ is less than h, the starting point of integration is expressed as

$$qb_o = (h + \frac{1}{4})\delta - N_p\delta \tag{59}$$

where $\frac{1}{4}\delta$ term is counted because origin of the coordinate is assumed as the center of the brightest fringe (see figure 10). The ending point of integration is

$$pb_o = qb_o - (N_L - \frac{1}{2})\delta \tag{60}$$

where $-\frac{1}{2}\delta$ term arises because the LFC counts only cycles corresponding to the bright fringes; thus, the last cycle in the LFC is considered one-half. The integration interval is given in Equations 59 and 60;

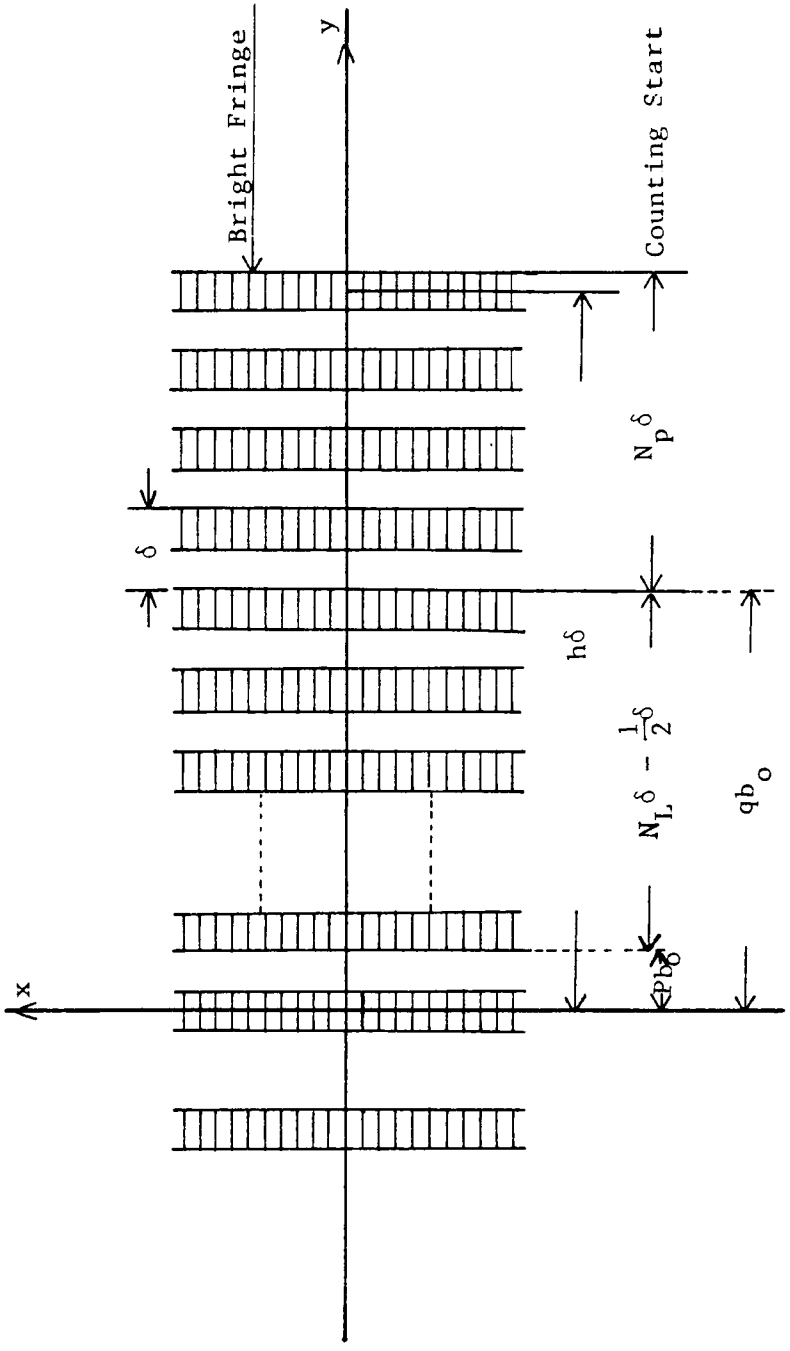

Figure 10. Evaluation of starting and ending point of integration.

thus, in this interval, the mean intensity of the probe volume (Equation 6) may be written as

$$I_{oave} = \frac{1}{2\cos\beta\pi b_o^2 (q-p)D} \int_{XN-\frac{1}{2}D}^{XN+\frac{1}{2}D} \exp\left(-\frac{2x^2}{b_o^2}\right) dx$$

$$\cdot \left[P_1 \left[\int_0^{2(|q|\cos\beta + Z1)} \exp(-y^2)\, dy - \int_0^{2(|P|\cos\beta + Z1)} \exp(-y^2)\, dy \right] + P_2 \left[\int_0^{2(|q|\cos\beta - Z1)} \exp(-y^2)\, dy - \int_0^{2(|P|\cos\beta - Z1)} \exp(-y^2)\, dy \right] \right] \tag{61}$$

Equation 61 can be obtained by making the integration interval of the y-axis in Equation 56 $-qb_o$ to $-pb_o$ and by changing the variables in the exponential to one variable.

Depending on the magnitude of Z1 and $|q|\cos\beta$ and $|p|\cos\beta$, the overall sign of the P_2 term is changed. (Two different sets of I_{oave} are possible.) When $N_L + N_p$ is larger than h but less than 2h,

$$qb_o = (h + \tfrac{1}{4})\delta - N_p \tag{62}$$

$$pb_o = (N_L - \tfrac{1}{2})\delta - qb_o \,. \tag{63}$$

Therefore, in this case,

$$I_{oave} = \frac{1}{2\cos\beta\pi b_o^2(q+p)D} \int_{XN-\frac{1}{2}D}^{XN+\frac{1}{2}D} \exp\left(-\frac{2x^2}{b_o^2}\right) dx$$

$$\cdot P_1 \int_o^{2(|q|\cos\beta + Z1)} \exp(-y^2)\, dy + \int_o^{2(|P|\cos\beta - Z1)}$$

$$\cdot \exp(-y^2)\, dy + P_2 \int_o^{2(|q|\cos\beta - Z1)} \exp(-y^2)\, dy$$

$$+ \int_o^{2(|P|\cos\beta + Z1)} \exp(-y^2)\, dy \qquad (64)$$

according to the values of Z1 and $|q|\cos\beta$ and $|p|\cos\beta$, $|q|\cos\beta - Z1$ and $|p|\cos\beta - Z1$ have plus or minus values; so, four different sets of I_{oave} are possible. When $N_p\delta$ is larger than h, Equation 61 may be applied to solve I_{oave}. By combining Equations 42 and 61,

$$i_{PMT} = \frac{G\eta De_c PMTG\varepsilon}{4 \quad 2\cos\beta b_o^2(q-p)h\nu_s} GG \qquad (65)$$

where GG represents the integral part of Equation 61. Since $q - p = (N_L - \frac{1}{2})\delta/b_o$, substituting this relationship into Equation 65 yields

$$i_{PMT} = \frac{G\eta e_c PMTG\varepsilon GG}{4\sqrt{2}\cos\beta(N_L - \frac{1}{2})\delta h\nu_s} \frac{D}{b_o} . \quad (66)$$

Mean pedestal voltage amplitude, V_p, is obtained by multiplying PMT output impedance, R, and overall signal processor gain, G_s, by Equation 66 to obtain

$$V_p = \frac{RG_s G\eta e_c PMTG\varepsilon GG}{4\sqrt{2}\cos\beta(N_L - \frac{1}{2})\delta h\nu_s} \frac{D}{b_o} . \quad (67)$$

For the evaluation of GG, an approximation given by Menzel[22] is used:

$$\int_o^a e^{-bx^2} dx \simeq \frac{1}{2}(\frac{\pi}{b})^{\frac{1}{2}} (1 - e^{-4ba^2/\pi})^{\frac{1}{2}} . \quad (68)$$

A PMT is a special kind of vacuum tube. If the signal intensity exceeds a certain limitation given as the limiting voltage divider current, then the PMT is saturated. When this occurs in PSI operation, increased collected intensity, i.e., increased particle diameter, no longer increases the PMT output. Thus, above a certain size range which causes PMT saturation, pedestal amplitude cannot give a valid correlation with particle size. Saturation characteristics are well described by Ross.[23]

3. RESULTS OF THE COMPUTATIONS

In this section, the results of the computations using the equations developed in section 2 are applied to a specific optical geometry found in a UTSI PSI optical system (see figure 11).

Section 3.1 gives the characteristics of the UTSI PSI optical system shown in figure 11 and the signal processor setup condition. Sections 3.2 through 3.5 will treat the results. For computational purposes, all particles are assumed to be spherical and transparent.

3.1 Characteristics of the PSI Optical System and Setup

The following is a list of experimental characteristics of the PSI optical system which has been analyzed.

1. Source of laser power - 5mW;
2. Wavelength of source laser - 0.6328 μm;
3. F-number of collecting lens - 1.5;
4. Distance between the probe volume and the center of the collecting lens -
5. Transmittance of the transmitting lens - 0.86;
6. Collection efficiency of receiving optics - 0.08725;
7. Scattered light collection lens position - centered on bisector between the beams;
8. Power of beam 1 and beam 2 - 2mW and 2.3 mW, respectively;
9. PMT gain - 2.0×10^5 to 7.1×10^5;
10. Quantum efficiency of PMT - approximately 0.02 at λ = .6328 μm;

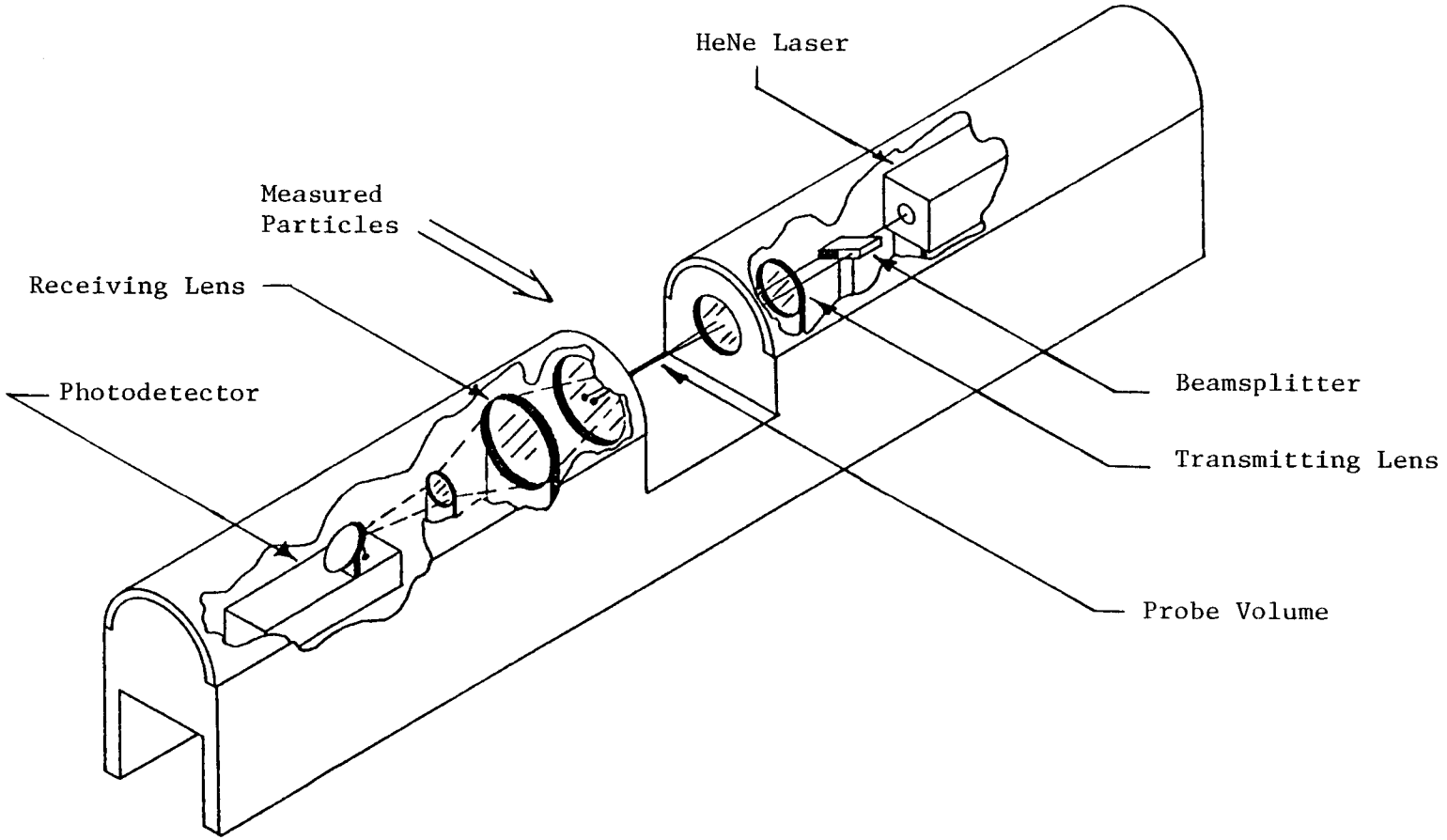

Figure 11. PSI Optical System.

11. PMT output impedance - 50 ohms;

12. Overall gain of signal processor - approximately 20,000;

13. Peak amplitude of signal processor output - 10V.

The power difference between beam 1 and beam 2 is caused by beam splitter limitation.

The operating conditions of the PSI are:

1. Fringe period - 6 μm;

2. Signal processor electronics parameters:

   a. Long Fringe Counter - 13;

   b. Short Fringe Counter - 7;

   c. Precounter - 8;

   d. Signal threshold level - 0.2×10^{-12}(w).

3. Beam stop diameters - 6 mm (circular);

4. Calibration particle diameter - 0.624 μm, 1.01 μm, 3.01 μm;

5. Particle used - Polystyrene Latex (PSL) spheres diluted with 95% ethyl alcohol.

Signal threshold level is determined from experimental data giving the lowest amplitude. Below 1 μm particle diameter, the geometrical optics theory and diffraction theory yield marginally accurate results. However, it will be applied to the calculation of the scattering gain in this size range.

3.2 Computation of the Scattering Gain

The diffractive scattering intensity coefficient (Equation 21) evaluated by numerical methods developed in Appendix A yields a

diffractive scattering gain larger than 1 as the particle size increases to above 19 μm, even if 1024 evaluation points are used. (Diffractive scattering gain should be less than 1.) This is mainly because the intensity distribution of the Airy pattern (characterized by the function $(2J_1(x)/x)^2$) has its principle maximum, 1, at x = 0; and with increasing x, it oscillates with gradually diminishing amplitude. Therefore, the diffractive scattering gain is evaluated by the simplified method formulated in Equation 20c.

For purposes of comparison, the case without beam stops (Equation 24) was evaluated by a numerical method. Figures 12 and 13 represent the computed results of diffractive scattering gain by the simplified method and the numerical method, respectively. To measure the effect of the collecting lens F-number on the diffractive scattering gain, the diffractive scattering gain for F-number 2.0 was also computed (see figure 13). From figures 12 and 13, it is seen that:

1. When the F-number is 1.5, both methods show reasonable agreement. Equation 21 yields a diffractive scattering gain which is a little higher than that of Equation 20c. This difference is almost negligible compared with the actual gain. It appears that the small differences in the lower size ranges result from difference in the evaluation methods and polarization effects in Equation 23. From this comparison, it is concluded that Equation 21c is a good approximation for the diffractive scattering gain in the configuration of interest.

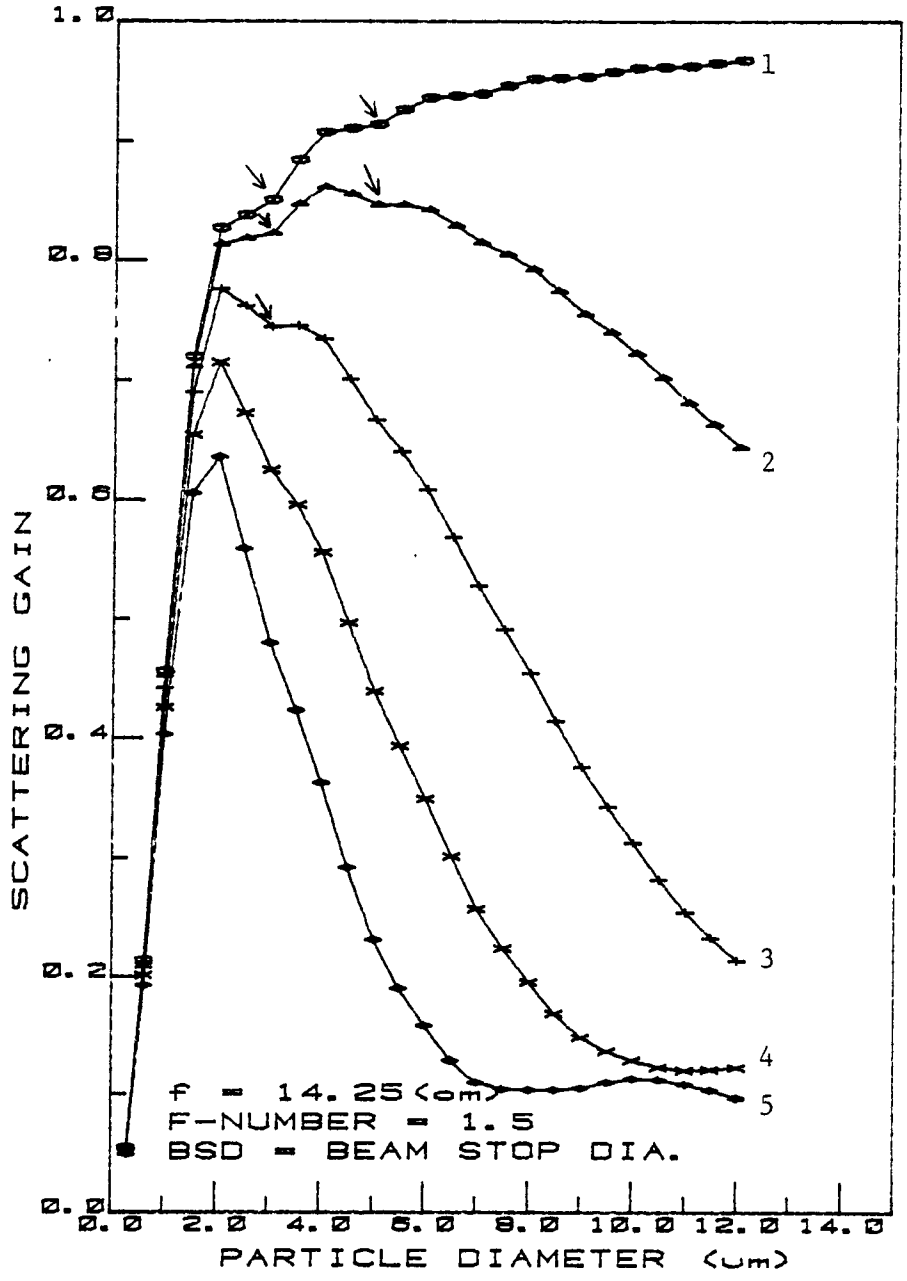

Figure 12. Diffractive scattering gain (using simplified method).

1: No beam stop
2: BSD = 3 mm
3: BSD = 6 mm
4: BSD = 9 mm
5: BSD = 12 mm
Arrows represent perturbation

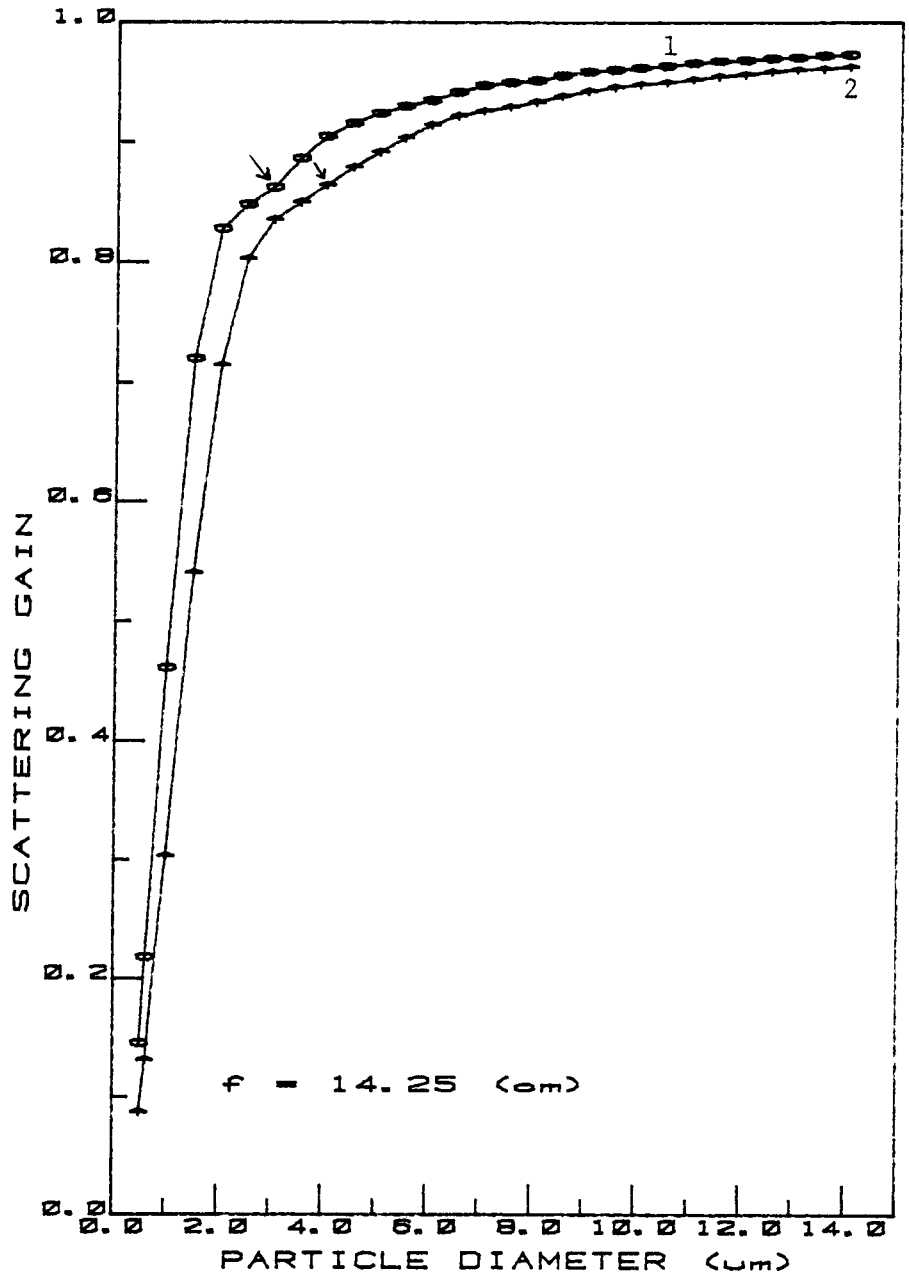

Figure 13. Diffractive scattering gain (using numerical method) with no beam stops.

1: F-number = 1.5
2: F-number = 2.0
Arrows represent perturbation

2. When the F-number is 1.5, both methods give perturbations in the curve at a size of 3 μm. However, when the F-number is 2.0, this perturbation appears at the 4.0 μm size although it is negligible. Apparently, this effect is caused by the characteristics of the diffractive scattering intensity function.

3. The difference between the diffractive scattering gain for F-numbers of 1.5 and 2.0 is significant only when particle size is smaller than 2.0 μm.

4. As the particles become large, the diffractive scattering gain is largely dependent on the beam stop diameters. When the beam stop diameters become larger than 6 mm, diffractive scattering gains have negative slopes for sizes greater than 2.0 μm.

5. As the particles become large, the diffractive scattering gain approaches 1 for the no beam stop case.

From these results, it is concluded that the diffractive scattering gain is largely dependent on the beam stop diameters rather than on the collecting lens F-number when the particle becomes larger.

The refractive and reflective scattering gain was calculated by the numerical method. In this case, only 64 evaluation points were used. The result is almost the same as that for a 1024 point evaluation. Since refractive and reflective scattering intensity coefficients are not dependent on particle size (as shown in Equations 16a,b and 18), the computation was performed for various F-numbers. For purposes of comparison, several other particle cases were also considered.

Figure 14 shows the refractive scattering gain. From this figure, it is seen that the refractive scattering gain is more dependent on the index of refraction of the particle than on the F-number. This calculation shows that the effects of beam stops are negligible. For example, in the case of water (index of refraction is 1.33), the difference of the refractive scattering gain between no beam stops and beam stops (1.2 cm diameter) for F-number 1.5 is only 0.0135 (.31277 to .29925) by Equation 16b and 0.0133 (0.30821 to 0.29494) by Equation 16a. In the case of the index of refractions used here, the relative magnitude of the difference is less than 5%; thus, beam stop effects can be neglected.

The refractive scattering gain is neglected in this calculation because it is so small compared to the other two scattering gains. For example, in the case of an F-number of 1.25 and on-axis observation geometry, the reflective scattering gain of PSL (index of refraction of 1.5985 at λ = .6328 μm) is 0.014; that of the refractive scattering gain is 0.205. Hence, the refractive scattering gain will be neglected for the given beam stop diameters (6 mm, twin circular).

It is noteworthy that, as the index of refraction of a particle approaches 1 and the collector F-number becomes small, the refractive gain becomes comparable to the diffractive scattering gain. Since the maximum possible diffractive scattering gain is 1, the refractive scattering gain becomes the dominant factor as beam stop diameters increase in size.

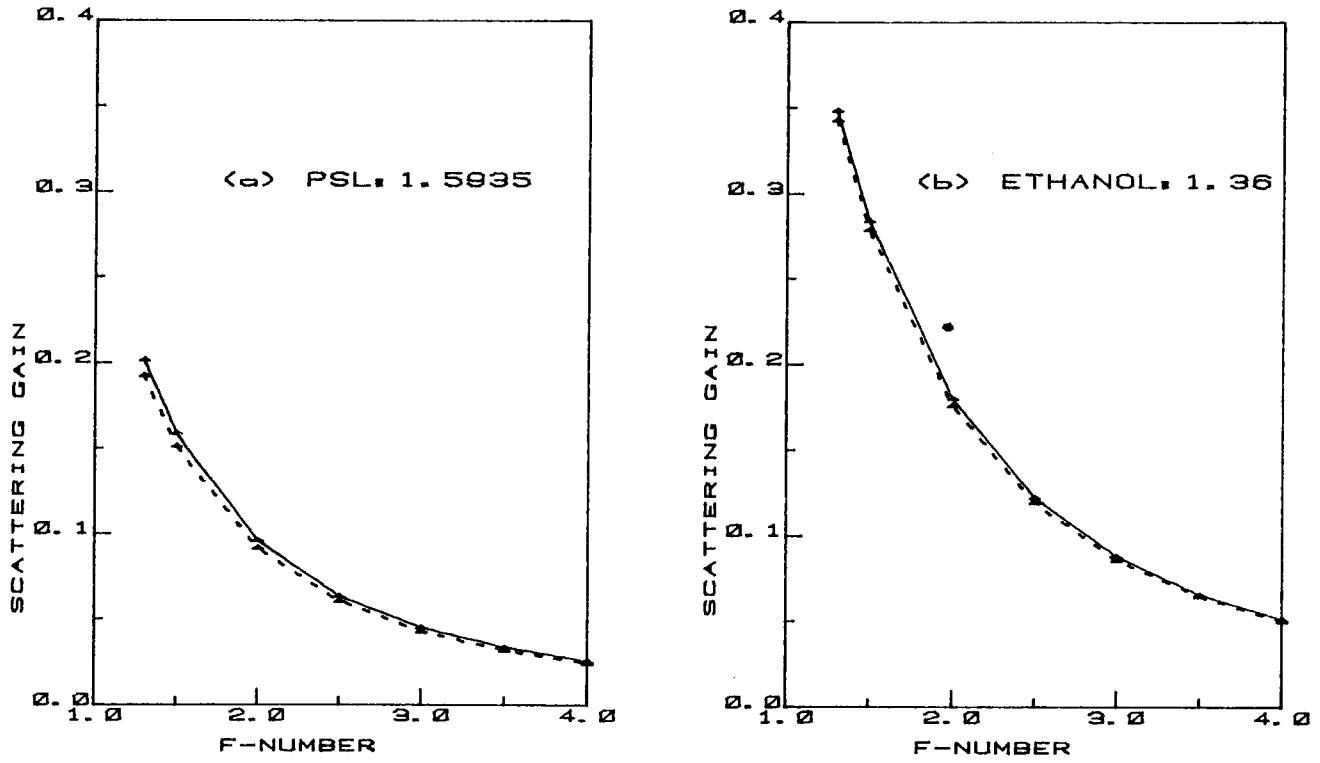

Figure 14. Refractive scattering gain in various F-numbers and particulate materials. Dash-line (Hodkinson), straight-line (Bachelo).

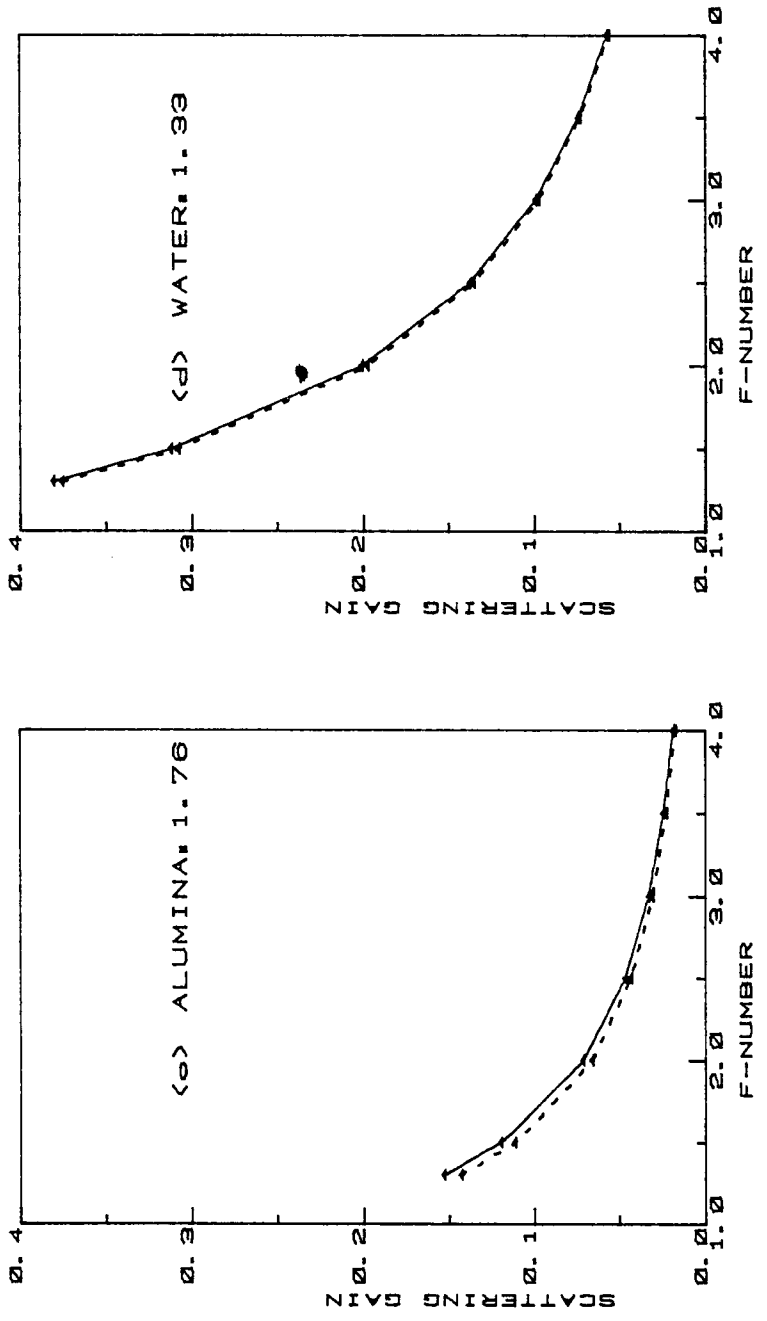

Figure 14. (Continued).

The total scattering gain is calculated by totaling the diffractive and refractive scattering gains. For example, the total scattering gain of a 3 μm diameter PSL sphere and an F-number 1.5 collector with 6 mm beam stops is determined from figures 11 and 12. The diffractive scattering gain is 0.8499, and the refractive scattering gain is 0.15. Thus, the total scattering gain is given by 0.8499 + 0.15 = 0.9999.

3.3 Computation of the Maximum Number of Signal Cycles (N_{max})

For calculation of N_{max} corresponding to the particle incidence position to the probe volume, several assumptions were made.

1. All particles are normally incident to the cross-section of the probe volume and maintain the trajectory through the volume (i.e., there are no drag or background turbulence effects).

2. The Doppler signal threshold is the same as the pedestal signal threshold (i.e., c = 1).

3. The geometric center of the probe volume is located at the focal plane of the transmitting lens, i.e., the interference fringes are parallel to the Z-axis (this assumption has been discussed by Hanson[24]).

4. The PMT slit (aperture) is imaged perfectly at the geometric center of the probe volume.

5. There are no noise contributions from the signal processor electronics.

Under these assumptions, the probe volume cross-sectional area was divided into meshes by specifying an incremental normalized Z-axis value, Z1, and x-axis values, WN. Using Equations 56 and 52, N_{max} was calculated for given size particles and for velocities 4.5 m/sec. and 6.5 m/sec., respectively. These are tabulated in Table 1 for Z1 values between 0.0 and 2.0 and WN values between 0.0 and 1.5.

From Table 1, it is observed that:

1. When WN = 0.0, Z1 = 0.0, N_{max} for 0.624 μm, 1.09 μm, 2 μm, and 3 μm size particles are 41, 45, 49, and 49 at 4.5 m/sec., 39, 43, 47, and 49 at 6.5 m/sec., respectively. In the case of 3 μm, this progression appears equivalently for WN = 0.5 b_o, Z1 = 0.0.

2. The minimum required signal cycles for fringe counters of this setup are 21 (LFC + PC = 13 + 8). When WN = 1.5, Z1 values which will satisfy this requirement are Z1 = 0.6, 1.1, 1.4, and 1.5 for velocity 4.5 m/sec. and 0.4, 1.0, 1.3, and 1.45 for velocity 6.5 m/sec. for 0.624 μm, 1.09 μm, 2 μm, and 3 μm particles, respectively. If these points are plotted for each particle size, the cross-sectional are of the probe volume for each particle size can be calculated for a given setup of signal processor constraints.

3. If geometrical optics and diffraction theory can be applied to particle diameters below 1 μm (at λ = 0.6328 μm), then it can be said that the signal processor fringe setup is acceptable. Application of these theories to particles with diameters below 1 μm is possible by decreasing the wavelength of the source light to

TABLE 1

MAXIMUM NUMBER OF SIGNAL CYCLES (N_{max})

PD	WN \ Z1	0.0	0.2	0.4	0.6	0.8	1.0	1.2	1.4	1.6	1.8	2.0
0.624 µm	0.0	39	39	39	37	35	33	31	27	21	11	
		41	41	37	39	37	35	31	27	23	13	
	0.5	37	37	37	35	33	31	29	23	17		
		39	39	37	37	35	33	29	25	19	9	
	1.0	33	33	33	31	29	25	21	15			
		35	35	33	31	29	27	23	17			
	1.5	23	23	21	19	17	11					
		25	25	23	21	19	13					
1.09 µm	0.0	43	43	43	41	41	39	35	33	27	21	13
		45	45	43	43	41	39	37	33	29	21	15
	0.5	43	43	41	41	39	37	35	31	25	19	
		43	43	43	41	41	37	35	31	27	19	10
	1.0	39	39	37	37	35	33	29	25	19		
		39	39	39	37	35	33	31	27	21	11	
	1.5	31	29	29	27	25	21	17				
		31	31	31	29	27	23	19	11			
2 µm	0.0	47	47	47	45	45	43	41	37	33	29	21
		49	47	47	47	45	43	41	39	35	29	23
	0.5	45	45	45	43	43	41	39	35	31	27	19
		47	47	47	45	43	43	39	37	33	27	21
	1.0	43	43	41	41	39	37	35	31	25	19	
		43	43	43	41	39	37	35	31	27	21	11
	1.5	35	35	35	33	31	29	25	19	11		
		37	37	35	35	33	29	27	21	13		
3 µm	0.0	49	49	47	47	45	43	41	39	35	31	25
		49	49	49	47	47	45	43	39	37	31	27
	0.5	47	47	47	45	45	43	41	37	33	29	23
		49	49	47	47	45	43	41	39	35	31	23
	1.0	43	43	43	43	41	39	35	33	29	23	13
		45	45	45	43	41	39	37	33	29	25	15
	1.5	37	37	37	35	33	31	27	23	15		
		39	37	37	37	35	31	29	25	19		

NOTE: Lower portion numbers: 4.5 m/sec.
Upper portion numbers: 6.5 m/sec.
Blank region represents $N_{max} \leq 7$.

obtain the same $\pi D/\lambda$ values where the theory is known to be accurate.

4. N_{max} is almost the same in the cases of WN = 0.5 for 0.624 μm and WN = 1.5 for a 3 μm particle diameter.

From these results, it is concluded that N_{max} and thus the equivalent cross-sectional area of the probe volume for each size particle is dependent on its velocity. As particle size becomes large and/or velocity decreases, the cross-sectional area increases, i.e., the detection probability of the signal processor is increased. Thus, to find the actual size distribution from PSI data, the PSI data should be weighted to give some detection probability for each size particle. The weighting factors will be dependent upon particle velocity and particle size.

3.4 Computation of Interference Fringe Variation

The visibility values used here are calculated from Equation 40 by dividing the size range given by the fringe period into twenty equal incremental diameters ($\delta/20$). These are represented as the diagonal values of figure 15. The values above the diagonal in figure 15 represent the rates of fringe visibility variation. ($c_{i,j} = a_{ii}/b_{jj}$; here, a, b, and c represent matrix elements and subscripts represent the number of row and column, $j \geq i$.) For example, the value in row 3, column 12, 1.575 represents the ratio of the visibility value in row 3, column 3, .972 to the visibility value in row 12, column 12, .675 (1.575 = .972/.675). This means that a particle with actual size ($3\delta/20$) passing through the probe

RATE OF FRINGE VISIBILITY VARIATION

	1	2	3	4	5	6	7	8	9	10	11	12	13	14	15	16	17	18	19	20	21
1	.997 (1)	1.01	1.03	1.05	1.08	1.12	1.17	1.22	1.3	1.38	1.49	1.62	1.77	1.97	2.25	2.54	2.96	3.52	4.32	5.51	
2		.988 (2)	1.02	1.04	1.07	1.11	1.15	1.21	1.28	1.37	1.48	1.60	1.76	1.95	2.23	2.51	2.93	3.49	4.28	5.46	
3			.972 (3)	1.02	1.05	1.09	1.14	1.19	1.26	1.35	1.45	1.58	1.73	1.92	2.19	2.47	2.88	3.44	4.21	5.37	
4				.951 (4)	1.03	1.07	1.11	1.17	1.24	1.32	1.42	1.54	1.69	1.88	2.14	2.42	2.82	3.36	4.12	5.25	
5					.925 (5)	1.04	1.08	1.13	1.20	1.28	1.38	1.50	1.65	1.83	2.08	2.35	2.75	3.27	4.00	5.11	
6						.893 (6)	1.04	1.10	1.16	1.24	1.33	1.45	1.59	1.77	2.01	2.27	2.65	3.16	3.87	4.93	
7							.856 (7)	1.05	1.11	1.19	1.28	1.39	1.52	1.69	1.93	2.18	2.54	3.03	3.71	4.73	
8								.815 (8)	1.06	1.13	1.22	1.32	1.45	1.61	1.84	2.07	2.42	2.88	3.53	4.50	
9									.770 (9)	1.07	1.15	1.25	1.37	1.52	1.73	1.96	2.29	2.72	3.33	4.25	
10										.722 (10)	1.08	1.17	1.29	1.43	1.63	1.84	2.14	2.55	3.13	3.99	
11											.670 (11)	1.09	1.19	1.32	1.51	1.71	1.99	2.37	2.90	3.70	
12												.617 (12)	1.10	1.22	1.39	1.57	1.83	2.18	2.67	3.41	
13													.562 (13)	1.11	1.27	1.43	1.67	1.99	2.43	3.11	
14														.506 (14)	1.14	1.29	1.50	1.79	2.19	2.80	
15															.444 (15)	1.13	1.32	1.57	1.92	2.45	
16																.393 (16)	1.17	1.39	1.70	2.17	
17																	.337 (17)	1.19	1.46	1.86	
18																		.283 (18)	1.23	1.56	
19																			.231 (19)	1.28	
20																				.181 (20)	
21																					(21)

EQUIVALENT RATE OF FRINGE VISIBILITY VARIATIONS
FOR EACH SIZE OF PARTICLE

Figure 15. Visibility table and the rate of fringe visibility variation.

volume with a $Z \neq 0$ trajectory corresponding to $\Delta\nu = 1.575$ is classified by the signal processor as a particle with size $(12\delta/20)$.

The visibility function given in Equation 40 can be applied to any values of the fringe period in which the particle size is ratioed to the fringe period. Visibility values below 0.181 are classified as an uncertainty region.[16] Therefore, the particles within the size increment given for the function of particle diameter to fringe period fall into a region of uncertainty defined by the fringe visibility variation. The rate of visibility variation corresponding to the starting point of integration, qb_o, is plotted in figure 16. (The numbers on each curve in the figure are calculated from Equation 59 by dividing both sides by δ. Here, let Q be the beginning point of the integration and let the corresponding end point be P.)

From figure 16, it can be seen that the fringe visibility variation (depending on the starting point of integration) has the following characteristics.

1. Since LFC = 13 is the setup for this paper, Q = 6.25 (corresponding to h = 14) represents the symmetrical case, i.e., P = Q. In this case, the rate of fringe visibility variation is less than 2 up to Z1 = 0.9 and less than 5.91 up to Z1 = 1.6.

2. The rate of fringe visibility variation increases with the increasing value of either P or Q.

3. Any power differences between beam 1 and beam 2 introduce fringe visibility variations. This variation is increased with increasing difference between P and Q. For example, at Z1 = 1.2,

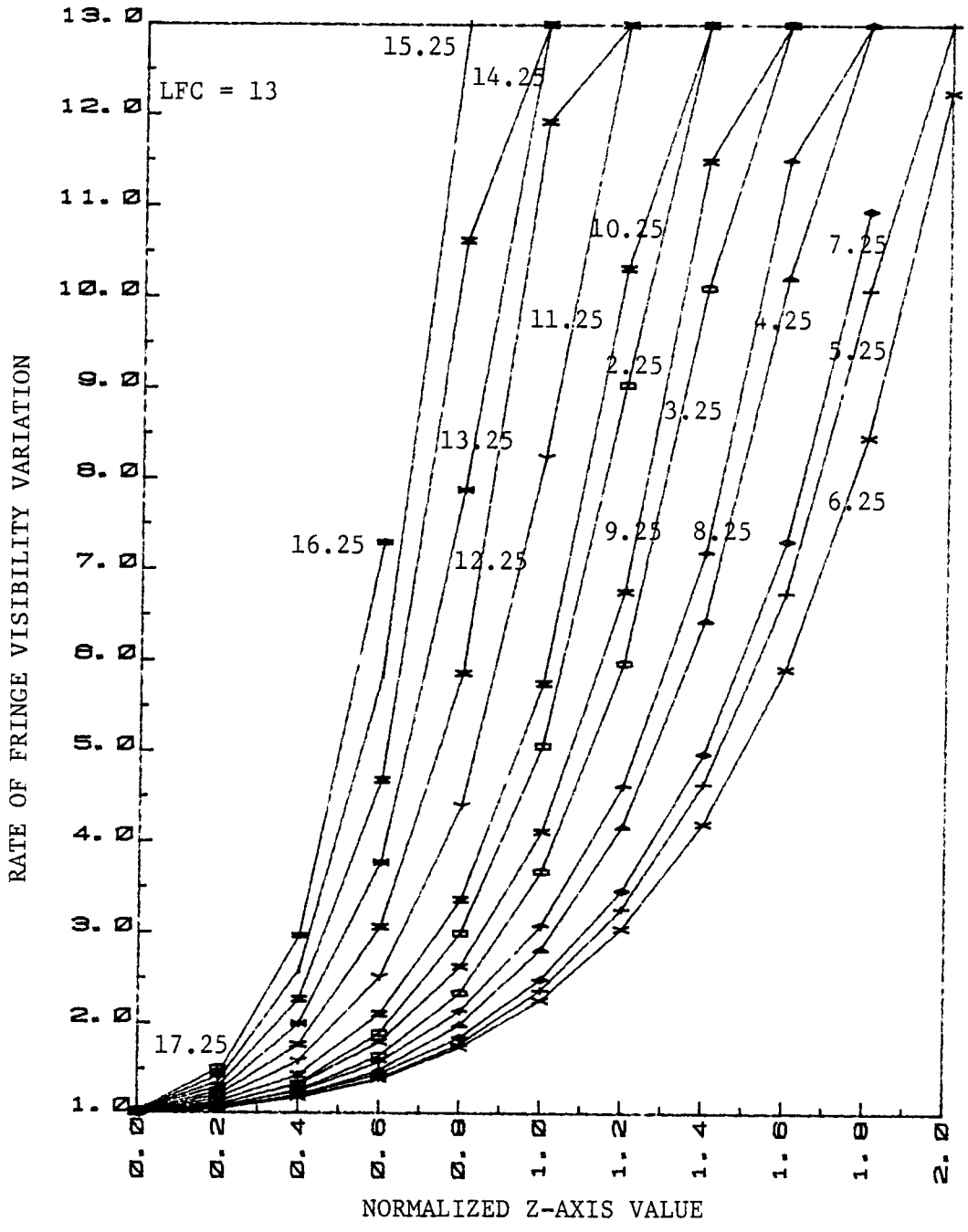

Figure 16. The rate of fringe visibility variation with starting point of integration. The number on each line represents starting point of integration.

the difference in the rates of fringe visibility variation between Q = 10.25 and 2.25, and between Q = 9.25 and 3.25, is 1.28 and 0.78, respectively. If Z has negative values, these differences become negative values. Q = 2.25 corresponding to h = 10 corresponds to the minimum required signal cycles for this fringe counter setup.

4. When Z1 is greater than 1.6, all sizes of particles will fall in the uncertainty region due to the fringe visibility variation.

5. The probability of the visibility being less than 0.181 (the uncertainty region) is dependent on Q values at the given Z1 value. Q = 17.25 (corresponding to h = 2.5) is a maximum value for the particle size range within δ.

Since the visibility values for 0.624 μm, 1.09 μm, 2 μm, and 3 μm calculated from Equation 40 are 0.986, 0.960, 0.870, and 0.722, respectively, then from Table 1 and figure 16 the particle size dependence of the rates of visibility variation is as follows.

1. In the case of a 0.624 μm particle diameter throughout the entire probe volume cross-sectional area, the probability of falling in the uncertainty region is low for both velocities which have been considered.

2. In the case of 1.09 μm particle diameters passing through the region WN $\leq$ 0.5, Z1 $\geq$ 0.8 (at 4.5 m/sec.), Z1 $\geq$ 0.9 (at 6.5 m/sec.), the results show a strong probability of signals having visibilities below 0.181.

3. In the case of 2 μm particle diameters passing through the region WN $\leq$ 0.5, Z1 $\geq$ 0.6 (at 4.5 m/sec.), Z1 $\geq$ 0.7 (at 6.5 m/sec.), the results show a strong probability of signals having visibilities below 0.181.

4. In the case of 3 μm particle diameters, a strong probability of visibility below 0.181 appears when its trajectory passes through the region bounded by WN $\leq$ 1.0, Z1 $\leq$ 0.5 for both velocities considered here.

5. All the cases, although there are some differences in powers of beam 1 and beam 2, do not introduce appreciable fringe visibility variations at Z1 = 0.0.

From these results, it is concluded that, for a given particle size increment, the probability of generating spuriously low visibility values increases with increasing particle diameter and decreasing particle velocity.

3.5 Computation of Mean Pedestal Amplitude

In addition to the assumptions given in section 3.3, one more assumption was used for the calculation of the mean pedestal amplitude, i.e., the PSI signal processor responds only to the signal amplitude higher than that detected for the first cycle of the Precounter.

This is a reasonable assumption since Equation 61 represents an average intensity of some interval of a Gaussian profile specified by LFC. On the other hand, the signal processor responds

only to a certain intensity point in the probe volume which corresponds to the signal processor threshold level. Therefore, the intensity level below that of the first cycle of the Precounter was subtracted from the average intensity computed from Equation 61. By these assumptions, the mean signal amplitude corresponding to N_{max} is computed over the interval given by the LFC setup from Equation 67. The mean pedestal amplitude corresponding to each value of Z1 and WN is plotted in the logarithmic voltage scale versus visibility graph by giving expected visibility values to each evaluation trajectory. These results are illustrated in figures 17a,b through 20a,b for particle sizes of 0.624 μm, 1.09 μm, 2 μm, and 3 μm at velocities 4.5 m/sec. (a) and 6.5 m/sec. (b). The expected visibility value is calculated by dividing the visibility values used here by the rate of fringe visibility variation for each evaluation trajectory. Thus, points on each WN curve in these figures correspond to Z1 values 0.0, 0.2, 0.4, and etc., from right to left.

From these figures, it is observed that:

1. When the velocity is 4.5 m/sec., the possible mean pedestal amplitude voltage ranges of 0.624 μm, 1.09 μm, 2 μm, and 3 μm size particles are -0.71 ~ -3.0, -0.31 ~ -2.43, 0.36 ~ 1.91, and 0.70 ~ -1.78, respectively. Similar mean pedestal amplitude levels appear for (1) WN = 0.5 of .624 μm, WN = 1.0 of 1.09 μm, and WN = 1.5 of 3 μm particle diameters; (2) WN = 0.5 of 1.09 μm, and WN = 1.0 of 2 μm particle diameters.

2. When the velocity is 6.5 m/sec., the possible mean pedestal

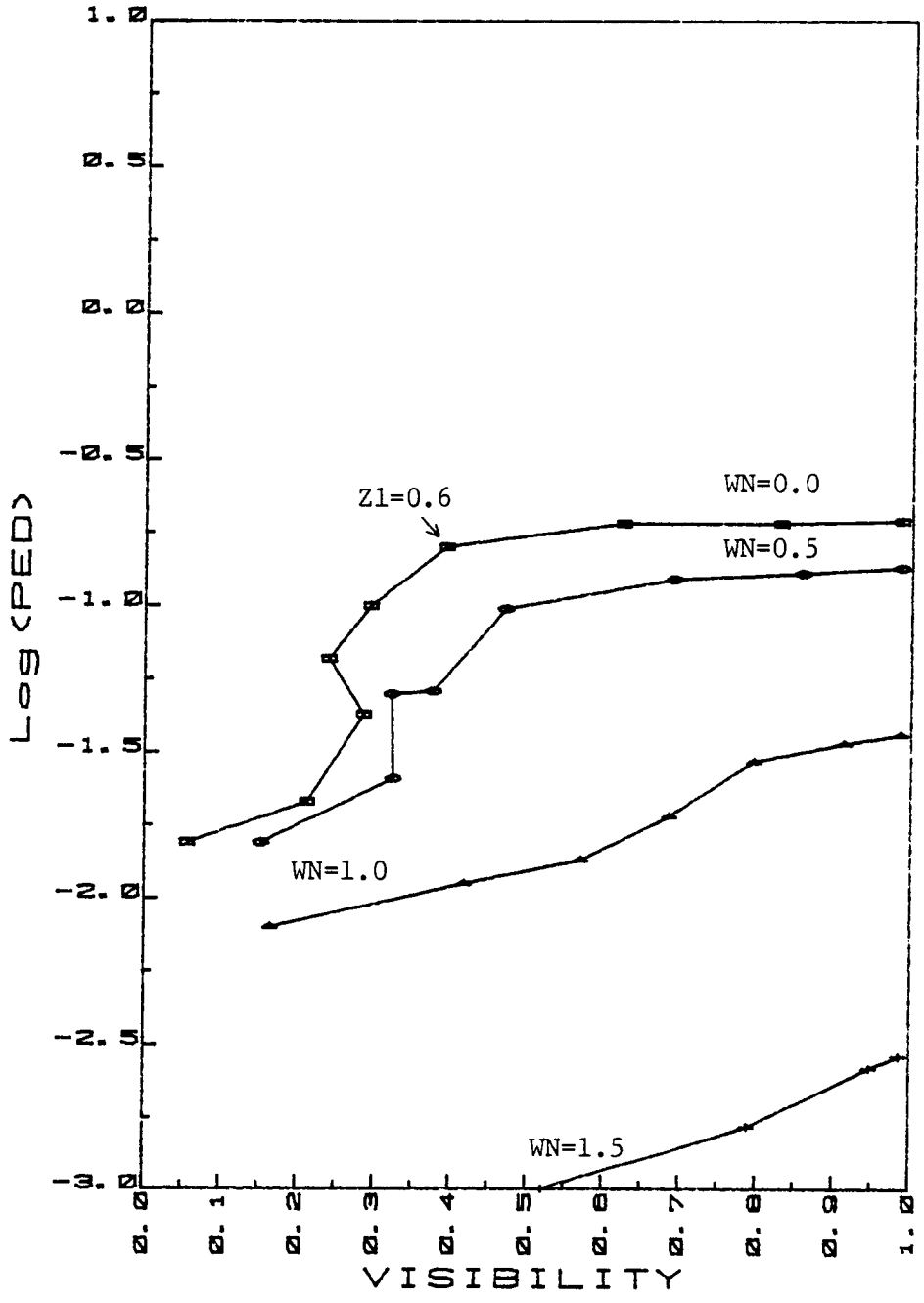

(a) Velocity: 4.5 m/sec.

Figure 17. Mean pedestal amplitude of 0.624 μm PSL particle. Points on each WN curve represent Z1 values 0.0, 0.2, 0.4, etc., from right to left.

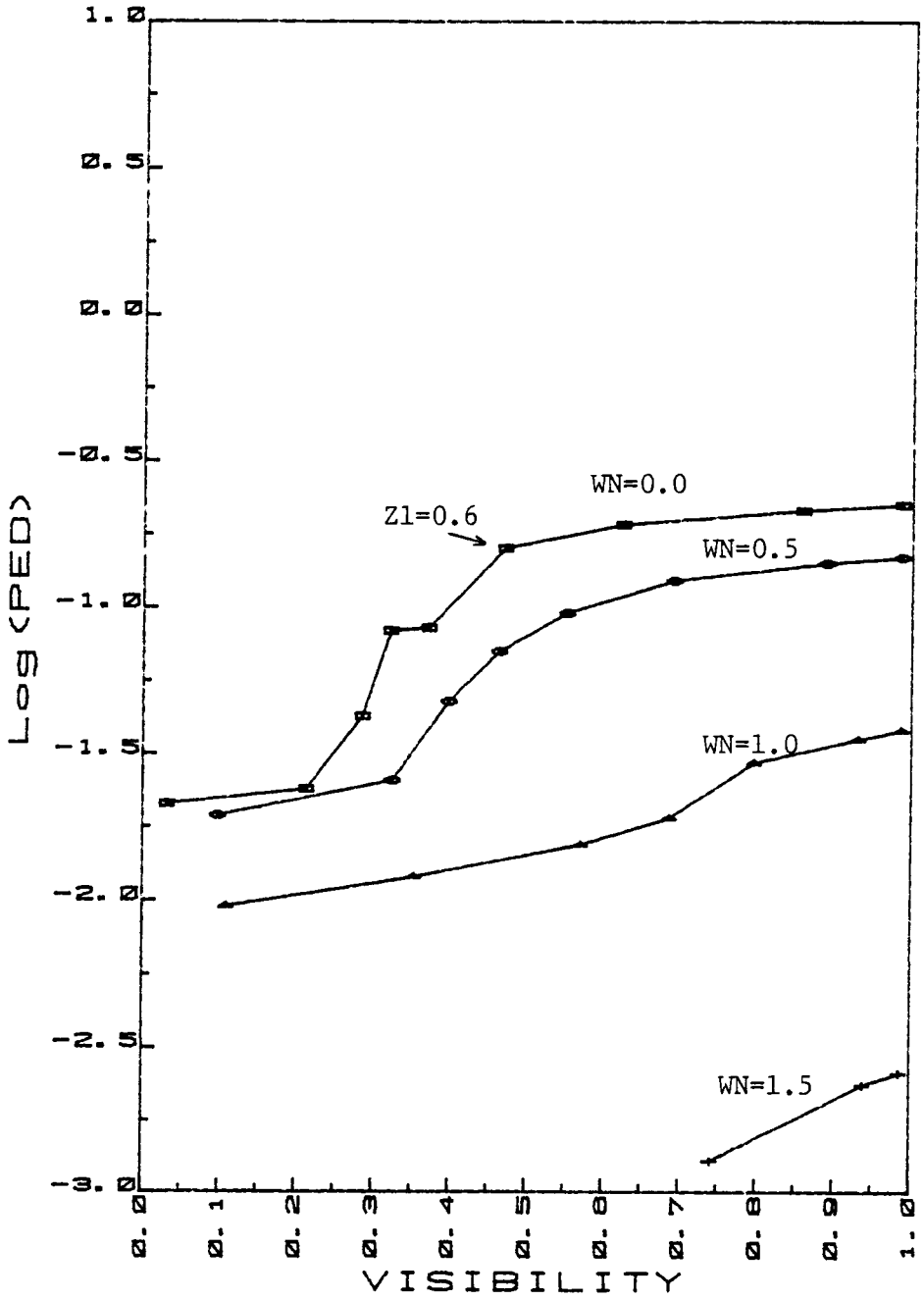

(b) Velocity: 6.5 m/sec.

Figure 17. (Continued).

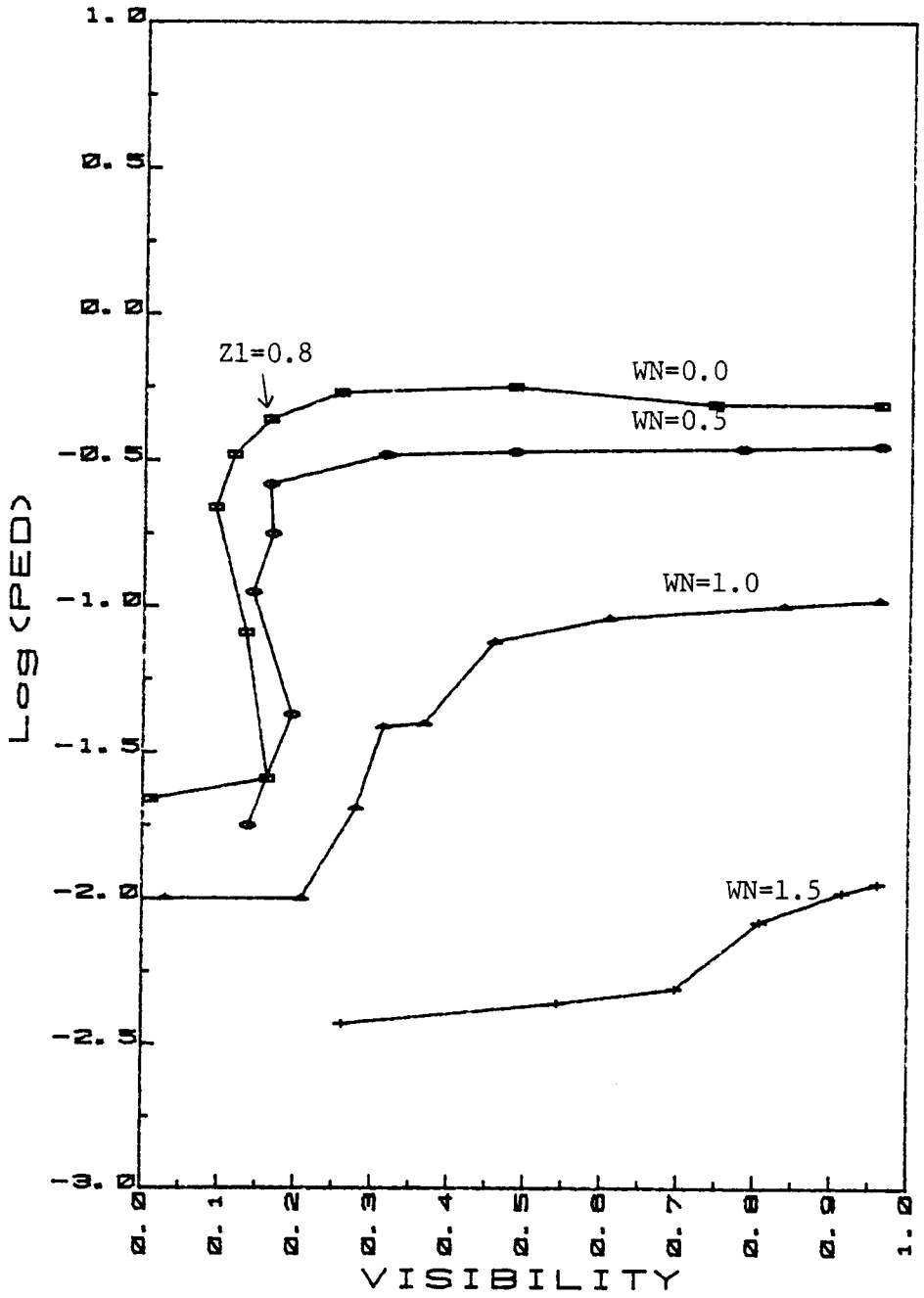

(a) Velocity: 4.5 m/sec.

Figure 18. Mean pedestal amplitude of 1.09 μm PSL particle. Points on each WN curve represent Z1 values 0.0, 0.2, 0.4, etc. from right to left.

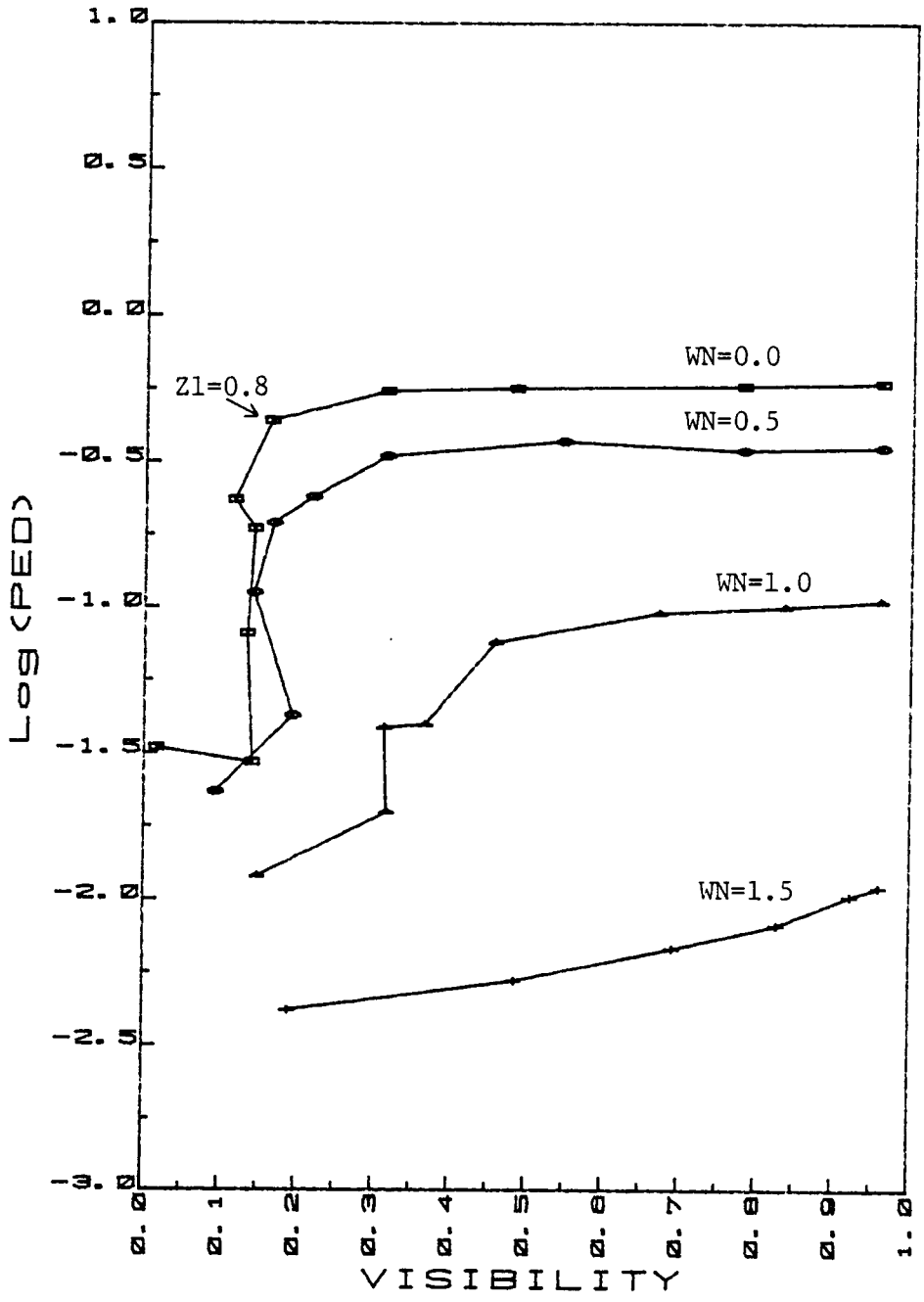

(b) Velocity: 6.5 m/sec.

Figure 18. (Continued).

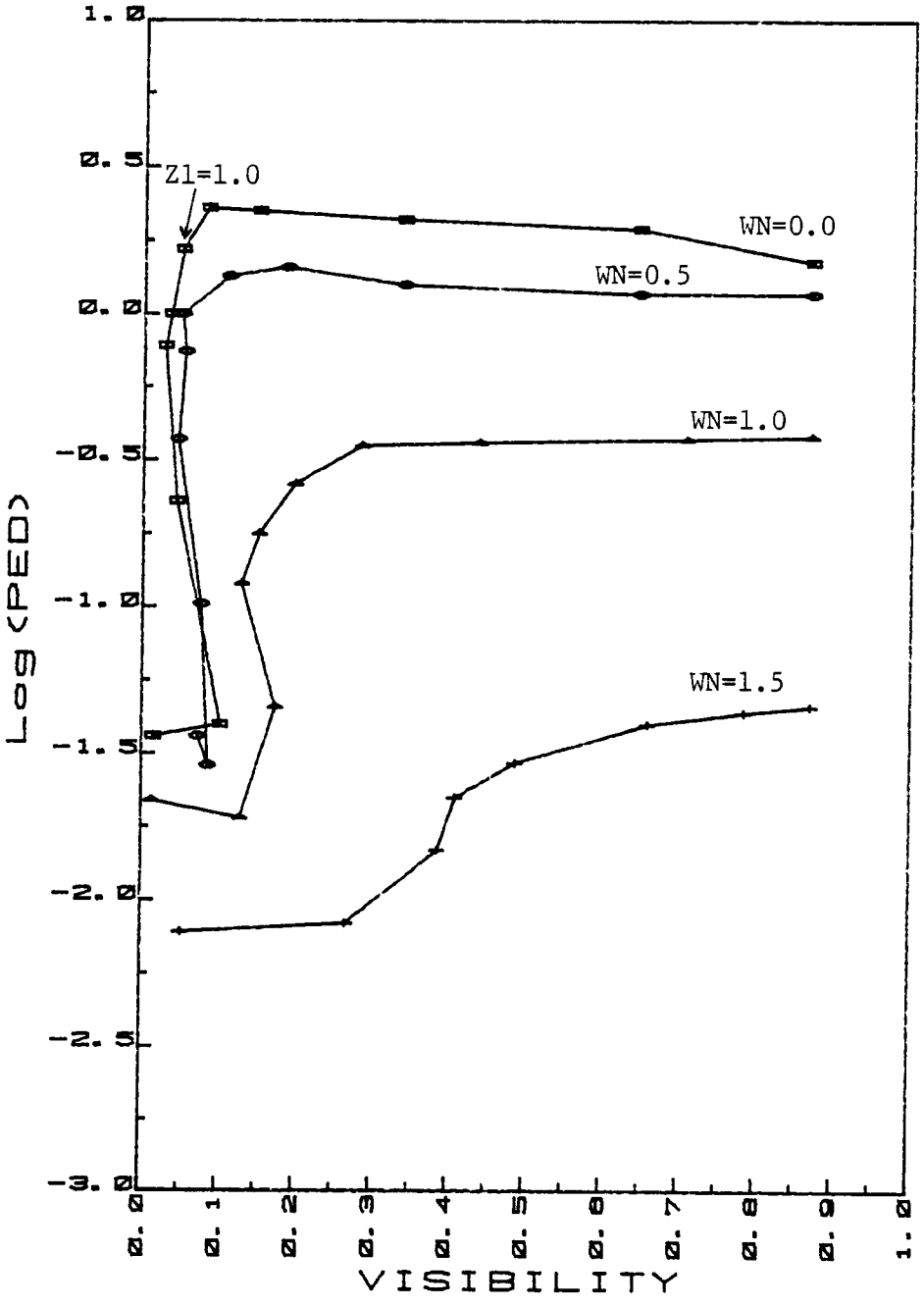

(a) Velocity: 4.5 m/sec.

Figure 19. Mean pedestal amplitude of 2 μm PSL particle. Points on each WN curve represent Z1 values 0.0, 0.2, 0.4, etc. from right to left.

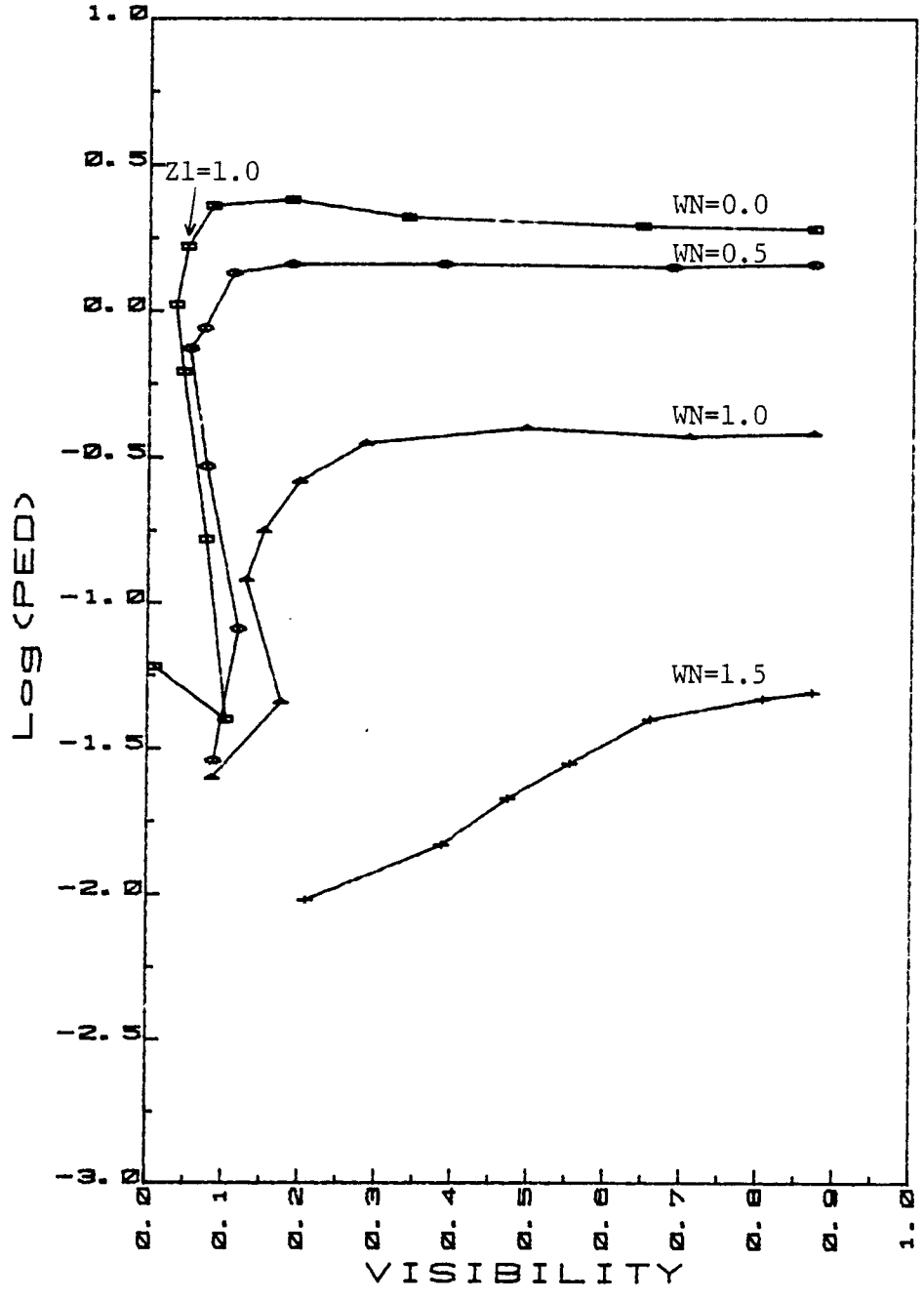

(b) Velocity: 6.5 m/sec.

Figure 19. (Continued).

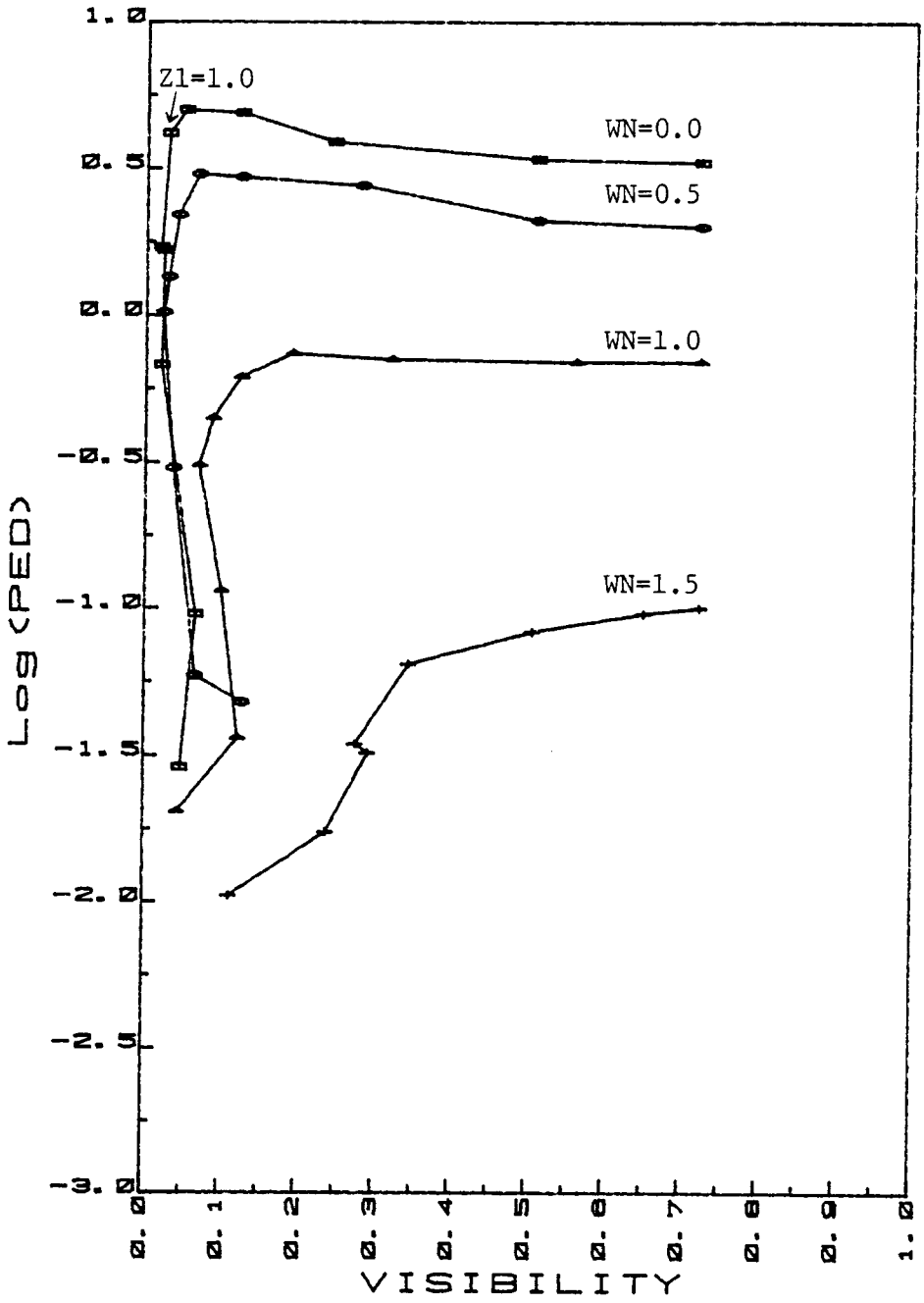

(a) Velocity: 4.5 m/sec.

Figure 20. Mean pedestal amplitude distribution of 3 μm PSL particle. Points on each WN curve represent Z1 values 0.0, 0.2, 0.4, etc., from right to left.

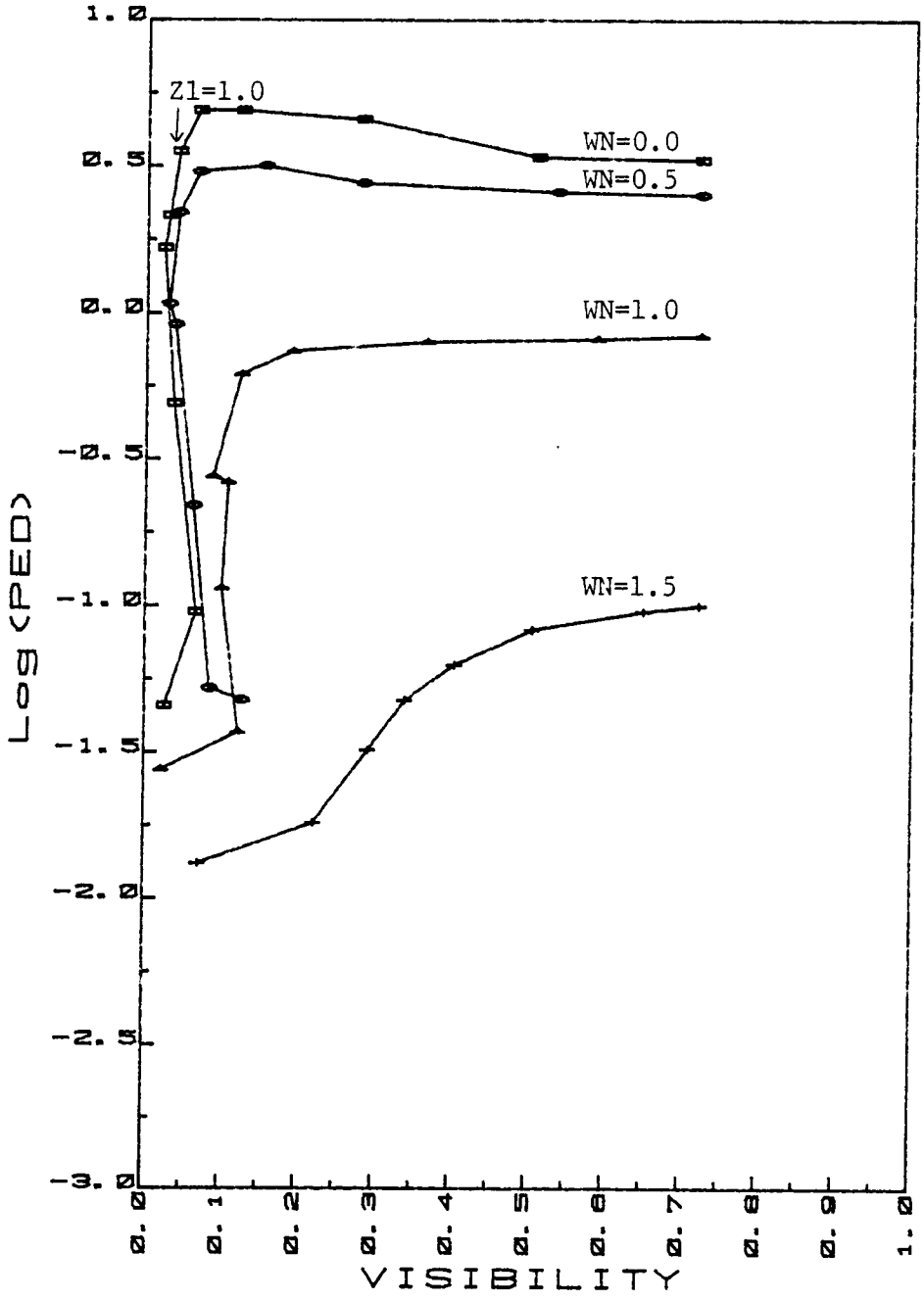

(b) Velocity: 6.5 m/sec.

Figure 20. (Continued).

amplitude ranges of 0.624 μm, 1.09 μm, 2 μm, and 3 μm diameter particles are -0.65 ~ -2.89, 0.23 ~ -2.38, 0.38 ~ -2.02, and 0.69 ~ -1.88, respectively. Similar mean pedestal amplitude levels appear in the same case in 4.5 m/sec.

3. As particle size increases, mean pedestal amplitude increases slightly up to Z1 = 0.8 in the region WN = 0.0 ~ 0.5 at both velocities considered here. This is mainly because, as the Z1 values increase up to 0.8, either laser beam 1 or beam 2 dominates the integration region.

4. Increasing the WN value introduces low rates of fringe visibility variation. This means that the particles with low pedestal amplitude have more probability of appearing in the low visibility region.

5. Mean pedestal amplitude is more dependent on x-axis values than Z1 values.

6. In the case of 3.0 μm diameter particles, the mean pedestal level at WN = 0.5 is higher than that of 2 μm at WN = 0.0.

7. As the particle size (.624 μm ~ 3 μm) increases, the region of minimum expected visibility value also increases.

Since increasing particle diameter introduces decreasing visibility, N_{max} can only increase up to the certain particle size for the size range allowed by the fringe period. In the experimental configuration being considered, maximum N_{max} (51) occurs for a particle diameter between 3.5 μm and 4.5 μm. Therefore, for particle sizes greater than 4.5 μm, the region of minimum expected visibility

value will decrease with increasing particle diameter. From these results, it is concluded that the cross-sectional area of the probe volume will increase with increasing particle size up to diameters producing maximum N_{max} for a given setup.

The maximum acceptable size for a given setup will depend on the signal processor saturation level. However, signal processor saturation levels are not high enough to cover the entire size range measurable by the PSI optics ($0.1\delta \leq D \leq 1\delta$); probe volume cross-sectional area cannot be increased indefinitely by increasing particle diameter.

The maximum possible WN value can be dependent on both PMT slit (or aperture) size and particle diameter. In the case of no limitations due to PMT slit size, the limiting value observable for trajectories passing through the x-axis will be dependent on given experimental arrangement since probe volume intensity is decreasing as a Gaussian function of WN values. However, increasing particle diameter increases the scattered intensity in proportion to D^2.

4. DISCUSSION OF THE RESULTS

For the setup condition given in section 3, an experiment was performed according to the setup given in figure 21. The results of this experiment are compared with the results of computations given in section 3.

4.1 Experimental Setup

To calibrate many kinds of particle-sizing equipment, Polystyrene Latex Spheres (PSL) are often used as reference particles. Commercially available PSL particles are in a stabilizer solution. To use this PSL solution as the reference particle source, it must be diluted in water or alcohol and atomized. A Devilbiss #40 nebulizer was used as an atomizer. For the measurements reported here, the PSL was diluted with ethyl alcohol in a ratio of about 1:300. For removing static charge on the particles generated by the atomization process, a Kr-85 charge neutralizer was used. The atomized particles were further diluted in a dilution chamber to reduce particle number density. Next, the particles were passed through small diameter (about 6 mm inner diameter) glass tubing of 50 cm length. The end of the tubing was aligned with the probe volume and the aerosol-laden air stream directed across it. PSL particle photos taken by an electron microscope show that, for nominal 0.624 μm and 1.09 μm particle diameters, the sizes are about as specified. However, in the 3 μm case, the size is more nearly 2 μm.

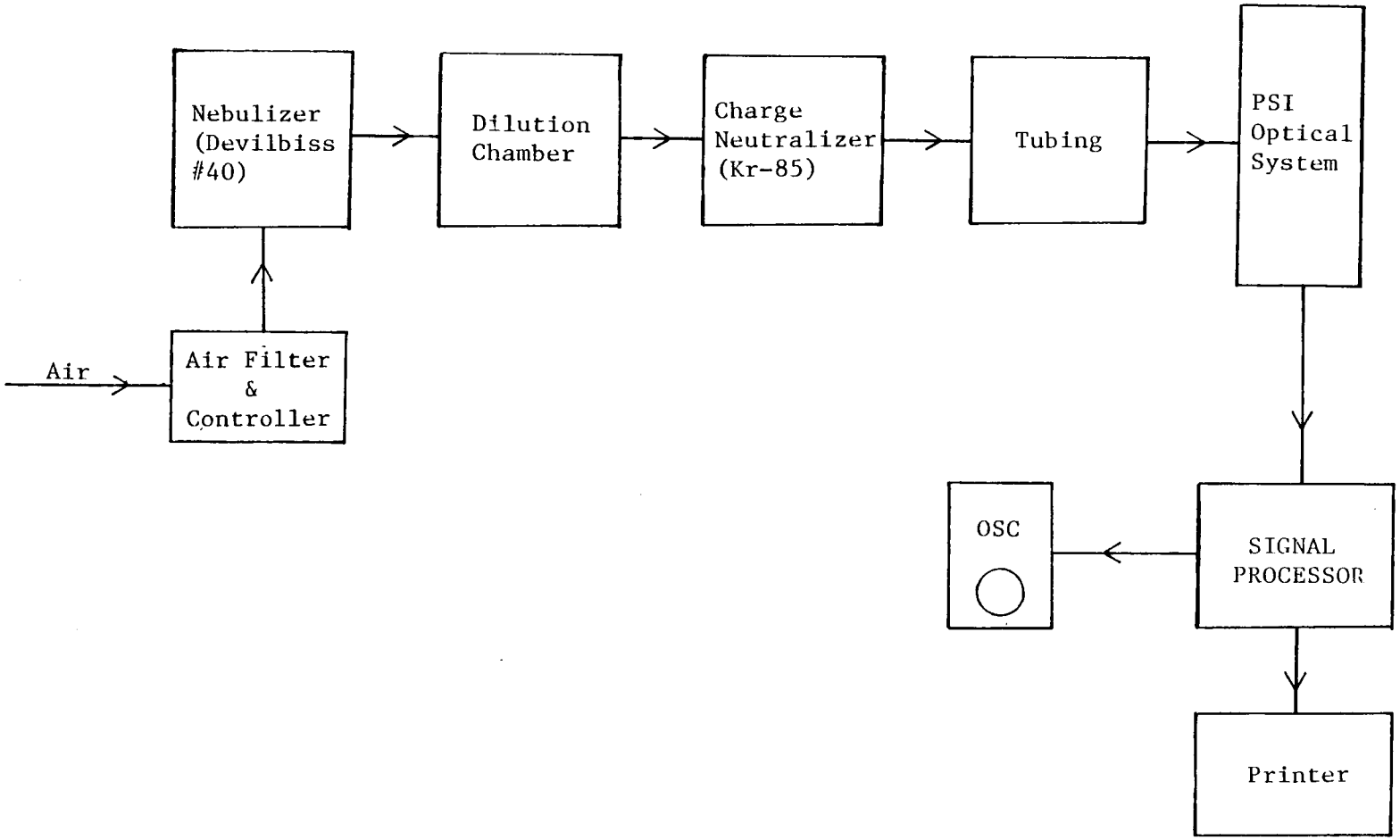

Figure 21. Experimental setup.

4.2 Comparison of Experimental and Computational Results

As explained in section 2, the PSI can measure particle velocity and size. From the velocity measurements, the particle size measurements were classified into different velocity groups. Particles in the velocity range of 4.01 through 4.99 m/sec. were classified into a 4.5 m/sec. group while 6.01 through 6.99 m/sec. particle velocities were grouped as 6.5 m/sec. particles. The mean pedestal amplitudes of these particles are plotted as a function of measured visibility in figures 22a,b through 24a,b for particle diameters of 0.624 μm, 1.09 μm, and 3 μm at velocities of 4.5 m/sec. (a) and 6.5 m/sec. (b).

For the comparison of experimental with computed results, solid curves corresponding to WN = 0.0 and WN = 1.0, respectively, are drawn in these figures. In the case of 3 μm PSL, comparison is made assuming a 2 μm diameter.

From figures 22a,b through 24a,b, it is observed that:

1. In the 0.624 μm particle case, when velocity is 4.5 m/sec., almost all of the particles are confined in $0.0 \leq WN \leq 1.0$ and $0.0 \leq Z1 \leq 0.6$. However, when the velocity is 6.5 m/sec., all pedestal levels are increased by a factor of approximately 1.3 (volts in logarithmic scale) more than that of 4.5 m/sec. cases; and one-third of the particles have higher mean pedestal amplitudes than that of the WN = 0.0 case.

2. For 1.09 μm particle diameters and a velocity of 4.5 m/sec., the majority of the particles are confined in $0.0 \leq WN \leq 1.0$ and

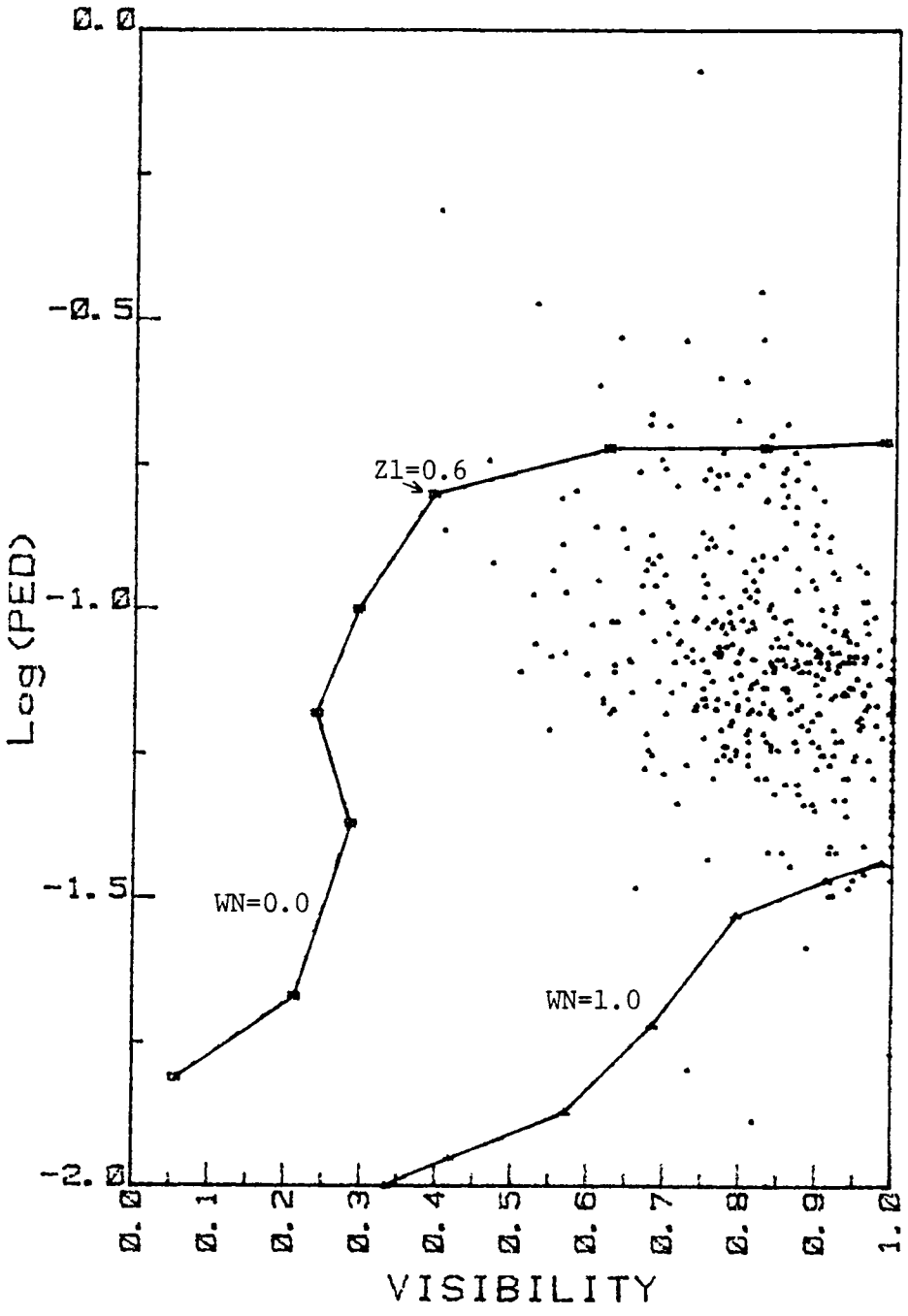

(a) Velocity: 4.5 m/sec.

Figure 22. Pedestal amplitude distribution of .624 μm PSL particle. Solid curve represents computed results. Dots on the solid line represent Z1 values (from right to left Z1 = 0.0, 0.2, 0.4, etc.).

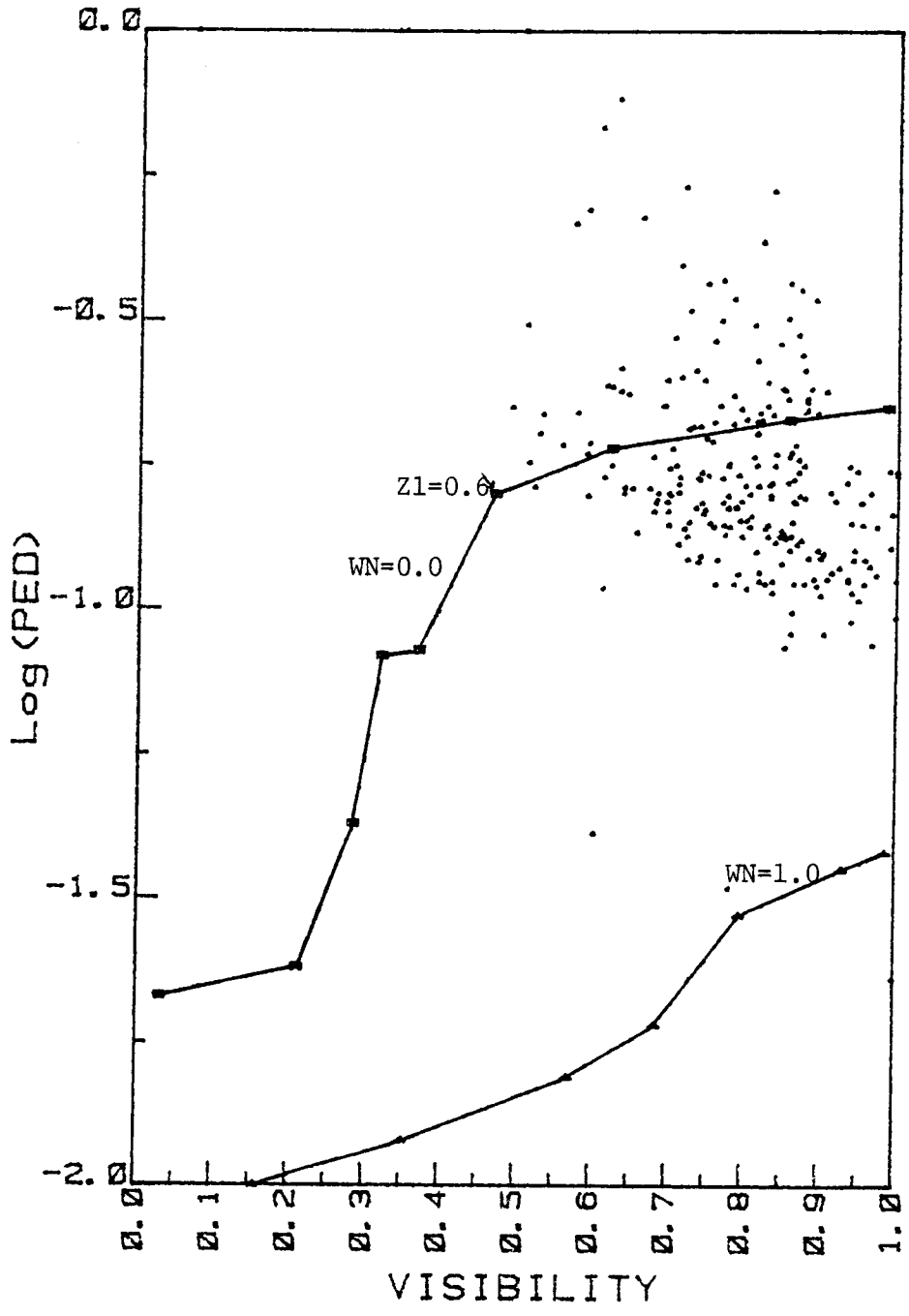

(b) Velocity: 6.5 m/sec.

Figure 22. (Continued).

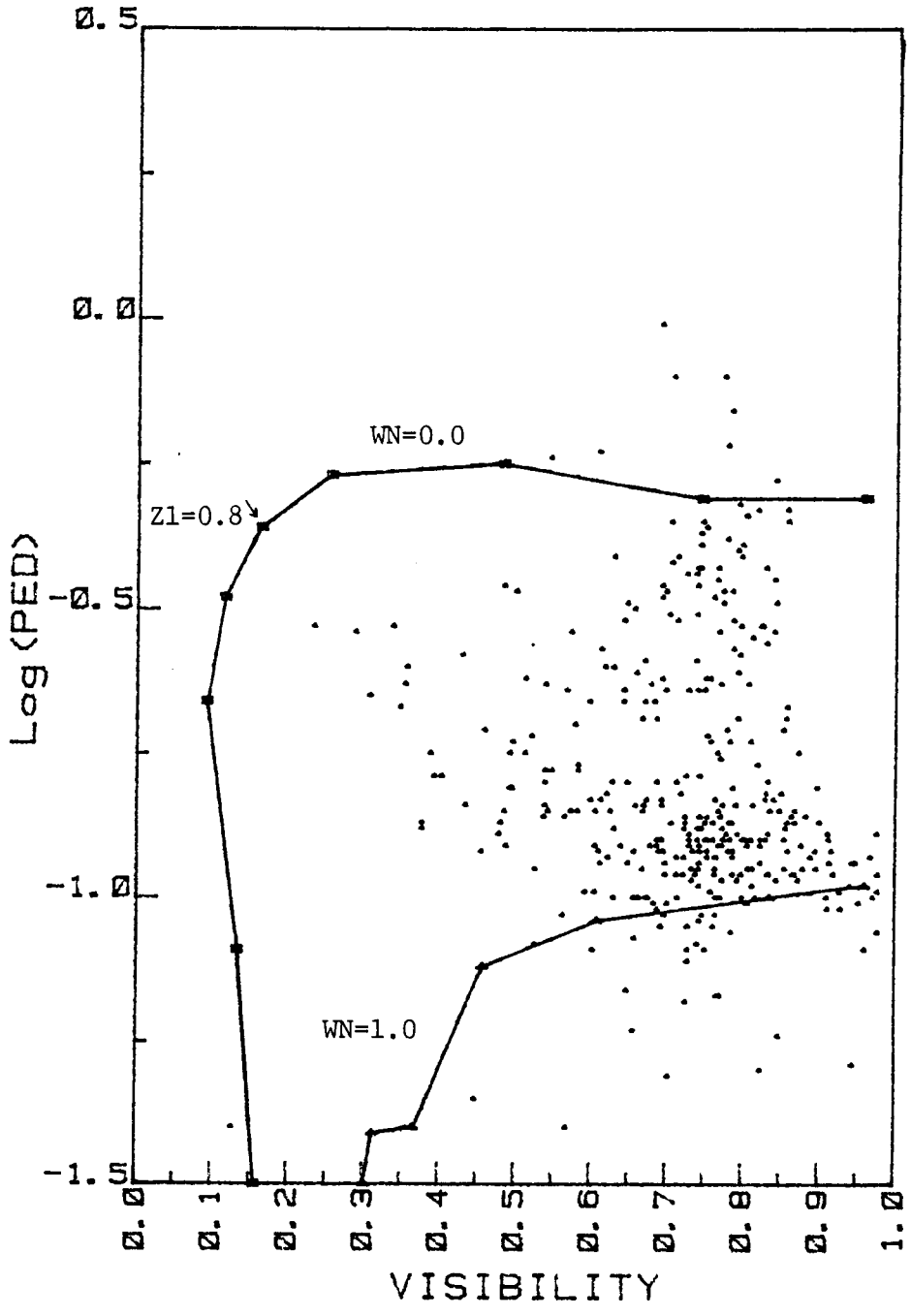

(a) Velocity: 4.5 m/sec.

Figure 23. Pedestal amplitude distribution of 1.09 μm PSL particle. Solid curve represents computed results. Dots on solid line represent Z1 values (from right to left 0.0, 0.2, 0.4, etc.).

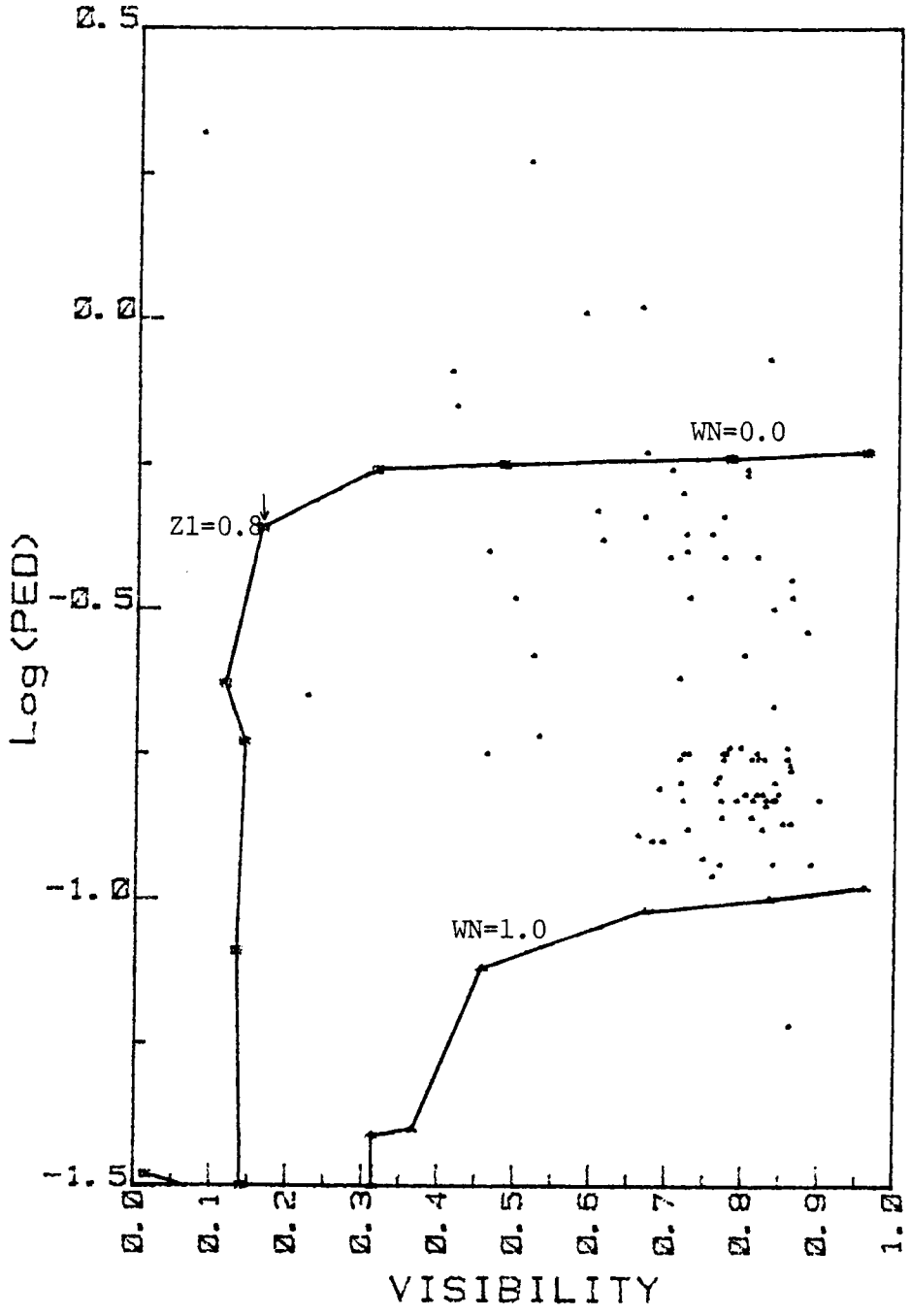

(b) Velocity: 6.5 m/sec.

Figure 23. (Continued).

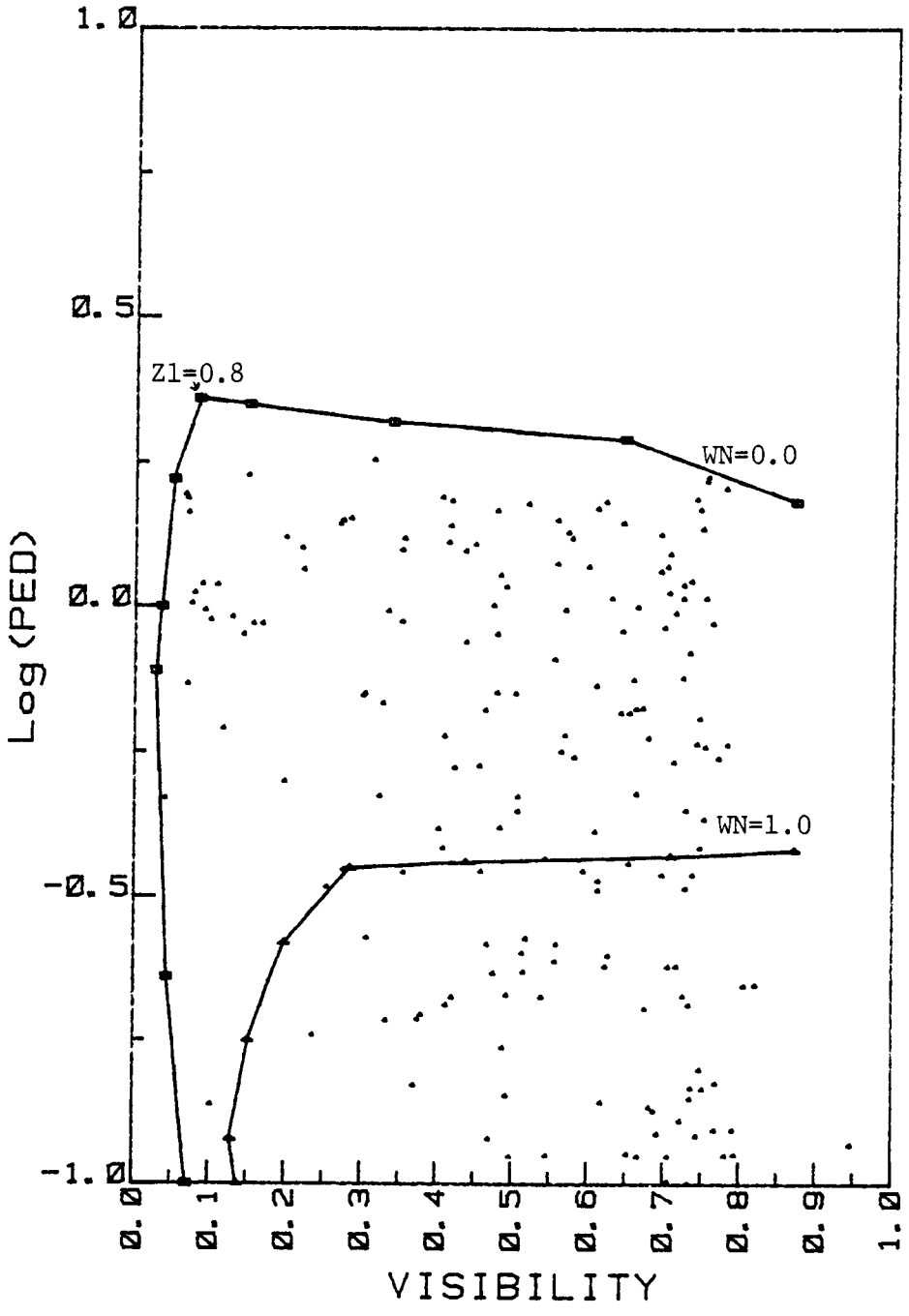

(a) Velocity: 4.5 m/sec.

Figure 24. Pedestal amplitude distribution of 3.0 μm PSL particle. Solid curve represents computed results. The dost on the solid line represent Z1 values (from right to left 0.0, 0.2, 0.4, etc.).

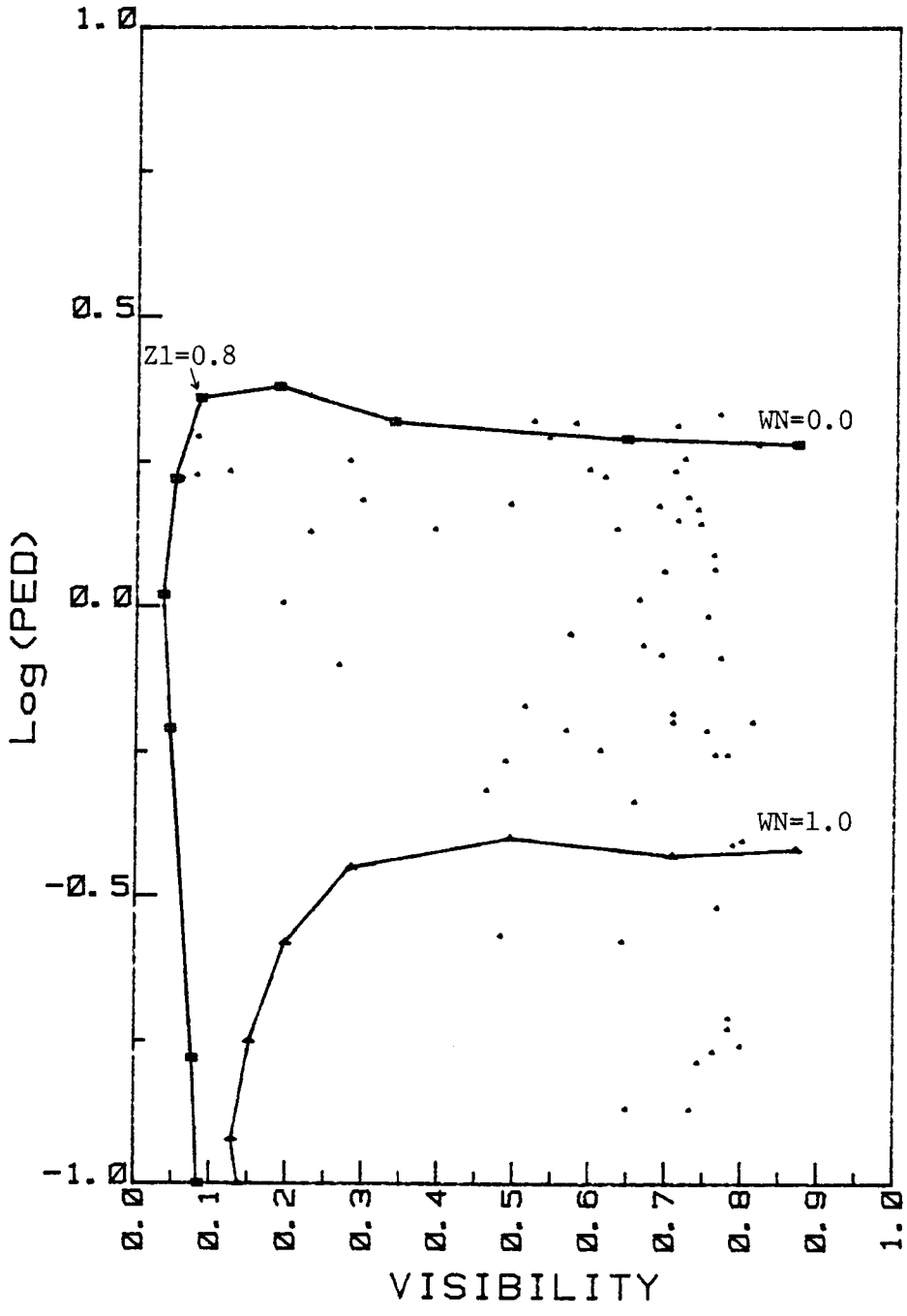

(b) Velocity: 6.5 m/sec.

Figure 24. (Continued).

$0 \leq Z1 \leq 0.8$. A significant fraction falls below WN = 1.0 (Log(PED) = -1.0). When the velocity is 6.5 m/sec., the majority of the particles fall within $0.0 \leq WN \leq 1.0$ and $0.0 \leq Z1 \leq 0.8$.

3. For 3 μm particles at velocities of 4.5 m/sec., all the particles are bracketed below WN = 0.0 and within Z1 = 1.0. Approximately 40% of the particles fall below WN = 1.0. When the velocity is 6.5 m/sec., however, the majority of these particles are bracketed $0.0 \leq WN \leq 1.0$ and $0.0 \leq Z1 \leq 1.0$.

4. For 0.624 μm and 1.09 μm particle diameters at 4.5 m/sec., and for 0.624 μm diameters at 6.5 m/sec., a number of particles have visibility values greater than theoretical maximum values. However, in the other cases apparently no particles have the theoretical maximum values of visibility allowed for these particle diameters.

In actual particle sizing experiments as the number density increases and the particle size (or scattering intensity) decreases, the signal cycles generated by these particles are lower in amplitude and more susceptible to noise generated by the signal processor hardware. Therefore, the relative threshold level of the signal processor increases. As explained in section 3.5, more signal power is removed from the pedestal signal than from the Doppler signal by increased relative threshold levels. Therefore, the visibility of these particles apparently increases.

For cases of theoretical maximum values of visibility less than actual visibility of these particles, the visibility changes caused by the beam stop[4] can be applied to explain these cases. As

particles increase in size, the visibility is decreased from that calculated using Equation 40. When the particle diameter is small compared to δ, this change is negligible. From statements 1, 2, and 3, it is obvious that, when the velocity is 6.5 m/sec., mean pedestal amplitudes of some particles are higher than that of the predicted value. This is because the number density of particles at 6.5 m/sec. is higher than that of the 4.5 m/sec. case.

5. SUMMARY AND CONCLUSIONS

As given in the discussions in section 2.3.4, the signal threshold level related with particle velocity, geometrical optics, and diffraction theory fairly well predicts maximum possible pedestal intensity and possible variation of size distribution, especially in the 1 μm and 2 μm diameter particle case.

It also frequently appears in the experimental data that (1) when particles are small, many particles have larger visibility values than maximum predictable visibility values by Equation 40, and (2) as the particle velocity increases, more particles have larger pedestal amplitudes than the maximum predictable pedestal amplitude.

The discussions and graphs (figures 17a,b through 20a,b and figures 22a,b through 24a,b) presented possible explanations and methods of solution to the following problems often arising in the PSI measurement;

1. PSI amplitude response as a function of particle diameters;
2. Determination of particle size beyond the limits imposed by the visibility measurement;
3. Determination of the cross-sectional area of probe volume as a function of particle size;
4. The velocity dependence of mean pedestal amplitude;
5. The number of signal cycles available for a given experimental arrangement.

From the analysis presented here, three conclusions are reached.

1. For certain experimental conditions such as small beam waist diameter and large fringe period, small particles can generate increased numbers of signal cycles by decreasing the speed of the particles to be measured.

2. For the accurate measurement of particle size with the PSI, the measured size distribution should be weighted properly. The weighting factors will be dependent on the particle velocity, particle size, and setup conditions.

3. By this method, the maximum possible pedestal level of each particle is predictable. In addition, the visibility and pedestal amplitude calculations also give valuable particle size information.

LIST OF REFERENCES

LIST OF REFERENCES

1. W. M. Farmer, "Measurement of Particle Size, Number Density, and Velocity Using a Laser Interferometer" Applied Optics 11, 2603-2612 (1972).

2. W. M. Farmer, "Sample Space for Particle Size and Velocity Measuring Interferometers" Applied Optics 15, 1984 (1976).

3. Private communication with W. M. Farmer of The University of Tennessee Space Institute, Tullahoma, Tennessee.

4. D. W. Roberds, "Particle Sizing Using Laser Interferometry" Applied Optics 16, 1861 (1977).

5. F. Durst, A. Melling, J. H. Whitelaw, Principles and Practice of Laser Doppler Anemometry Academic Press, London (1976).

6. A. E. Siegman, An Introduction to Lasers and Masers McGraw-Hill, New York (1971).

7. H. D. Young, Fundamentals of Optics and Modern Physics McGraw-Hill, New York (1971).

8. W. M. Farmer, "The Interferometric Observation of Dynamic Particle Size, Velocity, and Number Density" Ph.D. Dissertation, Department of Physics, The University of Tennessee, Knoxville, Tennessee (1973).

9. E. Hecht and A. Zajac, Optics Addison Wesley, New York (1974).

10. "BRL PSI Electronics Operations Manual" University of Tennessee Space Institute, Tullahoma, Tennessee.

11. H. C. van de Hulst, Light Scattering by Small Particles John Wiley and Sons, New York (1957).

12. J. R. Hodkinson and I. Greenleaves, "Computation of Light Scattering and Extinction by Spheres According to Diffraction and Geometrical Optics, and Some Comparisons with the Mie Theory" J.O.S.A. 53, 577 (1963).

13. W. D. Bachelo, "A Method for Measuring the Size and Velocity of Spheres by Dual Beam Scatter Interferometry" Applied Optics 19, 363 (1980).

14. A. Ungut, G. Grehan, and G. Gouesbet, "Comparisons Between Geometrical Optics and Lorentz-Mie Theory" Applied Optics 20, 2911 (1981).

15. M. Born and E. Wolf, Principles of Optics Sixth Edition, Pergamon Press, New York (1980).

16. W. M. Farmer, "BRL Particle Sizing Interferometer" The University of Tennessee Space Institute Report GD-TR-80-4, Tullahoma, Tennessee.

17. J. D. Jackson, Classical Electrodynamics Second Edition, John Wiley and Sons, New York (1975).

18. D. M. Robinson and W. P. Chu, "Diffraction Analysis of Doppler Signal Characteristics for a Cross-Beam Laser Doppler Velocimeter" Applied Optics 14, 2177 (1975).

19. A Yariv, Introduction to Optical Electronics Holt, Rinehart, and Winston, New York (1971).

20. H. Schwartz, Information Transmission, Modulation, and Noise Second Edition, McGraw-Hill, New York (1970).

21. L. D. Dickson, "Characteristic of a Propagating Gaussian Beam" Applied Optics 9, 1854 (1970).

22. R. Menzel, "Approximate Closed Form Solution to the Error Function" Am. J. Phys. 43, 366 (1975).

23. M. Ross, Laser Receivers, Devices, Techniques, Systems John Wiley and Sons, New York (1966).

24. S. Hanson, "Broadening of the Measured Frequency Spectrum in a Differential Laser Anemometer Due to Interference Plane Gradients" J. Phys. D: Appl. Phys. 6, 164 (1973).

25. W. H. Pierce, "Numerical Integration Over the Planar Annulus" Journal of the Society for Industrial and Applied Mathematics, Vol. 5, No. 2, (1957) p. 739.

26. A. N. Lowan, N. Davids, and A. Levenson, "Table of the Zeroes of the Legendre Polynomials of Order 1-16 and the Weight Coefficients for Gauss Mechanical Quadrature Formula" Am. Math. Soc. Bulletin 49, 939 (1943).

27. J. D. Pendleton, "Numerical Calculations of Visibility Using Mie Theory of Refraction Theory of Geometrical Optics" Short Course Lecture Notes, The University of Tennessee Space Institute, Tullahoma, Tennessee, June 1980.

APPENDICES

A. NUMERICAL INTEGRATION SCHEME

To evaluate the total scattered power incident on the collecting lens surface, the numerical integration formula over the planar annulus given by Pierce[25] is used. The integral over the annulus with inner radius A_ℓ and outer radius 1 is given as

$$I = \int_{A_\ell}^{1} \int_{o}^{2\pi} \ell F(\ell,\psi) d\psi d\ell \simeq \sum_{i=1}^{4(m+1)} \sum_{j=1}^{m+1} C_j F(\ell_j,\psi_i) \tag{A1}$$

where

$$\psi_i = \frac{\pi i}{2(m+1)} \tag{A2}$$

and

$$C_j = \frac{1}{4(m+1)P_{m+1}(\ell_j^2)} \int_{\ell^2}^{1} \frac{P_{m+1}(\ell^2)}{\ell^2-\ell_j^2} \, d(\ell^2) \tag{A3}$$

and $P_{m+1}(\ell^2)$ is the Legendre polynomial in ℓ^2 of degree m+1 orthogonalized on $^2 \leq \ell^2 \leq 1$, $P_{m+1}(\ell_j^2) = 0$, m = 0, 1, 2, ..., ℓ_j = jth radius of concentric circles, and $\ell d\psi d\ell$ = area element.

Equation A1 provides that the integration of the given function $F(\ell,\psi)$ over the planar annulus is approximately given by the weighted sum of each evaluation point, $F(\ell_j, \psi_i)$, that lies on the intersection of concentric circles (radius ℓ_j) with rays emanating from the origin (the angle between each origin is ψ_i). The degree of accuracy of this formula depends on the m value (the number of evaluation points). Figure A1 depicts a 64-point numerical scheme.

Since the scattering intensity coefficient is given by θ and ψ

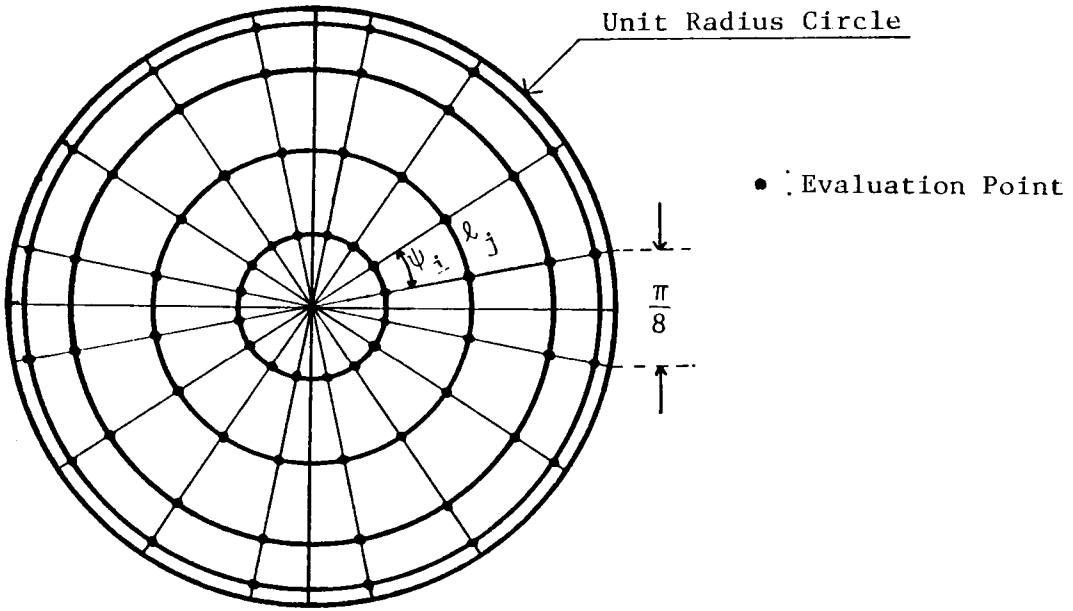

Figure A1. 64 evaluation points in the numerical integration scheme.

and the solid angle is given by da/r^2 (area/squared distance), it is possible to rewrite Equation A1 as

$$I = \int_{A_\ell}^{1} \int_{o}^{2\pi} \ell F(\ell,\psi) d\psi d\ell = \int_{\theta_j}^{\theta_{jmax}} \int_{o}^{2\pi} C(\theta,\psi) d\Omega \cdot \frac{r^2}{r^2} = \int_{\theta_j}^{\theta_{jmax}} \int_{o}^{2\pi}$$

$$\cdot \frac{C(\theta,\psi)}{r^2} da \qquad (A4)$$

so

$$F(\ell_j,\psi_i) = \frac{C(\theta_j,\psi_i)}{r_j^2} . \qquad (A5)$$

If $A_\ell = 0$, evaluation is done over the circular surface ($\theta_j = 0$). Since original integration is carried over the unit radius circle, the radius of the collecting lens should be normalized to unity. This is done in figure A2 by the triangular relation. From the figure A2, the radius of the collecting lens L is changed to 1, and the distance between the probe volume and collecting lens becomes r_o/L. Thus, r_j and θ_j in Equation A5 are

$$r_j = \frac{r_o}{L} + \ell_j^2 \qquad (A6)$$

$$\theta_j = \sin^{-1} \frac{\ell_j}{r_j} . \qquad (A7)$$

The relation between C_j, ℓ_j and the values a_j, x_j given by Lowan, et.al., was given by Pendleton[27]:

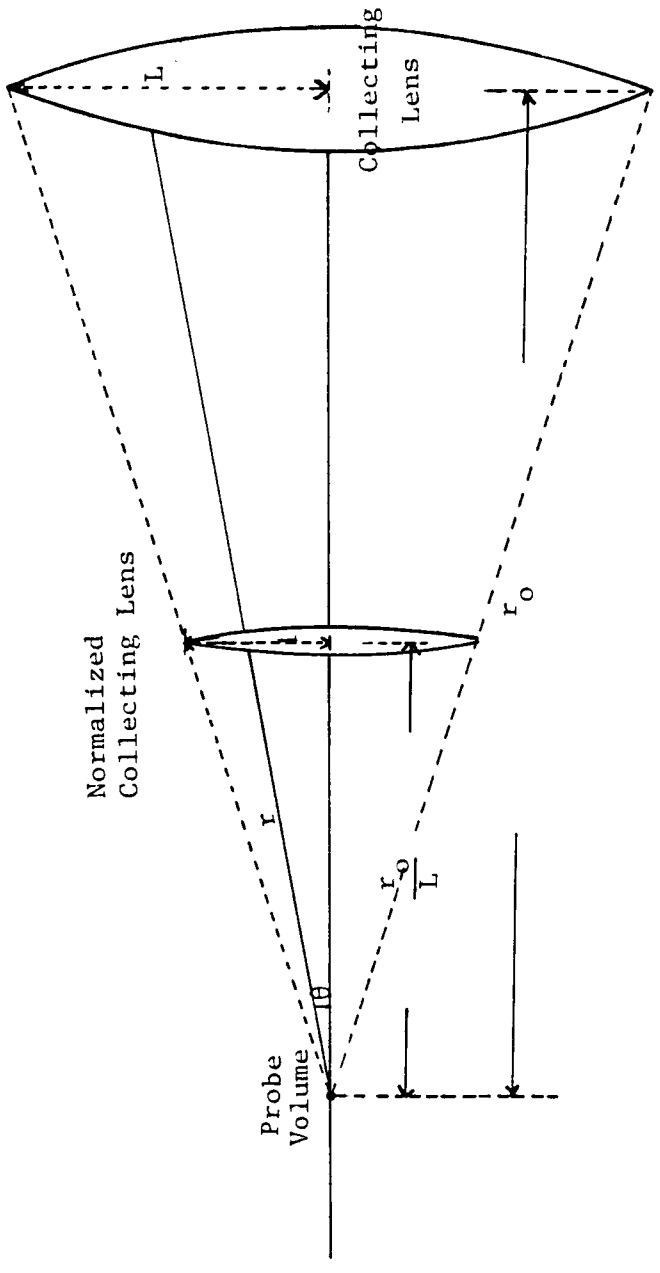

Figure A2. Normalizing of collecting lens' radius to 1.

$$C_j = \frac{\pi}{8(m+1)} a_j \tag{A8}$$

$$\ell_j = \frac{1}{2} (1-A_\ell^2) \cdot x_j + (1+A_\ell^2) . \tag{A9}$$

By the geometry given in figures A3 and A4, θ, ξ, r, P_1, $\phi_{1,2}$ are evaluated by the known parameters ℓ_j, F, ϕ, and β. Thus, by Equations A1 and A4, the scattering gain in Equation 25 can be evaluated.

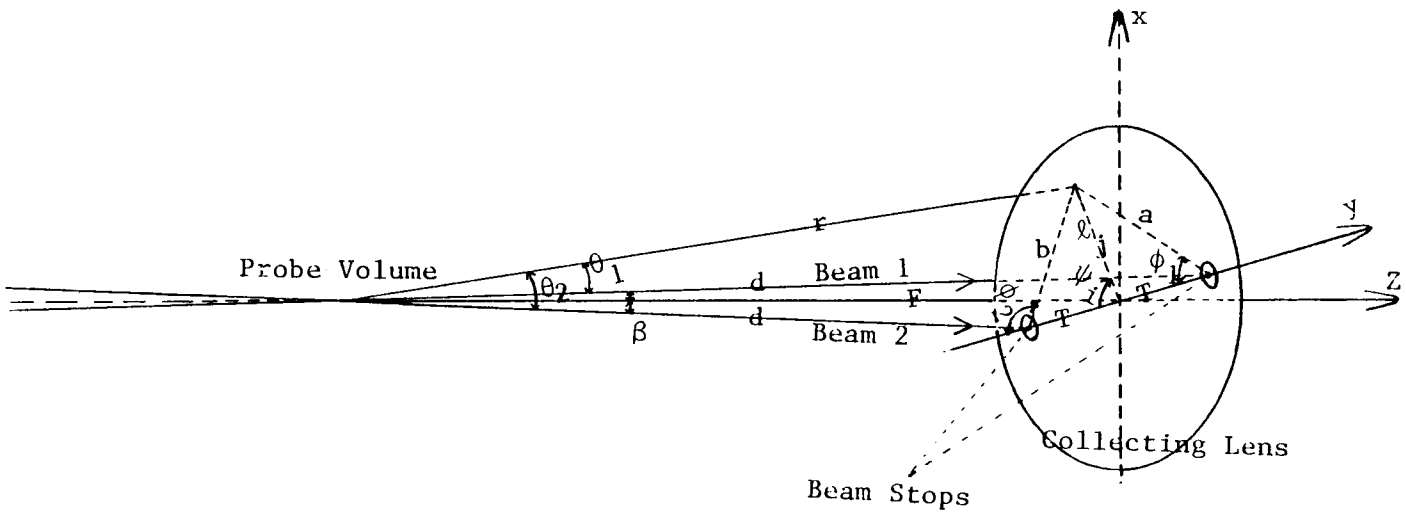

Figure A3. Geometry for numerical integration over collecting lens.

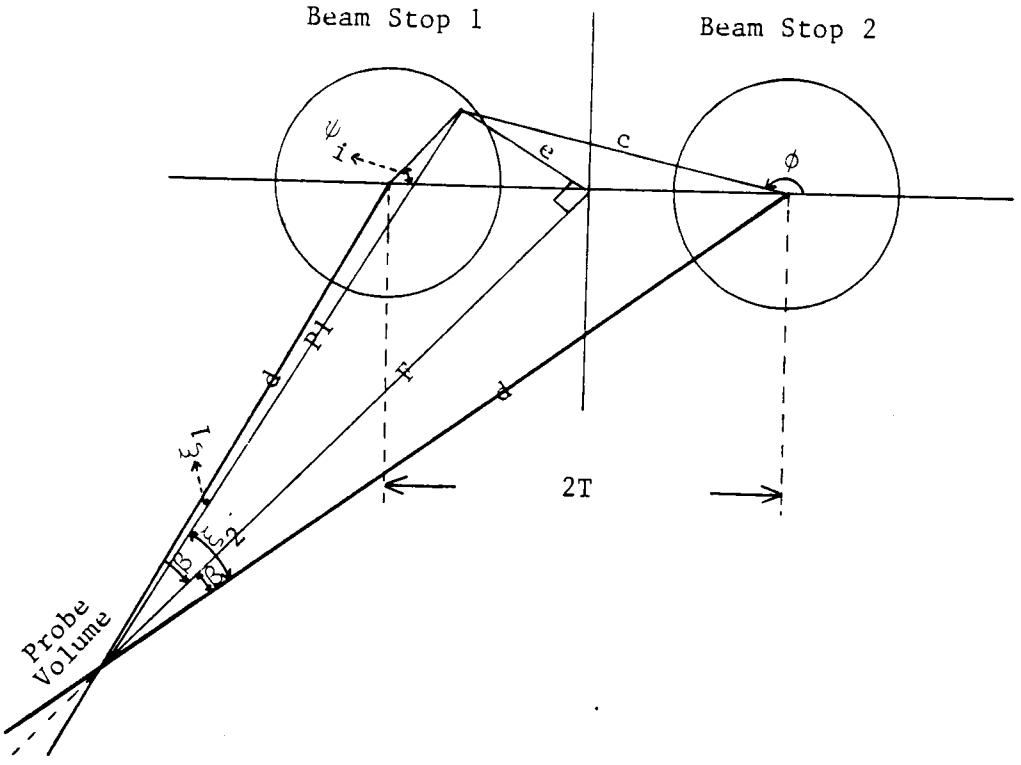

Figure A4. Geometry for numerical integration over the beam stops.

B. RAY TRACE THROUGH THE TRANSPARENT SPHERE

Figure B1 represents the geometry given by Bachelo[13] to evaluate Equation 16(b). The figure shows that, when one of the illuminating rays falls on the point A of a transparent sphere with angle $\frac{\pi}{2} - x$, the refracted angle $\frac{\pi}{2} - x'$ of this ray is specified by Snell's law:

$$m'\sin(\frac{\pi}{2} - x) = m\sin(\frac{\pi}{2} - x') \tag{B1}$$

where m',m are indices of refraction of air and transparent sphere, respectively. If ξ is the angle difference between incident and refracted then

$$\xi = x' - x \ . \tag{B2}$$

If m' is the index of refraction of air, m' = 1. From the Equation B1,

$$x' = \cos^{-1}(\frac{1}{m}\cos x) \ . \tag{B3}$$

To pass through the sphere, this refracted ray is once more refracted at point B. By the geometry given, it can easily be seen that the propagation direction of the ray, θ, is given by

$$\theta = 2\xi = 2x' - 2x \ . \tag{B4}$$

Substituting Equation B3 into B4 yields

$$\theta = 2 \ \cos^{-1}(\frac{1}{m}\cos x) - x \ . \tag{B5}$$

By this equation,

$$x = \tan^{-1}(\frac{m\cos(\theta/2) - 1}{m\sin(\theta/2)}) . \tag{B6}$$

By Snell's law given in Equation B1, x' is obtained.

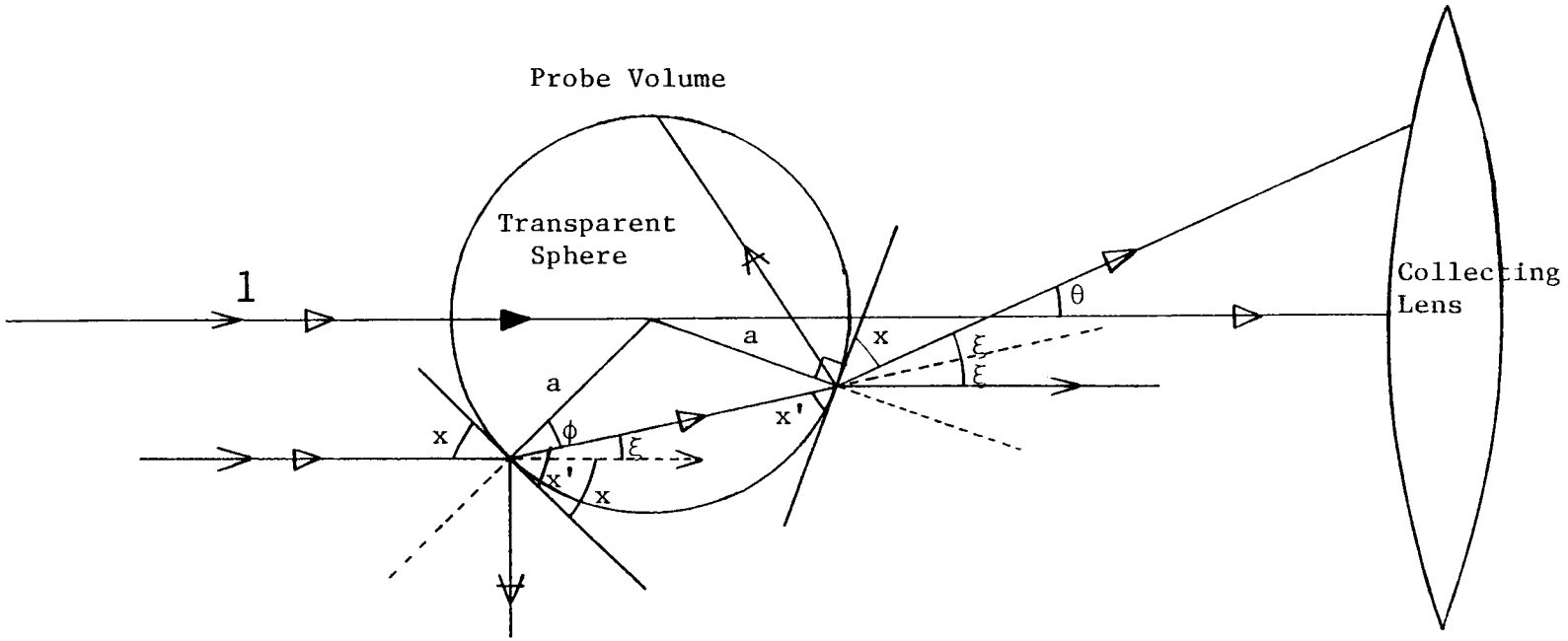

Figure B1. Ray trace through the transparent sphere in the probe volume.

→ : Incident and transmitted rays.

→ : Ray passing through the center of the sphere.

→ : Reflected rays from the sphere.

→ : Represents parallel direction.

VITA

Jung-Young Son was born on February 11, 1950 in Taegu, Korea. He received a Bachelor of Science degree in Avionics with honors from the National Civil Aviation College of Korea in February 1973. Upon graduation from the college, he joined the Republic of Korea Air Force as a communications officer. During that period, he served as an instructor in the areas of long range communication and basic electronics for communication and electronics officers of the ROK Air Force.

After deactivation from the ROK Air Force (July 1977), he joined the Electronics Division of Korea Institute of Science and Technology (KIST) as a research scientist. He entered The University of Tennessee in March 1980 as a graduate research assistant in the Gas Diagnostics Division of the Space Institute.

He received the Master of Science degree with a major in Electrical Engineering in June 1982.

He is a member of Korea Institute of Electronic Engineering and a student member of IEEE.